

Research Report



Comprehensive Revision of Design Considerations for Column Base Connections in Steel Moment Frames

FINAL REPORT

**AISC RESEARCH REPORT NO. 01
NOVEMBER 2022**

Project Title:	Comprehensive Revision of Design Considerations for Column Base Connections in Steel Moment Frames
Primary Investigator(s):	Ahmad S. Hassan and Amit M. Kanvinde
Research Organization(s):	University of California, Davis

DISCLAIMER

The material contained herein has been developed by researchers based on their research findings and is for general information only. The information in it should not be used without first securing competent advice with respect to its suitability for any given application. The publication of the information is not intended as a representation or warranty on the part of the American Institute of Steel Construction (AISC) or of any other person named herein, that the information is suitable for any general or particular use or of freedom from infringement of any patent or patents. Anyone making use of the information assumes all liability arising from such use.

PREFACE

The American Institute of Steel Construction (AISC), headquartered in Chicago, is a non-partisan, not-for-profit technical institute and trade association established in 1921 to serve the structural steel design community and construction industry in the United States. As part of its technical activities, AISC actively funds and supports research related to structural steel design and construction. AISC members primarily come from the structural steel construction community, including producers, fabricators, and engineers.

Many AISC members are engineers, so much of our research supports the engineering community, including maintaining and updating our technical publications such as Design Guides, The Steel Construction Manual, and our Specifications and Provisions. We distribute our specifications free for their use. The primary goal of those specifications is the reliability of structures and, through that, the safety of the public.

AISC does not use the results of research for profit, nor do we sell reports of the research or derivatives from it. Our work is performed in the interest of public safety. As such, we fund projects to, in part, support the development of next-generation steel systems for enhanced performance, safety, sustainability, and economy.

It is reasonably common for AISC research projects to receive additional direct, indirect, or in-kind support from external organizations such as federal or state agencies or member companies. As such, the partial or complete contents of this Report may also reside in the public domain of these external funding agencies.

FINAL REPORT (07-18)

COMPREHENSIVE REVISION OF DESIGN CONSIDERATIONS FOR COLUMN BASE CONNECTIONS IN STEEL MOMENT FRAMES



AHMAD S. HASSAN, & AMIT M. KANVINDE

DEPARTMENT OF CIVIL AND ENVIRONMENTAL ENGINEERING

UNIVERSITY OF CALIFORNIA, DAVIS

15TH NOVEMBER 2022

ACKNOWLEDGEMENTS

The authors are grateful to the Charles Pankow Foundation (Project 07-18) and the American Institute of Steel Construction (AISC) for providing major funding for this research. The authors are also thankful to the Pankow-AISC advisory committee: Mason Walters, Geoff Bomba and Ali Roufegarinejad of Forell/Elsesser Engineers, Jim Malley of Degenkolb Engineers, Chia-Ming Uang of UC San Diego, Subhash Goel of the University of Michigan, Tom Sabol of Engelkirk Structural Engineers, Tim Fraser of Structural Steel Detailing, Tom Kuznick of Herrick Steel, Joe Zona of Simpson Gumpertz and Heger, and Devin Huber of AISC. The findings, opinions, and conclusions/recommendations are those of the authors, and do not necessarily reflect the views of the sponsors.

TABLE OF CONTENTS

Chapter 1 – Introduction	1
1.1 Introduction	1
1.2 Motivation and Background	1
 Chapter 2 – Seismic Performance of Exposed Column Base Plate Connections with Ductile Anchor Rods	 4
2.1 Introduction	4
2.2 Background and Scope	7
2.3 Experimental Program	9
2.4 Experimental Results	16
2.5 Simulations to Assess Deformation Capacity of Untested Configurations	20
2.6 Summary and Conclusions	41
 Chapter 3 – Seismic Response of Blockout Column Base Plate Connections Under Axial Compression and Flexure	 44
3.1 Introduction	44
3.2 Background and Previous Work	48
3.3 Experimental Program	50
3.4 Experimental Results	57
3.5 Models for Strength Characterization	61
3.6 Models for Stiffness Characterization	74
3.7 Summary and Conclusions	76
 Chapter 4 – Seismic Performance of Embedded Column Base Connections with Attached Reinforcement: Tests and Strength Models	 79
4.1 Introduction	79
4.2 Current Practice and Available Strength Models	84
4.3 Experimental Program	89
4.4 Experimental Results	96
4.5 Proposed Model for Strength Characterization	102
4.6 Summary and Conclusions	114
 References	 117

CHAPTER 1

INTRODUCTION

1.1 INTRODUCTION

This report investigates the behavior and design of Column Base Connections in Steel Moment Frames (SMFs) with various configurations, performance objectives, and loading conditions. The investigation comprises three large-scale testing programs, complemented by computational simulations and analytical developments to examine the seismic performance and design of commonly used, as well as newly proposed base connection details. The intent of this report is to address knowledge gaps in the seismic performance of the connection between steel columns and concrete footings, and to develop predictive behavioral models currently unavailable in design practice.

1.2 MOTIVATION AND BACKGROUND

Column bases are arguably the most critical connections in Steel Moment Frames (SMFs), transferring the forces, and moments from the entire structure to the foundation. A variety of details are commonly used for these connections, which can be broadly classified into exposed type with anchor rods, to embedded type with various detailing and attachments – some commonly used types of base connections are shown in Figure 1.1. The role of these connections is even more critical in the seismic response of SMFs as their strength, rotational stiffness, and hysteretic characteristics interact with the frame, influencing force/moment distribution in the frame.

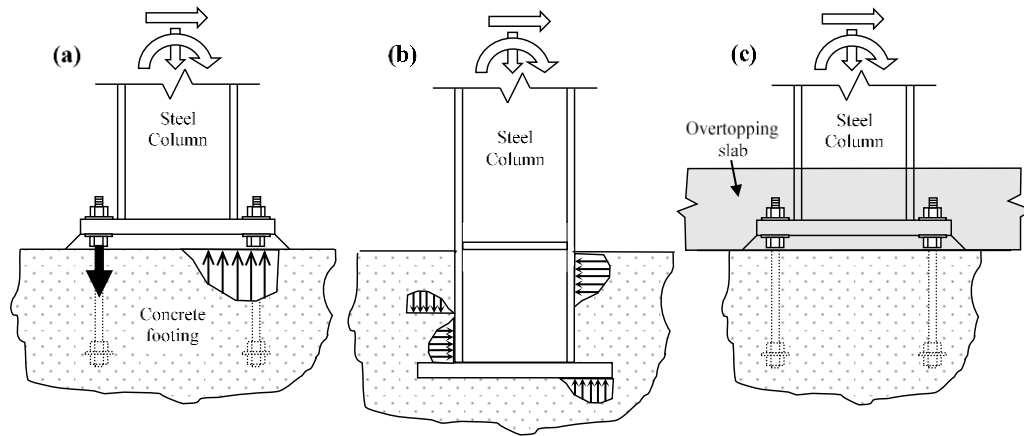


Figure 1.1 – Column base connections and force transfer mechanisms: (a) exposed with base plate and anchor rods, (b) embedded, and (c) slab-overtopped connections

Research on column base connections is relatively limited compared to research on other types of steel connections (for example, beam-column connections). Further complicating factors include the following: (1) these connections take vastly different forms (i.e., exposed, embedded, and shallowly embedded) as shown in Figure 1.1 above and (2) they lie at the interface of steel and concrete, which makes them challenging not only from a mechanics standpoint, but also from the standpoint of design guideline and standards development.

In light of these issues, and considering previous work on the topic of column bases (discussed in detail in the next chapters – as pertains to each study), the following priorities are identified and refined for research:

- 1- Development of ductile and dissipative column base connections that may be used in SMFs as “Weak/Dissipative Bases”, such that they may be designed more economically as compared to “Strong Bases” which are designed to yield the attached column. The aim is to propose methodologies for simulation and design of these connections (as well as the frames) that utilize weak-base connections.

- 2- Experimental investigation of the seismic performance of “Blockout” or shallowly embedded base connections. This includes the consideration of untested parameters, and providing a realistic test setup (representative of the construction practice), and eventually propose a model for strength characterization that provides good accuracy across all available test data.
- 3- Examination of embedded base connections with various types of reinforcement through a program of large-scale testing reflecting commonly used and untested connection details. The goal is to develop fundamental understanding of the force transfer mechanisms, and consequently strength models of commonly used embedded base connections.

Each of the above topics and research priorities is a self-contained study. Consequently, relevant literature review, context, test data, conclusive remarks and other information are provided within each of the chapters. Some or all test data, models, and codes supporting the findings of these studies are available from the authors upon request.

CHAPTER 2

SEISMIC PERFORMANCE OF EXPOSED COLUMN BASE PLATE CONNECTIONS WITH DUCTILE ANCHOR RODS

This chapter presents the post-print version of the article with the following full bibliographic details: Ahmad S. Hassan, Biao Song, Carmine Galasso, and Amit M. Kanvinde (2022). “Seismic Performance of Exposed Column–Base Plate Connections with Ductile Anchor Rods.” Journal of Structural Engineering, American Society of Civil Engineers (ASCE), Vol. 148, Issue 5, 04022028, DOI: [https://doi.org/10.1061/\(ASCE\)ST.1943-541X.0003298](https://doi.org/10.1061/(ASCE)ST.1943-541X.0003298)

2.1 INTRODUCTION

Current seismic design practice for Steel Moment Frames (SMFs) in the United States is intended to develop yielding in plastic hinges at the ends of the beams, while the columns, panel zones, and connections, which are presumed to have limited ductility, remain elastic (AISC 341-16 2016). This is accomplished by designing these non-ductile components for overstrength seismic loads (i.e., by amplifying the reduced base shear by the system-specific overstrength factor Ω_0) or by capacity-protecting the components (i.e., by designing them to withstand the expected strain-hardened strength of connected components). Connections are often designed as per the latter approach. For example, beam-to-column connections are typically designed to resist forces corresponding to the fully yielded and strain hardened moment ($M_{pr} = 1.1 R_y M_p$) in the adjacent beam plastic hinge (AISC-358 2016), in which M_p denotes the plastic moment and R_y denotes the ratio of expected to nominal yield strength. Plastic hinges are also expected to form at the base of the first story columns and are unavoidable from the standpoint of kinematics if a full-building sideway mechanism is desired. These plastic hinges may be accommodated in the column member itself or in the column base connection or the foundation. The former approach (i.e., a “Strong Base” design, forcing the plastic hinge into the column member) is the common practice (AISC

Seismic Design Manual 2018), and is achieved by capacity protecting the connection, i.e., requiring it to withstand $M_{pr} = 1.1 R_y M_p$ of the column in the presence of overstrength axial load. Designing connections in this manner is costly. Specifically, in the case of Exposed Base Plate (EBP) connections (see Figure 2.1a), the application of prevalent design methods (e.g., AISC Design Guide One - Fisher and Kloiber 2006; AISC Seismic Design Manual 2018) usually necessitates the use of multiple anchor rods and a thick plate to resist the large moment corresponding to M_{pr} . For larger column sizes in mid- to high-rise frames, the capacity design approach often favors the use of an embedded-type connection (Grilli and Kanvinde 2017). This is not only costly but also logistically challenging due to multiple concrete pours. The latter approach (i.e., a “Weak Base” design accommodating plastic deformations within the base connection) is allowed by AISC 341-16 (AISC 2016) Section D2.6c, using an overstrength seismic load to design base connections provided that “*a ductile limit state in either the column base or the foundation controls the design.*” However, this is not common because: (1) connection qualification data for column bases or detailing guidance to achieve ductile response is not readily available; and (2) until recently, there was limited understanding of the ductility demands in these connections, if designed as weak bases.

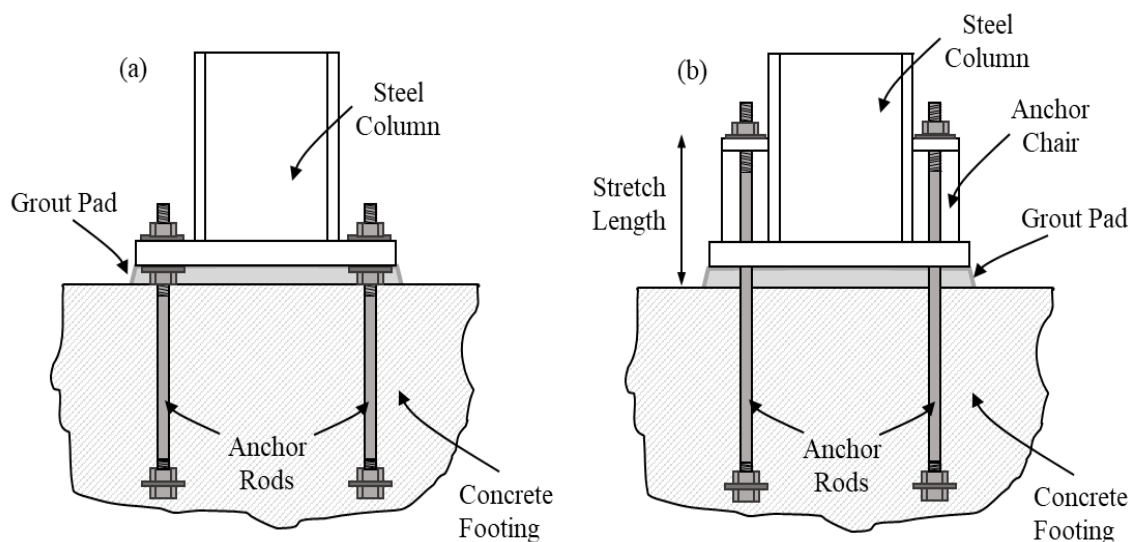


Figure 2.1 – (a) Schematic illustration of an Exposed Column Base Connection; (b) Exposed Base Connection with extended anchors (Soules et al., 2016).

Research conducted over the last 20 years provides motivation for developing high-ductility connections that may be used as weak bases in seismically-designed SMFs. Specifically, experimental studies by Gomez et al. (2010), Kanvinde et al. (2015), Trautner et al. (2017), Astaneh et al. (1992), Fahmy et al. (1999), Burda & Itani, (1999), Lee et al. (2008) and Wald et al. (2020) on EBP connections indicate a very high degree of rotation capacity (in the range of 6-10%). These capacities are observed even without intentional detailing for ductility, and are often as large as (if not greater than) rotation capacities for plastic hinges that form in wide-flanged column members (Elkady and Lignos 2016, 2018; Newell and Uang 2008), suggesting that the strong base approach may not only be expensive, but also counterproductive, forcing yielding into the possibly less ductile element (the column) rather than the base connection. Moreover, Nonlinear Response History Analysis (NLRHA) by Falborski et al. (2020) suggests that base rotation demands in moment frames designed with weak bases (designed for moments corresponding to Ω_o , rather than M_{pr}) are on the order of 4-5% (i.e., 0.04-0.05 rad). When compared to the observed rotation capacities of base connections from the various experimental programs mentioned above, this suggests that the effective development and mainstream adoption of base connections that reliably meet these demands is within reach.

Against this backdrop, this study presents a series of four full-scale experiments and associated computational analyses of EBP connections with yielding anchors. The study demonstrates EBP details that provide high rotation capacity, while also being convenient to fabricate in a practical setting in the United States. Figure 2.2 schematically illustrates the tested details developed in consultation with an oversight committee of fabricators and practitioners – see Acknowledgments. These details feature Upset Thread (UT) anchors, with a smooth shank to accommodate inelastic

cyclic deformations, while the base plate itself remains elastic. The shank is frictionally isolated from the surrounding concrete with polyethylene tape. The specimens are subjected to cyclic lateral loading under constant axial compression. The main variables are the axial load, rod diameter and grade. Complementary simulations of the base connections are conducted to generalize the test findings to untested configurations. The next section presents relevant background, followed by a description of the experimental program and the simulations.

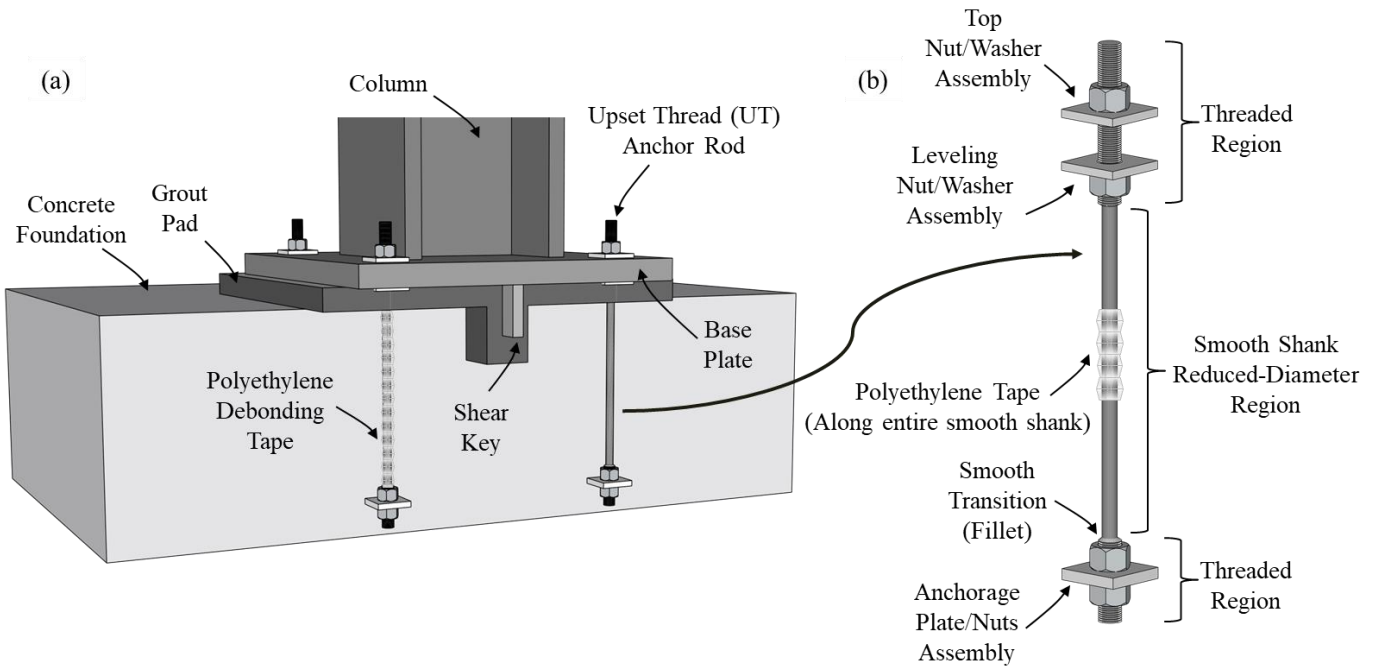


Figure 2.2 – (a) Exposed Base Plate Connection with Upset Thread (UT) anchor rods (Isometric section view); (b) Upset Thread (UT) anchor rod detail.

2.2 BACKGROUND AND SCOPE

Although EBP connections have been a subject of study for over three decades, the primary focus has been on developing strength models (Drake and Elkin 1999) leading to design guidelines (*AISC Design Guide One* - Fisher and Kloiber 2006) and manuals (*AISC Seismic Design Manual* 2018; *SEAOC Structural/Seismic Design Manual* 2015). Observations regarding their high ductility (Gomez et al. 2010; Trautner et al. 2017) have mostly been an outgrowth of studies

primarily focused on their strength characteristics. Conventional design methods for EBP connections consider various limit states, e.g., tensile yielding of the anchor rods or flexural yielding of the base plate on the tension or compression side of the connection, or bearing failure of the footing. Experimental research (including the studies cited above) suggests that concentrating the yielding in the anchors has the potential to maximize overall rotation capacity of the connections. Thus, EBP connections with yielding anchors have been utilized in shake table studies (Lignos et al. 2013; Hucklebridge 1977) with good performance. Nonetheless, the focus in these studies has been on the macro-mechanics of system performance rather than the development of a practically feasible ductile base detail.

Trautner et al. (2016, 2017) conducted comprehensive experimental studies to examine the seismic response of EBP connections with various types of yielding anchors. These experimental specimens reflected construction practice in the United States, with different anchor types (cast-in and post-installed), the use of leveling nuts, and different anchor stretch lengths. All these specimens showed excellent rotation capacity (6–15%) under cyclic loading protocols. Of these, the cast-in anchor detail that was able to distribute yielding over the largest length (longer effective stretch length), showed the greatest rotation capacity, whereas the strong-anchor detail that constrained the anchor yielding resulted in the lowest rotational capacity. In addition, reconnaissance studies conducted after the 2010 Maule earthquake in Chile (Soules et al. 2016) indicate that EBP connections with extended anchors (Soules et al. 2016, see Figure 2.1b) provided excellent seismic performance due to the greater stretch length, which allowed the accumulation of large plastic deformation. Collectively these (and other, e.g., Gomez et al. 2010) studies indicate

that: (1) ductile response of EBP connections may be achieved by concentrating yielding in the anchors; and (2) a large stretch length for distribution of plastic strains is beneficial.

Building on these insights, this study examines the UT detail (shown schematically in Figure 2.2) which has the following features:

1. A fairly long stretch length to distribute plastic strains over the anchor rods, without the use of additional fabrication – e.g., as shown in Figure 2.1b.
2. A smooth shank over this stretch length, to provide a greater resistance to fracture as compared to threaded rods.
3. Frictional isolation of the shank using polyethylene tape to ensure that plastic strains are mobilized over the entire shank.
4. A leveling nut-washer detail on the underside of the base plate (see Figure 2.2) to engage the rod in tensile as well as compressive yielding – in effect, this is similar to Buckling Restrained Braces which show excellent cyclic deformation capacity – e.g., see AISC 341-16.
5. A shear lug/key to transfer column shear.
6. The use of standard materials and fabrication practices, with the exception of the UT rods and the polyethylene tape to minimize additional expense, and facilitate adoption.

2.3 EXPERIMENTAL PROGRAM

This section outlines the experimental setup, test matrix, protocol, and instrumentation. Figure 2.3 illustrates the overall test setup, whereas Table 2.1 summarizes the test matrix. Table 2.1 also includes selected experimental results that are discussed later.

Test Setup and Instrumentation

Figure 2.3 shows the test setup, including the specimen, reaction frame for lateral loads, and the loading cross-beam to introduce compressive gravity loads. Key features of the test setup are:

1. All specimens were cantilever columns with a servo-controlled hydraulic actuator attached at the top. This location (3.4m above the base) was assumed to be the inflection point in a first story column. All columns were A992 Grade 50 ($F_y = 345$ MPa) and were designed to remain elastic to induce failure in the base connection.
2. The cross-beam indicated in Figure 2.3 introduced a constant compressive axial load through an assembly of tension rods and hydraulic jacks in Tests #1, 2, and 3. The lower end of the tension rods was connected to a freely rotating clevis, such that the axial forces were follower forces and did not introduce $(P - \Delta)$ moment into the connection as the column displaced.
3. The footings having a length of 2.74 m (108 in.), a width of 1.83 m (72 in.) and depth of 0.5 m (20 in.) with a nominal compressive strength $f'_c = 27.5$ MPa (see Table 2.2 for measured values) were provided with minimal longitudinal and transverse reinforcement. The reinforcement featured an identical top and bottom mesh of #5 hooked bars (#16 metric size) placed longitudinally at 305 mm (12 in.) on center and transversely at 178 mm (7 in.) on center, with a 76 mm (3 in.) bottom cover.
4. The columns were welded to the base plates with Partial Joint Penetration welds and reinforcing fillet welds. The plate and welds were sized to remain elastic, forcing yielding into the anchors.

Figure 2.2 illustrates the UT detail. Referring to the figure, each anchor rod was milled using a lathe to a reduced diameter denoted d_{UT}^{rod} over a designated stretch length denoted L_{UT}^{rod} . The reduced diameter was chosen such that the fully yielded and strained hardened stretch region would

not induce any yielding in the threaded region. A smooth transition (with a 6.3 mm fillet radius) was provided between the smooth shank and the threaded regions at both ends. At the bottom, a nut and square plate washer assembly provided anchorage. A concrete cover of 13 mm (0.5 in.) was provided below this nut-washer assembly. At the top, nut and plate washer assemblies sandwiched the base plate with oversized holes. The nut immediately below the base plate functions as a leveling nut and also provides a mechanism for introducing compression into the anchor. The upper plate washer was tack welded to the base plate, consistent with construction practice. Oversized holes in the base plate were used to facilitate installation (*AISC Design Guide One*, 2006). The dimensions of the oversized holes and the plate washers, along with the rod dimensions for each of the experiments are summarized in Table 2.1 footnotes. A shear key with a thickness of 25.4 mm was fillet welded to the bottom of the base plate. The key protruded 82.5 mm (3.25 in.) from the bottom surface of the base plate and was accommodated in a pocket in the footing – see Figure 2.2a. A 50 mm (2 in.) layer of non-shrink grout with nominal compressive strength $f_{grout} = 55.1 \text{ MPa}$ was provided between the base plate and the top surface of the concrete footing. This grout was poured after the setting and leveling of the base plate on the leveling nuts (and shim stacks to avoid applying accidental forces to rods during setting). Thus, except for the upset thread rods and the polyethylene tape, the fabrication and erection procedure for the detail is identical to that of conventional EBP details.

The data collected from the experiments includes: (1) lateral force and displacement at the top of the column; (2) axial force in the column; (3) vertical and horizontal displacements of the base plate; (4) strain gage measurements from the anchor rods and the base plate surface; and (5) displacements to monitor rocking and sliding movement of the footing. Additional transducers

were installed to detect unanticipated response modes such as out of plane, and torsional response of the column. Figure 2.4 shows instrumentation schematics for the base plate and the column, identifying the location and purpose of each sensor.



Figure 2.3 – Experimental test setup.

Test Matrix

Referring to Table 2.1, the following test parameters were varied: (1) the axial load, (2) the anchor rod diameter, (3) stretch length, and (4) the anchor grade. The selected parameter values for each considered similarity to prevailing practice, and limitations of the test setup. Specifically:

1. The compressive axial loads were selected to produce significant variation in moment capacity by delaying plate uplift (as estimated by the *AISC Design Guide One* approach), while also not inducing yielding in the base plate on the compression side of the connection.
2. The anchor dimensions were chosen to ensure yielding in the UT region, while other components remained elastic. The embedment length of anchor rods was selected to ensure that the rods achieve their full tensile capacity prior to pullout/breakout concrete failure.
3. Two anchor rod grades, namely Grade 55 and 105, (380 and 724 MPa, respectively) of ASTM F1554, were used.
4. Subsets of tests interrogate effects of individual test variables. For example, Tests #1 and 2 provide an examination of the effect of anchor rod diameter (other variables are held constant), whereas Tests #3 and 4 provide a similar investigation of the effect of axial load.

Tables 2.2 and 2.3 summarize the results of ancillary tests for measurement of material properties. These measured properties are used to interpret results and calibrate analysis models.

Loading Protocol

In all specimens, the axial load was introduced first and held constant while the lateral displacement-controlled loading protocol was applied. Figure 2.5 illustrates the lateral loading protocol, expressed in terms of the column drift ratio. The loading protocol consists of two ATC-SAC (Krawinkler et al. 2000) loading histories applied consecutively (each with a maximum drift of 5%) followed by additional cycles till 6.5% drift amplitude. The ATC-SAC history was selected because it is also mandated for pre-qualification of beam-column connections in SMFs as per AISC-358 (2016); the goals of this study are similar, i.e., to demonstrate performance under high seismic demand. The additional loading cycles (beyond the first application of the ATC-SAC

history) were pre-planned in case failure was not observed during the first application and may represent extreme seismic demands or multiple earthquakes.

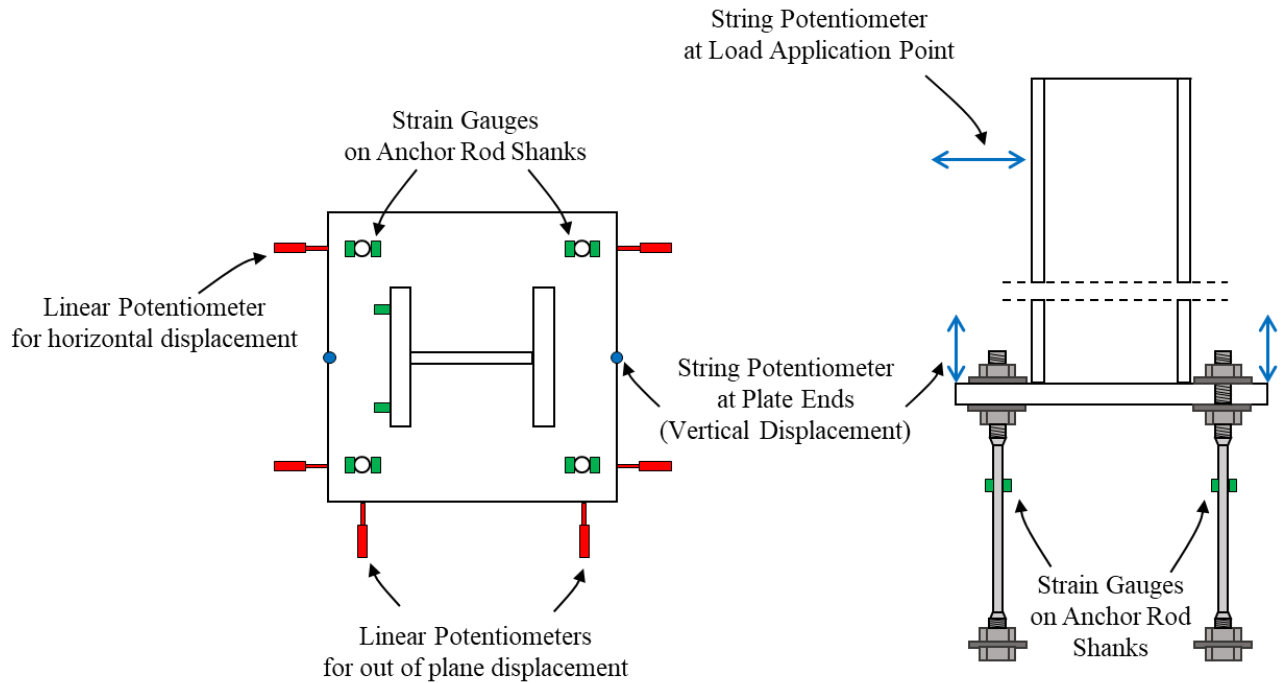


Figure 2.4 – Instrumentation schematics for the base plate and the column.

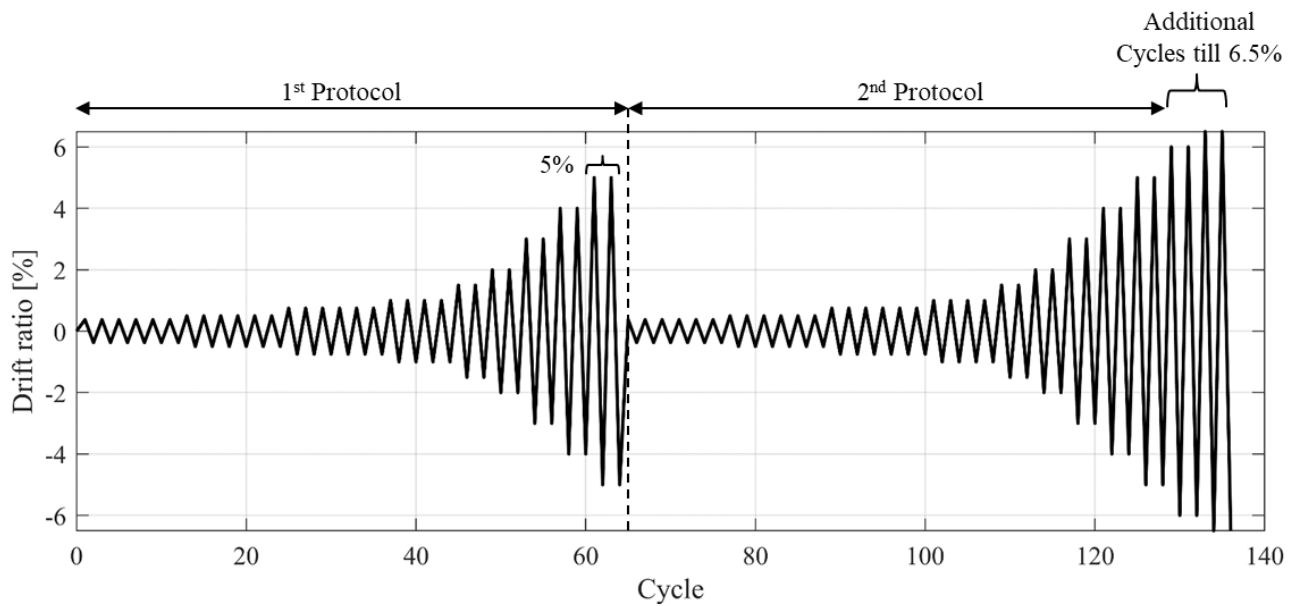


Figure 2.5 – Loading protocol with two consecutively applied ATC-SAC (Krawinkler et al. 2000) loading histories.

Table 2.1 – Tests Matrix and Results

Test ^{a,b}	Axial Load P [kN]	Rod Unthreaded (Core) Diameter $d_{unthreaded}^{rod}$ [mm]	Rod ^c Threaded Diameter $d_{threaded}^{rod}$ [mm]	Rod Reduced Diameter d_{UT}^{rod} [mm]	Rod UT Length L_{UT}^{rod} [mm]	ASTM ^d F1554 Anchor Grade	M_{DG1} ^e [kN.m]	$M_{max}^{test\ f}$ [kN.m]	$\frac{M_{max}^{test}}{M_{DG1}}$	$\frac{M_{4\%}^{test\ g}}{M_{max}^{test}}$
1	534 (120 kip)	19 (0.75")	16 (0.63")	12.7 (0.5")	419 (16.5")	55 (380 MPa)	356.7	506.8 (+)	1.42	0.82
2		25.4 (1")	22.3 (0.88")	19 (0.75")	381 (15")		346.5	420 (-)	1.18	0.77
3						428 (+)		1.24	0.97	
						467 (-)	1.35	0.94		
4	451.7					552 (+)	1.22	0.90		
						611 (-)	1.35	0.93		
0	263.7					402.5 (+)	1.53	0.98		
		378 (-)	1.44	0.93						
		Mean	1.34	0.90						
		COV	0.09	0.07						

^a Tests featured $W14 \times 370$ (customary units) cantilever columns - ASTM A992 Grade 345 MPa.

^b Base plate dimensions: $N \times B \times t_p = 762 \times 762 \times 51$ mm; Edge distance between rod centerline and edge of plate = 101.5 mm. with 2 rods on each side; Oversized hole diameter in plate = 47.5 mm.

^c Square plate washers at top and bottom dimensions: $76 \times 76 \times 9.5$ mm and $76 \times 76 \times 12$ mm, respectively.

^d Values of anchor rod yield strength f_y^{rod} are nominal.

^e Moment calculated in accordance with current procedures outlines in AISC's Design Guide One - Fisher and Kloiber (2006).

^f Maximum moment measured for specimens in each direction of loading (positive and negative).

^g The ratio between the base moment at 4% drift (during the first application of SAC protocol) and the maximum moment.

Table 2.2 – Summary of measured material strengths from concrete/grout ancillary tests

Cure Age	# of Samples	Concrete Compressive Strength f'_c [MPa]	Grout Compressive Strength f_{grout} [MPa]
28 days	8	28.3	-
Day of full-scale test		31.0	58.6

Table 2.3 – Summary of measured material strengths from anchor rod ancillary tests (as per ASTM A370, 2020)

ASTM ^a F1554 Rod Grade	# of Samples	f_y^{rod} [MPa]	f_u^{rod} [MPa]	$\frac{\epsilon_{max}^{Test}}{\epsilon_{max}^{ASTM}}$ ^b
55 (380 MPa)	3	405.4	552.3	1.53
105 (724 MPa)		775.0	946.7	1.32

^a Measured yield stress for Grade 105 rods, is based on the 0.2% offset method.

^b The ratio between the average maximum strain for tested rods at fracture and the maximum strain provided by ASTM 1554 (2020) for a 8 in. (203 mm) gage length.

2.4 EXPERIMENTAL RESULTS

Figures 2.6a-d show the moment rotation plots for all four specimens. The rotation in these is determined by subtracting the elastic column rotations from the overall drift. For all specimens, the initial elastic response was observed until a base rotation of approximately 0.008-0.01 rad was reached; this corresponds to column drift of approximately 1-1.1 %. This was followed by non-linear response due to the yielding of the anchors with a gradual increase in resistance until a rotation of 0.04-0.05 rad. This was accompanied by gradual cycle-to-cycle degradation, as damage accumulated in the grout. After this point, the flexural resistance slowly decreased due to cycle-to-cycle degradation, although in-cycle degradation (i.e., negative slope) or failure was not observed in any of the experiments. For all specimens, the hysteretic response was pinched, owing to gapping and contact between the base plate and the footing. The hysteresis loops also showed an intermediate plateau of resistance (for tests with axial load). As noted previously by Gomez et al. (2010), this corresponds to the flexural resistance due to the prestressing effect from axial compression, wherein the connection resists moment without developing tension in the anchors. All tests exhibited extremely high deformation capacity, surviving both applications of the ATC-

SAC protocol as well as the subsequent 6.5% cycles, without rod fracture or any other form of catastrophic failure.

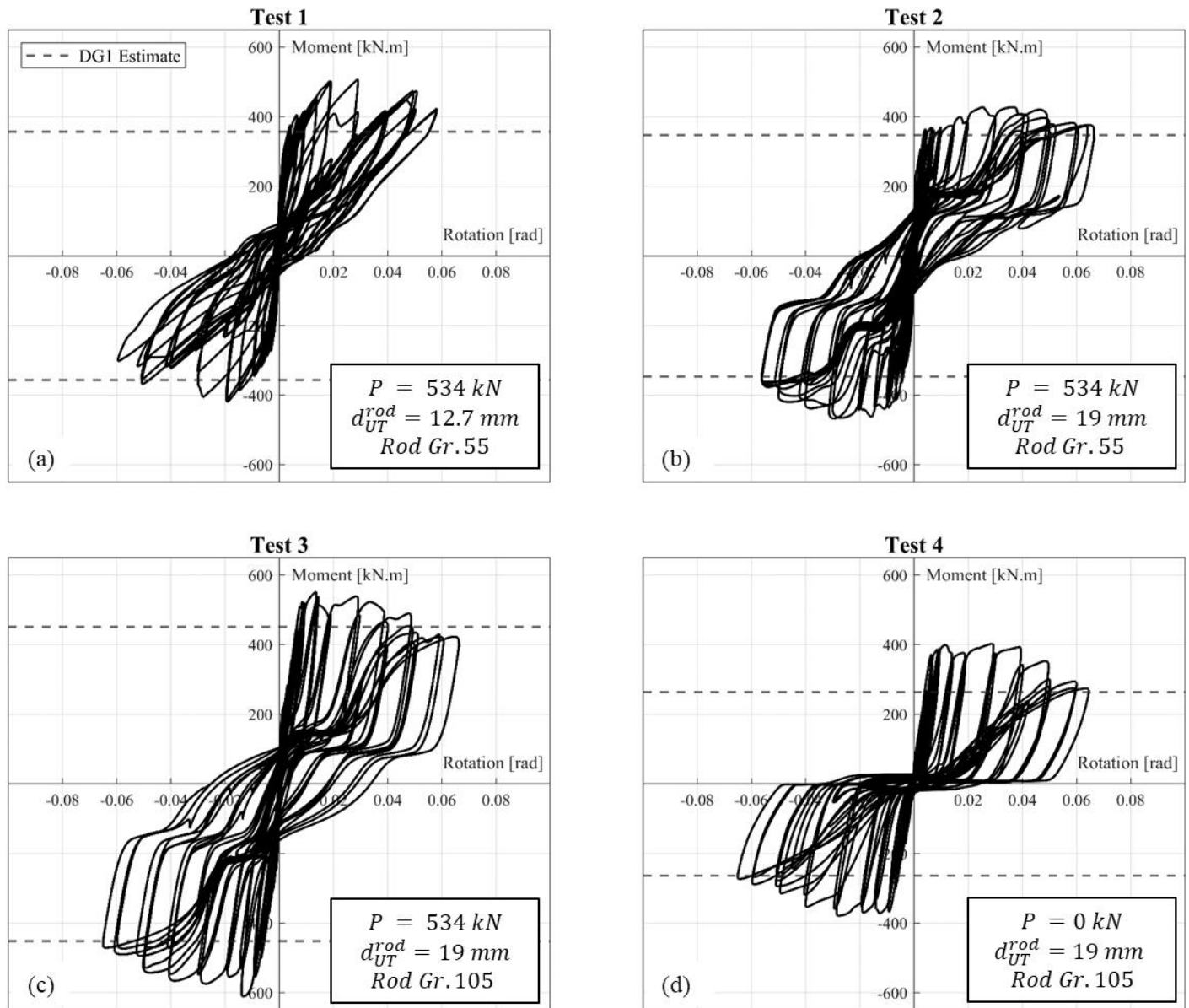


Figure 2.6 – Moment-Rotation plots for all tested specimens.

Figures 2.7a-d show damage progression photographs for one of the tests (Test #3) taken at various points during the cyclic loading history. The photographs illustrate typical response and failure modes of all test specimens. Referring to the photographs, the damage accumulation was gradual,

and observable mainly in the spalling of grout. Figure 2.7a illustrates damage observed during the initial stages of loading (at drifts $\leq 1\%$). Minor cracks began to form in the grout pad accompanied by surface flaking at the top of the pad surrounding the plate, with traces of plate separation from the pad at the plate/grout interface. However, this did not affect the load-deformation response, such that linear elastic response was observed until drifts of 0.8%. As loading progressed, the following damage modes were observed:

- Vertical cracks (Figure 2.7b) in the grout pad near the plate edges and cracks radiating from plate corners, followed by the breakage of the cold joint between grout and concrete.
- This damage progression continued until the end of the first SAC protocol (drift of 0.05 rad), leading to crushing/spalling of grout chunks at the plate corners with separation from the pad under the baseplate footprint. During the second application of the protocol, these chunks continued to crush and separate further from the base plate – see Figure 2.7c.
- No damage to the concrete footing was observed due to bearing. However in all specimens, punch-out of the anchor rods occurred through the bottom cover of the concrete, resulting in a gap below the bottom nut-washer assembly (Figure 2.7d). This gap was 13mm long (the thickness of the concrete cover), and allowed unrestrained vertical movement of the anchor through the gap. Implications of this are discussed in a subsequent section.
- Anchor rod yielding was observed in all tests. The yielding initiated in the stretch region between a drift of 1 and 1.5% for all tests (strain data from anchor rods confirmed this). As the grout pad deteriorated, compression force was transferred to anchor in compression through the leveling nut. At larger deformations ($> 4\%$ drift), dishing of the plate washer immediately below the base plate was observed, resulting in a small gap (~ 3 mm) at the top nut level (Figure 2.7c). This gap did not have any significant effect on the connection response.

Table 2.1 summarizes measured quantitative data. Two moment strength values are recovered for each specimen, one corresponding to the maximum moment measured in each direction of loading. These are denoted as M_{max+}^{test} and M_{max-}^{test} , where the positive sign denotes the direction of application of the first deformation cycle. The table includes the ratio between the maximum column base moment (M_{max+}^{test} and M_{max-}^{test}) observed during testing and the moment M_{DG1} calculated in accordance with current procedures outlined in *AISC's Design Guide One*, and measured material properties summarized in Tables 2.2 and 2.3. Referring to Table 2.1, the average value of M_{max}^{test}/M_{DG1} for all tests is 1.34 (with a Coefficient of Variation 0.09), indicating that the *AISC Design Guide One* approach is conservative. Table 2.1 also includes the ratio between the base moment observed at 4% drift (during the first application of the SAC protocol) and the maximum moment, i.e., $M_{4\%}^{test}/M_{max}^{test}$. This provides a direct point of reference to pre-qualification standards for beam-column connections (AISC 341-16 2016), wherein a resistance of 80% of the beam strength is required at 4% drift, when subjected to the ATC-SAC protocol. Referring to Table 2.1, the average value of $M_{4\%}^{test}/M_{max}^{test}$ across all experiments is 0.9, with a CoV of 0.07, indicating good performance in terms of maintaining strength for large deformations. The flexural resistance increases with the increase in compressive load (e.g., see Test #3 and 4 that are otherwise identical), as well as with an increase in anchor diameter (e.g., see Test #1 and 2) or steel grade (e.g., see Test #2 and 3). Other than these, the response was fairly consistent across the test variables.

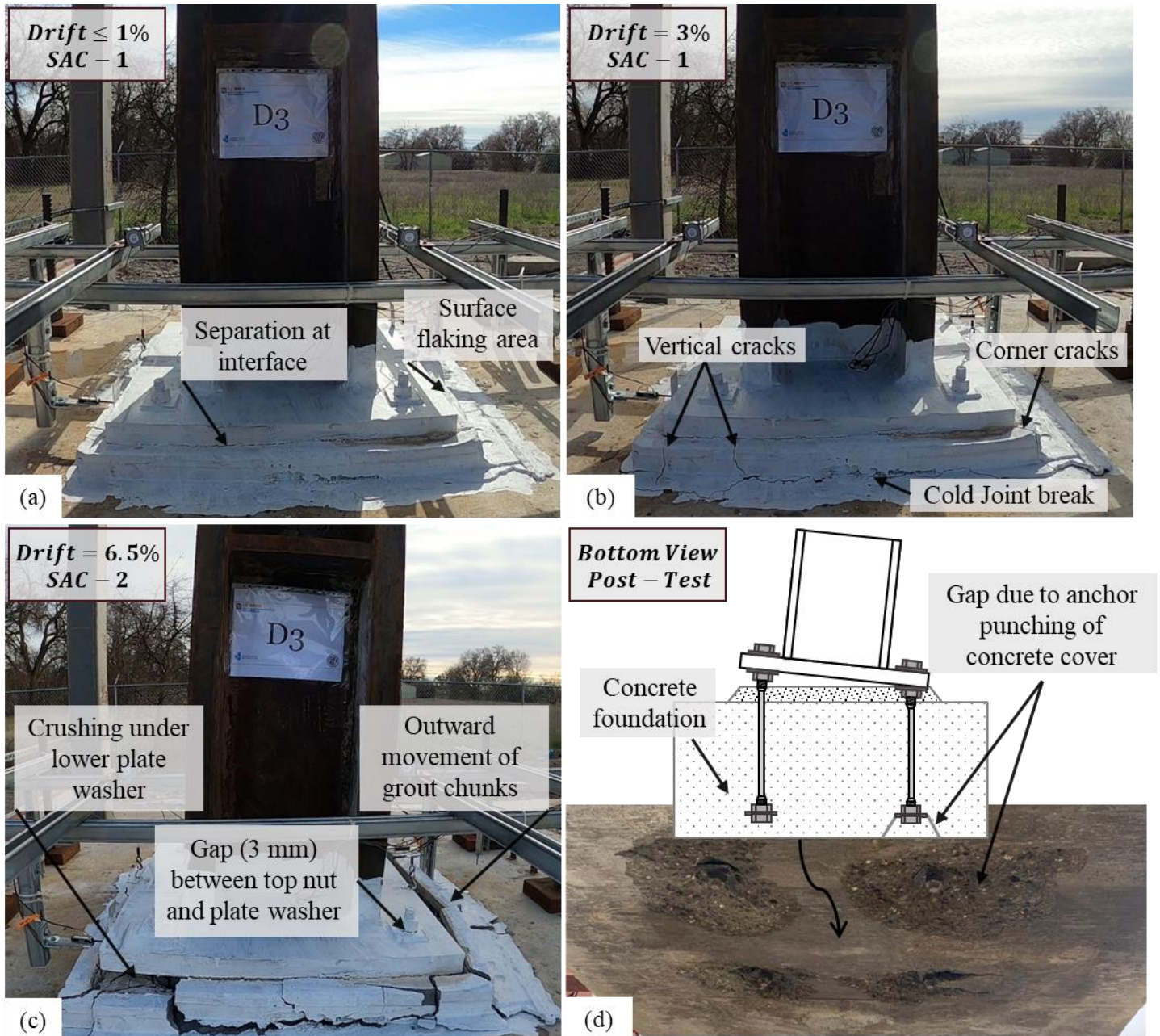


Figure 2.7 – Typical/observed damage progression for one of the tested specimens (Test #3).

2.5 SIMULATIONS TO ASSESS DEFORMATION CAPACITY OF UNTESTED CONFIGURATIONS

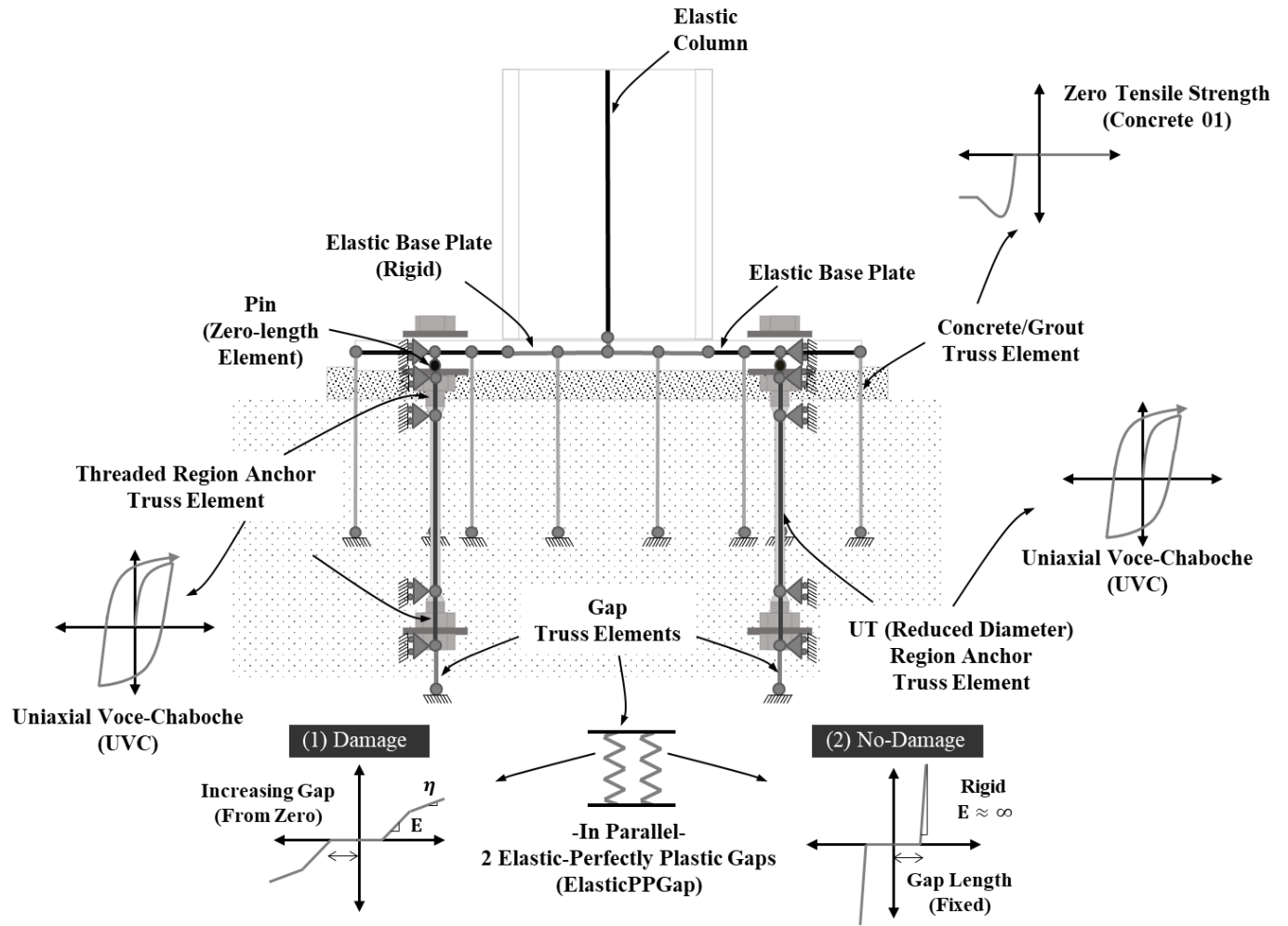
Simulations complementary to the experiments were conducted to examine the degree to which the high deformation capacity of the tested specimens may be generalized to untested

configurations. This included: (1) Line Element Based (LEB) models to infer the deformation histories in the anchor rods, (2) estimation of damage in the rods based on the deformation histories estimated from the LEB models; and (3) parametric assessment of this damage across various configurations.

Line Element Based simulations to characterize anchor deformation histories

Figure 2.8 schematically illustrates a representative two-dimensional Line-Element Based (LEB) model constructed using the OpenSees (v.3.2.1) platform (McKenna et al. 2012) to determine the deformation histories of the anchor rods. This model follows the methodology outlined by Inamasu et al. (2021). Referring to Figure 2.8, the base connection is represented through an assembly of uniaxial springs and beam-column elements; these include:

1. *Beam-column elements to represent the base plate as well the column:* These components are simulated as elastic recognizing that dissipative base connections will be designed to concentrate inelastic response only in the UT region of the anchor rods. The beam-column elements representing the plate in the flap region outside the W-section assume an effective width equal to the entire plate width, assuming that the high flexural rigidity of the plate minimizes bending in the out of plane direction. Within the W-section region, the beam-column elements representing the plate are modeled as rigid.
2. *Uniaxial spring elements to represent the bearing response of the footing:* A total of 20 such elements are used (not all shown in Figure 2.8 for clarity), each representing the response of a segment of the footing. The Zero Tensile Strength material model (Kent-Scott-Park Concrete Material (Kent and Park 1971; Scott et al. 1982) – implemented as “Concrete01” in OpenSees) is used to represent concrete/grout response. This model captures important aspects of footing



Parameters for Gap Element			
Parameter		Value	Rationale
Stiffness of gap material [kN/mm]	E_{gap-1}	175000	Calibrated to match test data
	E_{gap-2}	$\approx \infty$	Laboratory strong floor stiffness
Yield force of gap material [kN]	F_{ygap-1}	106	Concrete end blowout strength as per the ACI 318-19 provisions (ACI 2019)
	F_{ygap-2}	$\approx \infty$	Laboratory strong floor stiffness
Gap length [mm]	δ_{gap-1}	0	Initial condition (no gap)
	δ_{gap-2}	13	Gap length after test completion (concrete cover)
Material hardening ratio	η_{gap-1}	0	No hardening for gap growth (elastic perfectly-plastic)
	η_{gap-2}	1	Laboratory strong floor stiffness (almost elastic)

Figure 2.8 – Schematic illustration of the two-dimensional Line-Element Based (LEB) simulation model with element and material definitions.

behavior, including softening due to crushing, the absence of tensile strength (that results in gapping between the plate and concrete/grout), and strength degradation due to cyclic loading.

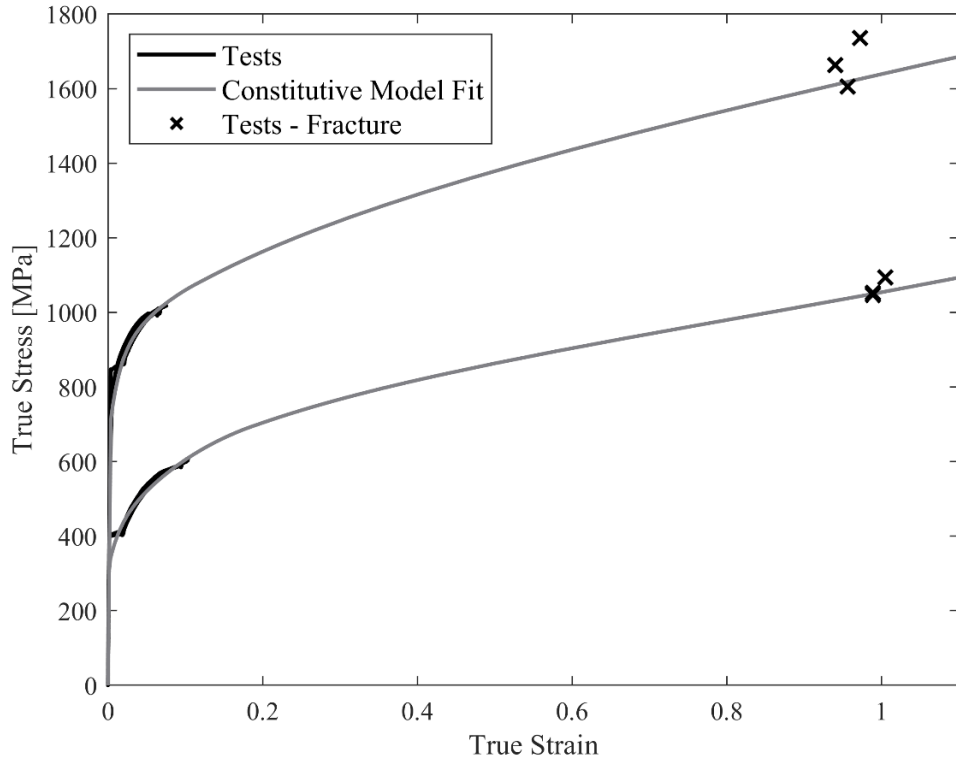


Figure 2.9 – Comparison of uniaxial coupon test data and constitutive model fit for the ASTM F1554 (Grade 55 and 105) rods.

The parameters of the concrete and grout were calibrated based on cylinder tests as follows: compressive strength, $f_{pc} = 58.6 \text{ MPa}$, compressive strain at maximum strength, $\varepsilon_{c0} = 0.003$, crushing strength, $f_{pcU} = 6.89 \text{ MPa}$ and compressive strain at crushing strength, $\varepsilon_U = 0.005$. It is important to note here that the softening properties of the concrete response imply a length scale over which softening (and hence localization) occurs (Bazant 1976). Consequently, the parameters controlling this (specifically f_{pcU} and ε_U) are calibrated to fit the load-displacement response of the test data.

3. *Uniaxial spring elements to represent the anchor rods:* Each anchor rod was simulated as an assembly of three springs (represented by uniaxial truss elements) in series. Of these, the element in the center represents the UT section over which the plastic deformations concentrate – the effective diameter for this element was set equal to the reduced diameter size from the tests (12.7 mm for Test #1 and 19 mm for Tests #2, 3 and 4). The two outer springs represented the threaded region of the rod outside this length. For these, the diameters were set equal to 16

mm for Test #1 and 22.3 mm for Tests #2, 3 and 4. The constitutive response of the steel material was represented through the Voce-Chaboche model (Voce 1948 and Chaboche et al. 1979), implemented in OpenSees as Updated Voce-Chaboche “UVCuniaxial” (de Castro e Sousa et al. 2020). The parameters of this model (which includes combined isotropic and two-backstress kinematic hardening) were calibrated as the following: elastic modulus of steel, $E_{rod} = 200000 \text{ MPa}$; initial yield stress of steel, $f_y^{rod} = 405.5 \text{ MPa}, 775 \text{ MPa}$; maximum increase in yield stress due to isotropic hardening $Q_\infty = 0.07 \text{ MPa}$; isotropic hardening saturation rate $b = 0.54$; kinematic hardening parameters $C_1 = 6550 \text{ MPa}, 11721.1 \text{ MPa}$, $C_2 = 173.1 \text{ MPa}, 138 \text{ MPa}$; $\gamma_1 = 61.8, 72.8$ and $\gamma_2 = 13.5, 40.57$. The two values for some of these parameters are for the Grade 55 and 105 steels, respectively. The monotonic parameters (E_{rod} , f_y^{rod} , and f_u^{rod}) as well as the C_1 and C_2 parameters were calibrated to match the response of uniaxial coupon tests conducted on unthreaded rod material as shown in Figure 2.9, whereas the remaining parameters were adopted from the study of de Castro e Sousa et al. (2020). Referring to Figure 2.9 (see the X-markers), the complete true stress-strain response (which includes information even after necking and extensometer) was inferred by measuring the force at fracture, and the corresponding post-fracture necked diameter.

4. *Gap elements*: Referring to prior discussion, gapping was observed at the bottom of the anchor rod due to punch-out of the concrete cover in the footing (Figure 2.7d). This gapping accommodates overall deformations of the connection and has the potential to decrease the strain demands in the designated stretch length of the rod for a given magnitude of connection rotation. The gapping at the bottom was represented through an assembly of two springs in parallel attached in series with the bottom end of the anchor rod springs (as shown in Figure 2.8). Each spring is represented through a tension/compression Elastic-Perfectly Plastic Gap

material implemented in OpenSees as “ElasticPPGap”. When represented in this way, the spring arrangement activates the gap at a pre-determined level of compressive force (corresponding to the punch-out of the concrete), and then increases the gap dimension each time additional damage is accumulated during subsequent cycles. The maximum gap dimension in the downward direction corresponded to the distance at which the bottom of the rod would impinge the strong floor. Figure 2.8 includes an inset table in which the various LEB gap parameters are summarized, with the rationale for their selection.

Using the above approach, LEB models were constructed complementary to the four full scale experiments. These simulation models were subjected to the axial load and lateral loading protocols as applied to the experimental specimens. Figures 2.10a-d compare the load-deformation response for each test to the corresponding response as determined from the LEB models. Referring to the figures, the LEB models simulate the overall load-deformation response with accuracy, including the various transition points that correspond to contact/gapping between the plate and concrete and the anchor and strong floor (i.e., gap closure). The sharp kinks in the simulated curves arise due to the placement of bearing springs at discrete locations; this response is smoothened if more springs are added. Referring to Figure 2.10a, the higher values of moment from the test compared to the simulation results is possibly attributed to asymmetry in the direction of loading for this specific specimen (Test #1) – particularly some additional grout was deposited on one side versus the other. However, the model is able to simulate the moment values, as well as the hysteretic behavior (loading and unloading branches) on the negative side with good accuracy. As an additional source of validation, similar agreement was found for the evolution of other experimental quantities for all tests, including the vertical motion of the base connection at

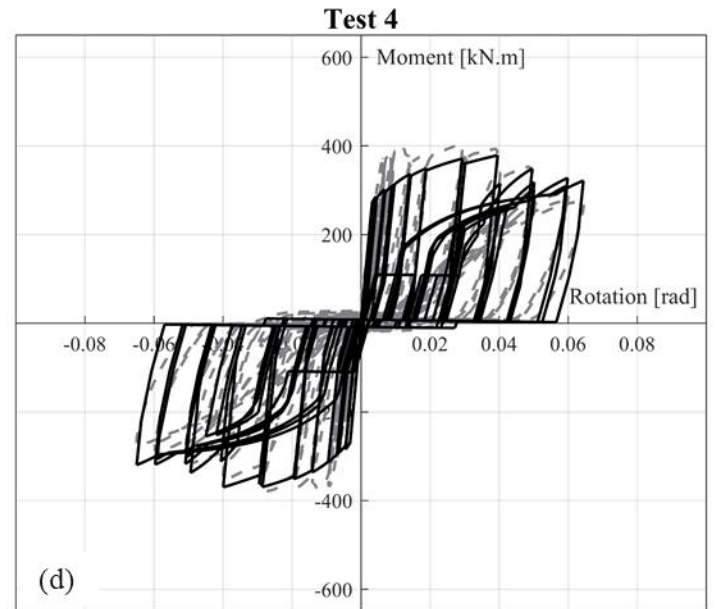
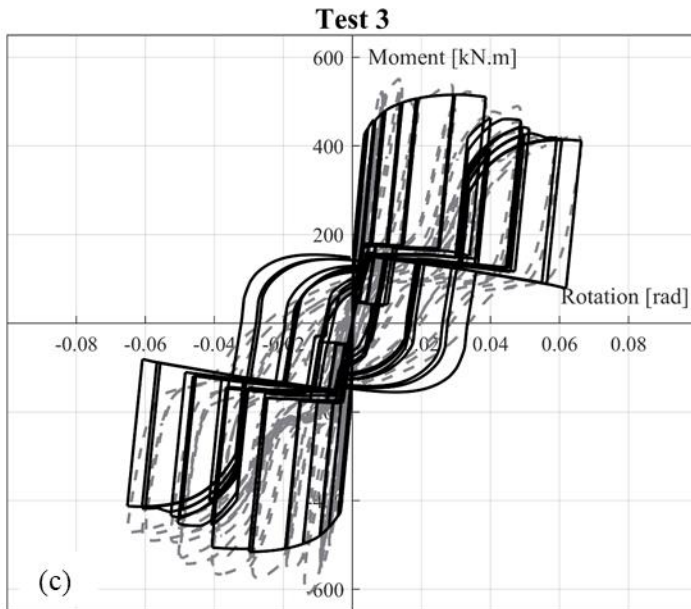
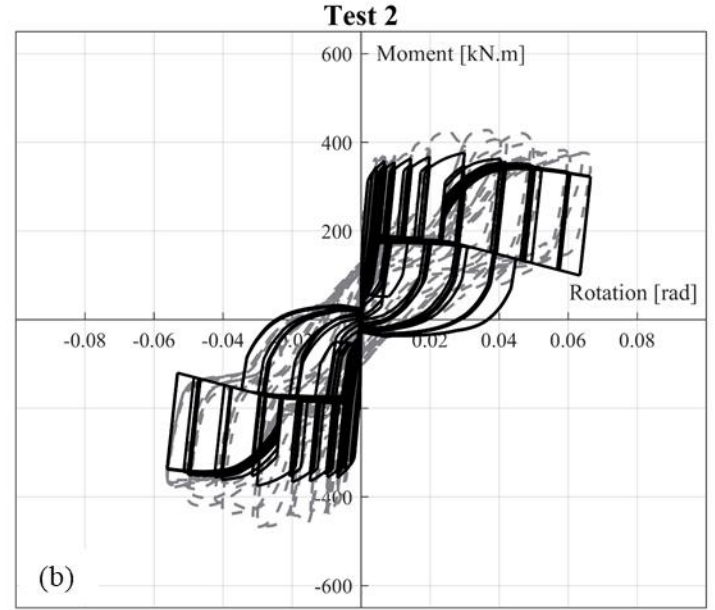
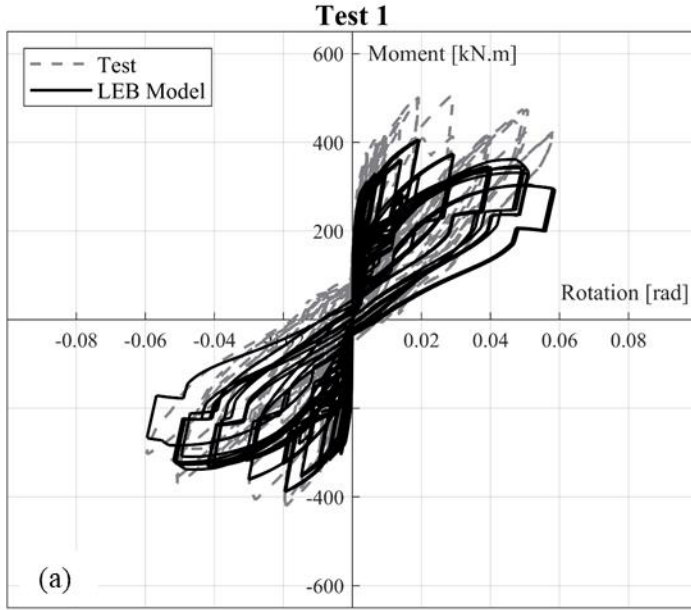


Figure 2.10 – Moment-Rotation curves for the 4 tested specimens and their corresponding curves recovered from LEB model.

the location of the anchor rods, as shown in Figures 2.11a-d. The vertical motion at this location is a direct indicator of the anchor rod deformations that are used for assessing their capacity. In this context, the vertical displacement, as predicted by the LEB model (corresponding to anchor rod tension at a drift of 4%) is within 7% of the experimental displacement.

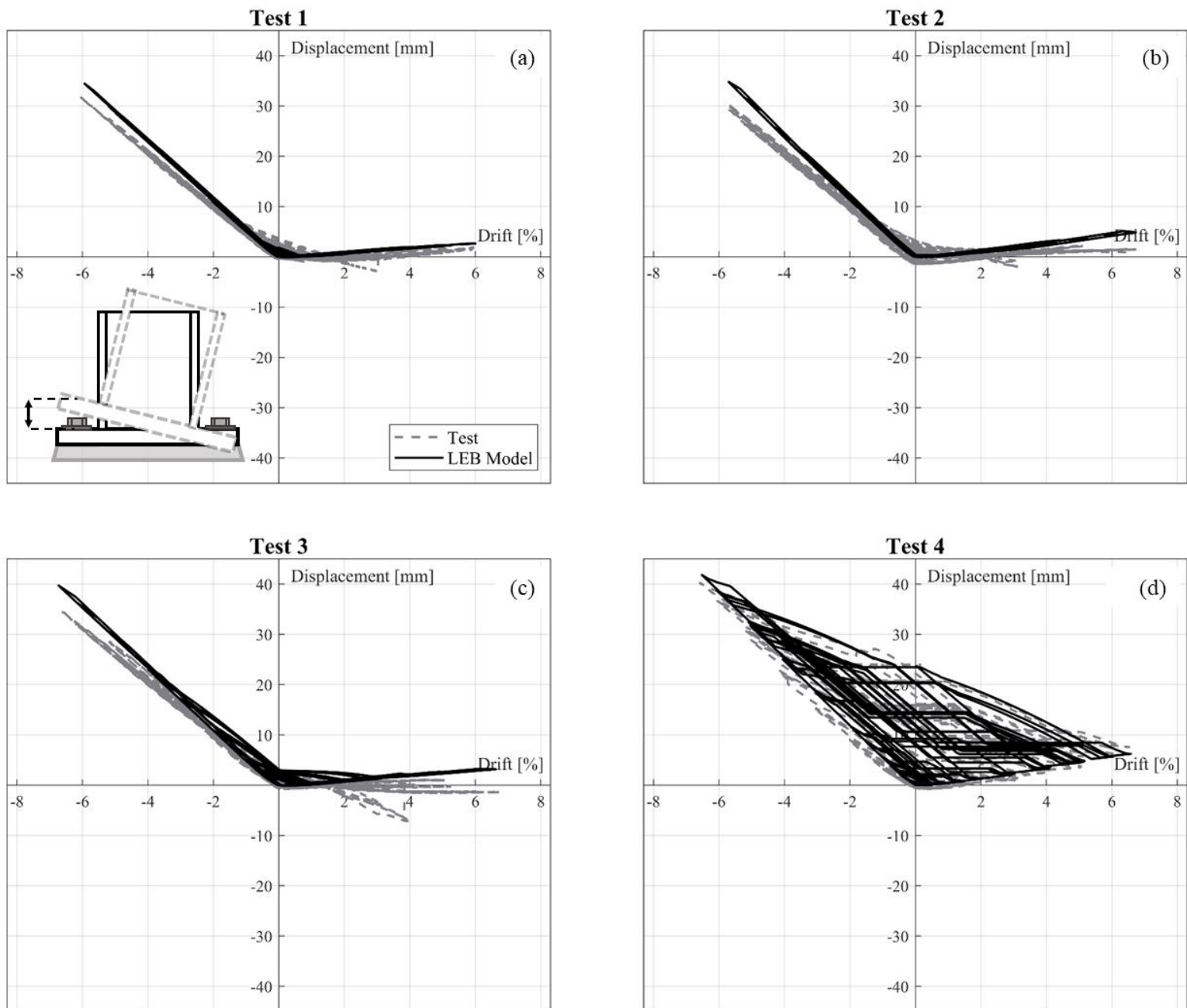


Figure 2.11 – Vertical displacement history of the base plate at anchor rod location plotted against column drift from tested specimens and LEB models.

This, along with the agreement in the load-deformation response suggests that the LEB models effectively represent the physics of connection response and may be used to characterize the load deformation response and anchor deformation histories. Once validated, the simulation approach was used for parametric simulation of configurations that were not tested physically. Table 2.4

summarizes all the parameter sets (including those complementary to the physical experiments) for which the LEB models were constructed. Referring to Table 2.4, these parameter sets include:

- Additional base plate sizes, since the base plate size (specifically the length N) directly influences the kinematic relationship between the connection rotation and rod deformation.
- Situations in which there is no gapping below the anchor, to examine a more conservative condition with respect to strain accumulation in the anchors. This may occur when a large concrete cover below the bottom end of the anchor prevents blowout. Two values of $\delta_{gap} = 13 \text{ mm}$ (similar to experiments) and $\delta_{gap} = 0 \text{ mm}$ (no gap) were examined.
- Additional values of the anchor rod diameters and the stretch length L_{UT}^{rod} .

Each of the LEB models in Table 2.4 was subjected to cyclic column lateral deformations consistent with two ATC-SAC protocols applied consecutively followed by additional cycles to 6.5% drift – identical to the drift histories applied to the experiments (illustrated previously in Figure 2.5). Anchor rod deformation histories were extracted from each run. Figure 2.12 shows two such deformation histories plotted against the cumulative drift applied at the top of the column. One history corresponds to Test #2 (i.e., Simulation #18 in Table 2.4). The other history is for an identical configuration, albeit with δ_{gap} set to 0 (Simulation #19). Both deformation histories show only the deformations of the anchor rod (UT region), excluding the gapping displacements – since only these deformations contribute to damage and eventual failure of the anchor rod. Referring to Figure 2.12, two observations may be made:

- Although the column deformations are symmetric, for Simulation #18 (with gap) during the initial cycles of loading, the rod elongations ratchet in the tensile direction. This may be attributed to the gradually opening gap below the anchor rod, which prevents full recovery of compressive deformations. In fact, as indicated in Figure 2.12, the saturation value of the gap

(i.e., $\delta_{gap} = 13 \text{ mm}$) is consistent with the irrecoverable deformation in the anchor. Referring to the “no-gap” deformation history (Simulation #19), it is apparent that all the deformation is recovered during compressive cycles, as expected.

- A consequence of the above behavior is that although the cumulative plastic strain in the no-gap situation is larger, the peak tensile plastic strain is virtually identical between the gap and no-gap situations; this observation is consistent across all the parameter sets studied.

Damage assessment in anchor rods

The anchor rod deformation histories recovered from each of the parametric simulations may be used to infer damage in the anchor rods. Based on observations of failure in previous EBP experiments (Gomez et al., 2010; Trautner et al., 2017), and of similar steel components subjected to cyclic loading (e.g., Kanvinde 2004 for steel rods; Terashima 2018 for buckling restrained braces) two relevant damage/failure modes are considered: (1) necking of the anchor rods in the UT section, which leads to strain accumulation and fracture, and (2) Ultra Low Cycle Fatigue (ULCF) fracture of the anchor rods which may occur without necking, due to plastic strains accumulated homogenously over the UT length. Each of these is now discussed.

- *Necking induced failure:* Previous experiments on EBP connections as well as cyclically loaded steel rods indicate that necking (which occurs on a tensile excursion) results in loss of strength, and rapid localization of strains within the necked region, ultimately leading to fracture. It is well established (Considère 1885) based on volume conservation arguments that necking instability in axially loaded bars occurs when the instantaneous true longitudinal stress in the rod exceeds the instantaneous tangent modulus of the material, expressed mathematically as $\sigma_{true} \geq (d\sigma_{true}/d\varepsilon_{true})$. In this expression, the true stress and strain are functions of the

engineering values as $\sigma_{true} = \sigma_{eng} \times (1 + \varepsilon_{eng})$, and $\varepsilon_{true} = \ln(1 + \varepsilon_{eng})$. The main implication is that in cyclically loaded rods, history effects are not important, because only the instantaneous values of stress and the tangent modulus control the necking instability. To examine this further, Figure 2.13 plots the true stress-strain curves for two of the simulations whose deformation histories were shown earlier in Figure 2.12. Stress-strain curves for all parametric simulations are qualitatively similar. Referring to Figure 2.13, two points are evident. First, from the standpoint of predicting necking, which occurs at strains greater than 0.1, the hysteresis loops are fully stabilized for both the gap and no-gap situations. Due to this loop-stabilization, the tensile strain interpreted in a monotonic manner (disregarding history effects) is an accurate predictor of the instantaneous stress, as well as the tangent modulus. Second, for a given connection rotation, the tensile strain is virtually identical between the gap and no-gap situations, even if the accumulated strain is different. Based on the above observations, the following damage index is proposed for necking:

$$D_{neck} = \varepsilon_{max} / \varepsilon_{neck} \quad (2.1)$$

In the above, ε_{max} is the maximum tensile strain encountered until any point in the loading history of the UT section in LEB model, whereas ε_{neck} denotes the value of strain at which necking would initiate, such that $D_{neck} = 1$ predicts necking. For each steel grade, the value of ε_{neck} is inferred from the maximum elongation values in ASTM 1554 (2020). Specifically, the failure elongations implied in ASTM 1554 correspond to a standard tensile test. The failure elongation may be decomposed as follows:

$$\Delta_{failure} = \Delta_{neck} + \Delta_{post-neck} \quad (2.2)$$

In the above, Δ_{neck} represents the deformations up to the point of necking, and $\Delta_{post-neck}$ represents the post-necking deformations to fracture. Of these, Δ_{neck} corresponds to a state of

uniform strain over the gage length, whereas $\Delta_{post-neck}$ corresponds to localized deformations and has been shown to be independent of gage length for a given rod diameter (e.g., see Kolwankar et al. 2017). Consequently, Equation 2.2 above may be simplified to:

$$\varepsilon_{max} \times L_{gage} = \varepsilon_{neck} \times L_{gage} + \Delta_{post-neck} \quad (2.3)$$

For each steel grade, ASTM 1554 provides two values of ε_{max} , for two gage lengths. These values may be used in conjunction with Equation 2.3 above to eliminate $\Delta_{post-neck}$, and estimate ε_{neck} . The computed values of ε_{neck} are as follows: 0.17 for the Grade 55 anchor rod, and 0.11 for the Grade 105. Once ε_{neck} is thus calibrated, the damage index D_{neck} and its evolution may be determined for each of the simulations; see Figure 2.14 for an illustration of one such evolution of D_{neck} (for Simulation #18).

- *Ultra Low Cycle Fatigue Failure:* In situations where no single tensile cycle is large enough to trigger necking, Ultra Low Cycle Fatigue (ULCF) fracture may still occur due to cyclic plastic strains that accumulate in a homogenous manner over the entire UT region (rather than localize due to necking). Numerous continuum damage mechanics-based criteria have been proposed to predict ULCF fracture – Kanvinde (2017) provides a comprehensive review. In this work, ULCF damage was assessed based on the Stress Weighted Damage Fracture Model (SWDFM) proposed by Smith et al. (2021), which has been extensively validated against experimental data from structural steels. The original SWDFM model includes continuum stress invariants, including stress triaxiality and the Lode parameter – see Smith et al. (2021) for the detailed expression. However, for the uniaxial cyclic case with an axisymmetric state of stress (for which the triaxiality alternates between +1/3 and -1/3 for tension and compression, and the absolute value of Lode parameter equals 1), the fracture (or damage)

criterion corresponding to the SWDFM may be represented as the following damage index, which predicts ULCF when it exceeds 1:

$$D_{ULCF} = \int_0^{\varepsilon_p} C \times [2 \times \exp(1.3 T) - \exp(-1.3 T)] \times d\varepsilon_p \quad (2.4)$$

All terms in the above equation may be known or readily calculated from the stress-strain histories determined from the LEB simulations; specifically, T is the stress triaxiality that alternates between $\pm 1/3$ for tension and compression, $d\varepsilon_p$ is the incremental plastic strain, and C is a material parameter. Based on data reported for various materials by Smith et al. (in press), the parameter C is selected as 0.31 (the highest reported value in literature) to conservatively estimate the ULCF damage. Based on this, Figure 2.14 also shows the evolution of D_{ULCF} for Simulation #18, overlaid on the evolution of D_{neck} shown previously.

Both the LEB models and the above damage measures based on them assume that the anchors undergo purely axial deformations in tension and compression. However, the rotation of the base plate produces small lateral deformations at the top of the anchor rod (due to the arcing effect), resulting in bending strains and stresses. To examine whether this influences strains in the UT region, 6 Continuum Finite Element (CFE) simulations were conducted using the ABAQUS (v.6.14) simulation platform (2014). These simulations interrogated: (1) column sizes (W14x370 and W8x48); (2) base plate footprints (762x762 mm² and 356x356 mm²); (3) anchor rod grades (ASTM F1554 Grade 55 and Grade 105), diameters (25.4 mm with UT diameter of 19.1 mm and 19.1 mm with UT of 12.7 mm); and (4) axial loads (in the range of 0 to 534 kN) and loading heights (2.3 to 3.4 m). Each of the simulations was subjected to displacement-controlled lateral loadings until necking was observed in an anchor rod. The CFE models can simulate necking in the rods, because they use large-deformation continuum elements to represent the rods. Key aspects of connection physics were simulated following best-practices outlined previously by

Kanvinde et al. (2013); these include (1) all geometric aspects including nut-washer assemblies at the end of the rods, and the transitions at the ends of the UT; (2) appropriate constitutive properties of all materials – specifically the Armstrong Frederick model for steel (1966), which is the multiaxial analogue of the UVC model used in the LEB simulations, and an elastic model for the concrete; and (3) frictionless hard contact between the anchor and the concrete/grout. Figure 2.15 illustrates the plastic strain contours in one such model after necking initiation in the anchor rod. Referring to the figure, the maximum strains occur in the UT region of the rod, and the bending in this region is negligible.

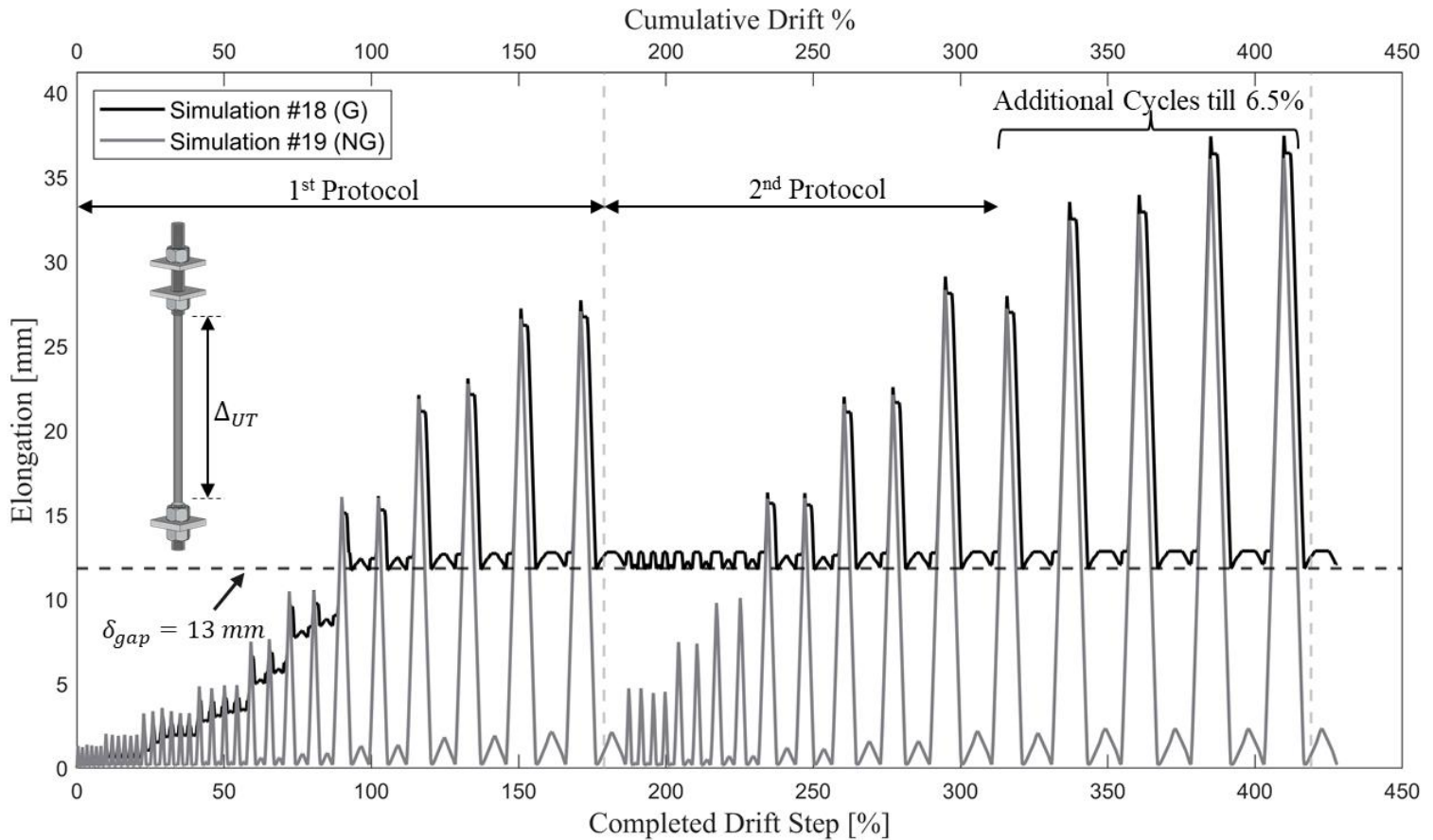


Figure 2.12 – Anchor rod elongation history plotted against cumulative drift.

Table 2.4 – Simulation Matrix and Results

Simulation ^a #		N ^d [mm]	P [kN]	L ^{rod} _{UT} [mm]	d ^{rod} _{threaded} [mm]	d ^{rod} _{UT} [mm]	Rod Gr. ^e	D ^{SAC-1} _{neck} ^f		D ^{SAC-2} _{neck} ^g		D ^{SAC-1} _{ULCF} ^f		D ^{SAC-2} _{ULCF} ^g		$\frac{M_{4\%}^{simulation}}{M_{max}^{simulation}}$ ^h	
G	NG							G	NG	G	NG	G	NG	G	NG		
1	2	1016	890	508	35	31.8	105	0.65	0.65	0.88	0.87	0.10	0.20	0.33	0.63	0.96	1.00
3	4			381				28.7	25.4	0.86	0.86	1.16	1.16	0.14	0.28	0.45	0.85
5	6				0.92	0.91				1.22	1.22	0.13	0.33	0.29	0.95	0.98	0.98
7	8				55	0.62	0.61	0.81	0.81	0.19	0.42	0.60	1.15	0.93	0.96		
9	10		1779		35	31.8	105	0.82	0.82	1.13	1.13	0.13	0.27	0.43	0.83	0.94	0.98
11	12			55			0.57	0.57	0.77	0.77	0.17	0.36	0.54	1.03	0.92	0.96	
13	14			28.7	25.4	105	0.87	0.87	1.18	1.18	0.15	0.31	0.47	0.92	0.92	0.96	
15	16					55	0.59	0.59	0.79	0.79	0.18	0.39	0.57	1.09	0.90	0.93	
17 ^b	-	762	534	419	16.5	12.7	55	0.42	-	0.48	-	0.29	-	0.67	-	0.80	-
18 ^b	19			381	22.3	19		0.48	0.46	0.64	0.61	0.14	0.34	0.41	0.91	0.95	0.97
20 ^b	-		0				105	0.70	-	0.94	-	0.08	-	0.20	-	0.92	-
21 ^b								0.77		0.98		0.08		0.19		0.96	
22	23		890				381	16.5	12.7	105	0.68	0.67	0.89	0.89	0.09	0.25	0.29
24	25			55	0.45	0.44				0.59	0.58	0.12	0.32	0.36	0.85	0.89	0.93
26	27			105	0.69	0.69				0.91	0.90	0.18	0.27	0.39	0.75	0.88	0.90
28 ^c	29			55	0.45	0.45				0.59	0.59	0.32	0.33	0.85	0.88	0.85	0.85
30	31	508	223	508	22.3	19	55	0.24	0.23	0.31	0.30	0.04	0.13	0.10	0.38	0.95	1.00
32	33			381		15.9		0.31	0.30	0.41	0.40	0.06	0.18	0.14	0.51	0.97	0.98
34	35						105	0.47	0.46	0.63	0.62	0.04	0.14	0.10	0.43	0.98	0.97
36 ^c	37						55	0.31	0.30	0.41	0.40	0.18	0.19	0.51	0.54	0.97	0.98
38	39		667				19	105	0.41	0.41	0.56	0.56	0.03	0.11	0.08	0.36	0.92
40	41			55		0.28		0.28	0.38	0.37	0.05	0.16	0.13	0.46	0.81	0.83	
42	43			105		0.43		0.43	0.57	0.57	0.04	0.13	0.09	0.38	0.87	0.85	
44 ^c	45			55		0.29		0.29	0.38	0.38	0.16	0.17	0.46	0.49	0.78	0.79	
46	47	356	400	305	16.5	15.9	105	0.30	0.31	0.43	0.44	0.02	0.07	0.03	0.22	0.96	0.92
48	49			381		12.7		0.25	0.26	0.35	0.36	0.02	0.05	0.03	0.17	0.96	0.92
50	51						55	0.28	0.28	0.38	0.38	0.06	0.06	0.15	0.21	0.87	0.87
52 ^c	53						105	0.19	0.19	0.25	0.25	0.09	0.09	0.27	0.29	0.78	0.78
54	55		667				15.9	55	0.23	0.23	0.32	0.33	0.02	0.04	0.02	0.15	0.90
56 ^c	57			55		0.17		0.17	0.23	0.23	0.07	0.07	0.22	0.24	0.80	0.80	
58	59			105		0.25		0.25	0.35	0.35	0.05	0.06	0.15	0.19	0.82	0.82	
60 ^c	61			55		0.17		0.17	0.23	0.23	0.08	0.08	0.25	0.26	0.73	0.73	

^a G = “with gap of length 13 mm”; NG = “with no gap”

^b Simulations represent the tested specimens (Tests #1,2,3 and 4 respectively).

^c Bottom gap was not fully activated for these simulations.

^d Base plate dimensions $N \times B \times t_p$ and (column profile): 1016 × 610 × 102 mm (W24 × 176); 762 × 762 × 51 mm (W14 × 370); 508 × 508 × 51 mm (W12 × 96); 356 × 356 × 51 mm (W8 × 48) for $N = 1016, 762, 508$ and 356 mm, respectively.

^e ASTM F1554 Anchor rod grade with $f_y^{\text{rod}} = 405$ and 775 MPa for grades 55 and 105, respectively.

^f The maximum necking and ULCF damage indices observed before the end (5% cycles) of the first application of the SAC protocol (SAC-1).

^g The maximum necking and ULCF damage indices observed before the end of the second application of the SAC protocol (SAC-2) and the additional cycles till 6.5%.

^h The ratio between the base moment at 4% drift during the first application of the SAC protocol (SAC-1) and the maximum moment, observed during the simulations.

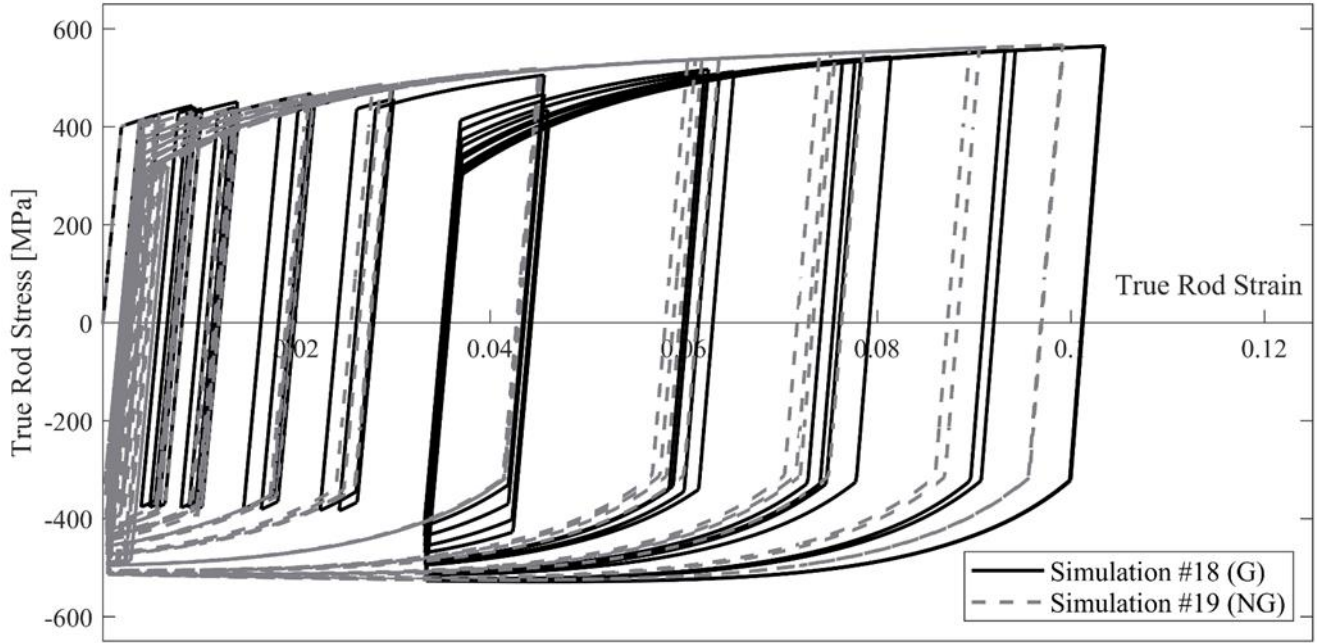


Figure 2.13 – Anchor rod true stress-strain curves, for Simulations #18 and 19 (G and NG).

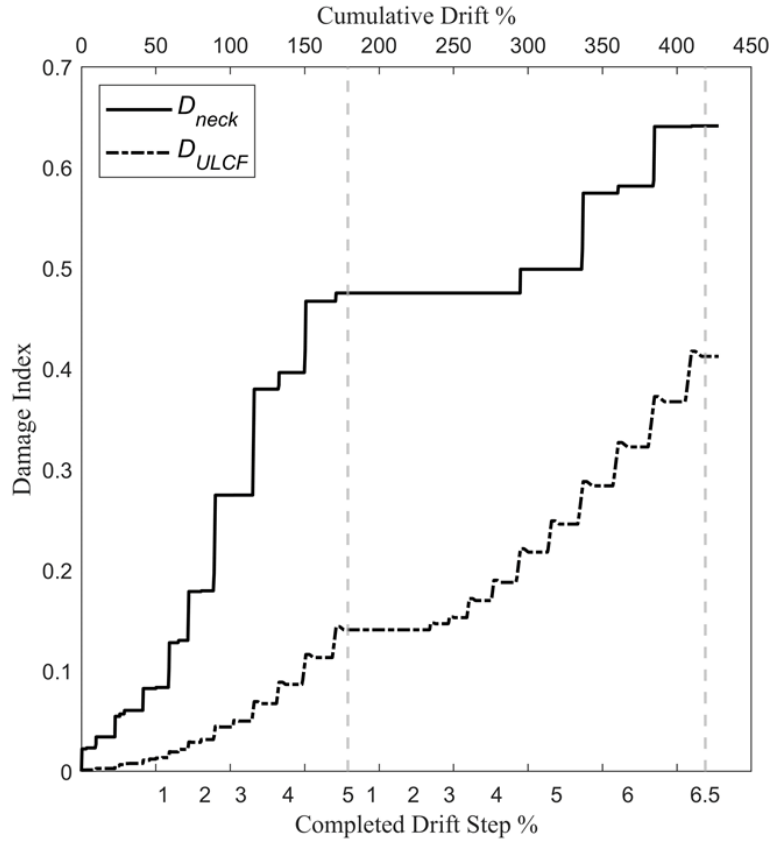


Figure 2.14 – Evolution of D_{neck} and D_{ULCF} for Simulation #18 (G); vertical dashed lines indicate completion of first and second loading protocol.

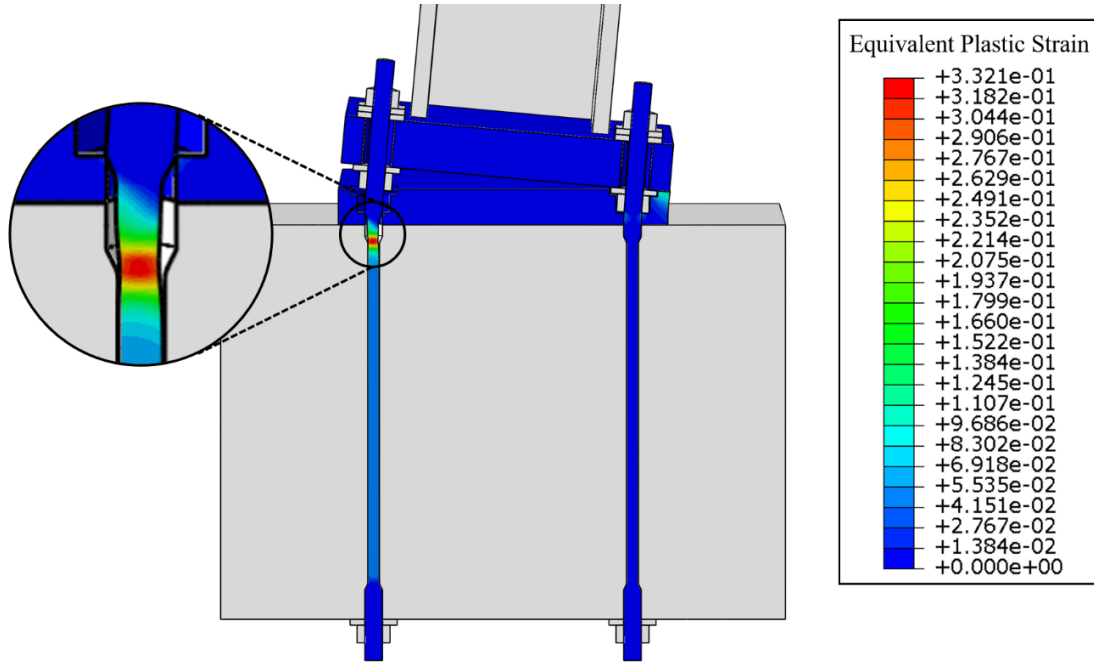


Figure 2.15 – Plastic strain contours from CFE simulation showing necking in the UT region of the rod.

Additionally, a series of 32 CFE component simulations (including the UT region of the anchor rod and the surrounding concrete – see Figure 2.16a) were conducted to examine the validity of the proposed necking damage index D_{neck} . The three-dimensional CFE models feature a frictionless interface between the rod and concrete surface, and are able to directly simulate necking in the rods following a well-established, and validated methodology for simulating tensile necking (e.g., see Terashima 2018) because they can represent the diametral reduction of the rods, and its interaction with constitutive response. Moreover, the models do not require the introduction of a diametral imperfection to initiate the necking instability, because mild gradients in the longitudinal stress field (owing to boundary condition effects at the end of the rods) are sufficient to initiate the instability.

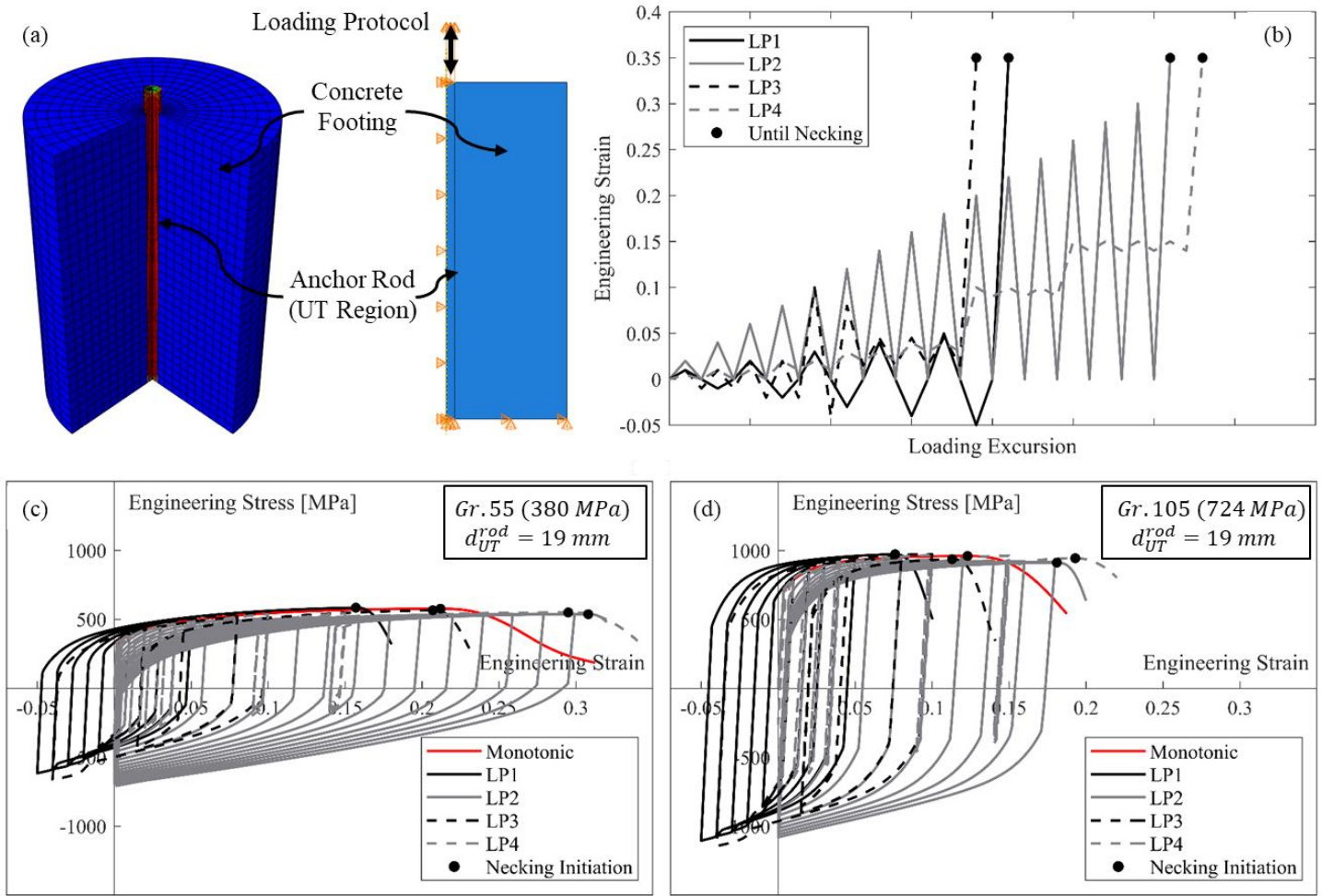


Figure 2.16 – CFE simulations for necking damage measure validation: (a) CFE model for anchor rod with surrounding concrete; (b) Loading protocols under investigation; (c) stress-strain curves for rods of same diameter size (19 mm), subjected to monotonic and cyclic loading protocols, for Grade 55; and (d) Grade 105

Necking instability is detected in the rods when the tensile force (or the effective engineering stress) begins to reduce; this is usually followed by visual observation of a neck in the rod. Using this simulation methodology, two rod grades (ASTM F1554 Grade 55 and Grade 105), four UT region diameters (12.7 mm, 19.1 mm, 25.4 mm, and 31.8 mm) and four cyclic deformation loading protocols/histories (see Figure 2.16b) were considered. For the purposes of illustration, Figures 2.16c-d plot representative engineering stress-strain curves for these rods as inferred from the CFE models. These are shown for one UT diameter (19.1 mm), and two different grades subjected to the cyclic and monotonic loading protocols. The values of strains at which necking initiates (indicated by a drop in engineering stress, and denoted as ϵ_{neck}^{CFE}) are recovered from all the

simulations. A survey of these values reveals that the ε_{neck}^{CFE} as inferred from CFE simulations are significantly larger than the previously computed/calibrated values from ASTM 1554 (denoted hereafter as $\varepsilon_{neck}^{ASTM}$) for both grades. The average $\varepsilon_{neck}^{CFE}/\varepsilon_{neck}^{ASTM}$ is 1.55 with a CoV of 0.17, and 1.44 with a CoV of 0.22 for Grades 55 and 105, respectively. This is not surprising, given that the ASTM values represent minimum values. This suggests that the proposed necking damage index is relatively conservative, i.e., for the rod materials tested herein, necking is likely to occur at significantly greater strains than implied by $\varepsilon_{neck}^{ASTM}$. It is relevant to note here that, lower values of necking strain ε_{neck}^{CFE} (albeit still close to the $\varepsilon_{neck}^{ASTM}$) are generally observed in loading protocols in which the rod undergoes significant negative strain cycles (e.g., LP1 and LP3). In the context of anchor rod in exposed base connections, these strain cycles are highly unlikely/unrealistic. Both these observations (negligible bending effect, and the conservatism in necking damage index) lend support to the use of LEB-based damage measures used in this study.

Results and Discussion

The damage measures D_{neck} and D_{ULCF} may be applied to examine the deformation capacity of base connection details other than those that have been tested (i.e., those introduced previously in Table 2.4). Consequently, for each of the simulations in Table 2.4, values of both damage indices were recovered at specific instants. Referring to Table 2.4, these indices are denoted D_{neck}^{SAC-1} , D_{ULCF}^{SAC-1} , D_{neck}^{SAC-2} , and D_{ULCF}^{SAC-2} . Of these, the former two (superscript SAC-1) denote the maximum necking and ULCF damage indices observed before the end (i.e., 5% cycles) of the first application of the SAC protocol, whereas the latter two (superscript SAC-2) denote the maximum damage indices observed before the end of the second application of the SAC protocol and the additional cycles till 6.5%. The former may be considered damage at demands consistent with connection

pre-qualification, whereas the latter may be interpreted as damage at extreme demands or after multiple high-intensity earthquakes. Figures 2.17a-b plot results graphically. Referring to Table 2.4 and Figures 2.17a-b, the following observations may be made:

- For a large majority of the simulation sets (43 out of 61), all damage indices are below 1.0, indicating that the anchor rods are unlikely to exhibit either necking or ULCF fracture in most of the scenarios, even after two applications of the SAC protocol and the 6.5% cycles.
- All instances where either D_{neck} or D_{ULCF} exceeds 1.0 (see bold values in Table 2.4) occur only during the second application of the SAC loading history and only for the longest plate ($N = 1016$ mm). These are extreme situations, both in terms of the applied demands and base plate geometry. In fact, the highest value of either D_{neck} or D_{ULCF} during the first application of the SAC loading history is $D_{neck,max}^{SAC-1} = 0.92$ (for Simulation #5), indicating that none of the examined configurations fails during the first application of the SAC protocol.
- In 47 out of 61 simulations (including both the SAC-1 and SAC-2) the D_{neck} value is greater than the corresponding D_{ULCF} value, indicating that failure by necking is the more likely failure mode. The exceptions to this all occur in the no-gap simulations. This is not surprising because the plastic strain accumulation is greater than that in the simulations with the gap.
- Referring to Figures 2.12-2.14 and associated discussion, D_{neck} values (for both SAC-1 and SAC-2) are similar between the gap and no-gap simulations because the maximum tensile elongation is virtually identical between the two. However, the D_{ULCF} values are, on average larger for the no-gap simulations, in which the cyclic strain accumulation is more significant.
- It is relevant to note here that although the introduction of the gap (which was incidental for the tested specimens, owing to the small concrete cover under the anchor rod end) reduced the cumulative plastic strain accumulation and hence enhanced the overall deformation capacity

of the anchor rod; a punching shear failure at the bottom of the footing is typically undesired. This should be avoided through providing an adequate concrete cover and potentially supplementary reinforcement below the anchor rod/assembly (anchorage plate and nut) in accordance with ACI 318-19 (ACI 2019).

- Table 2.4 (last two columns) summarizes the values $M_{max}^{simulation}/M_{max}^{simulation}$ for each of the simulations; these are determined for the SAC-1 condition and are analogous to the $M_{4\%}^{test}/M_{max}^{test}$ values presented previously for the experimental data, and indicate the ability of the given detail to maintain flexural strength. Referring to this column, these values range between 0.73-1.0 (average of 0.9, with a CoV of 0.07 – similar to the physical experiments) suggesting that the connections continue to carry significant moments at 4% drift.

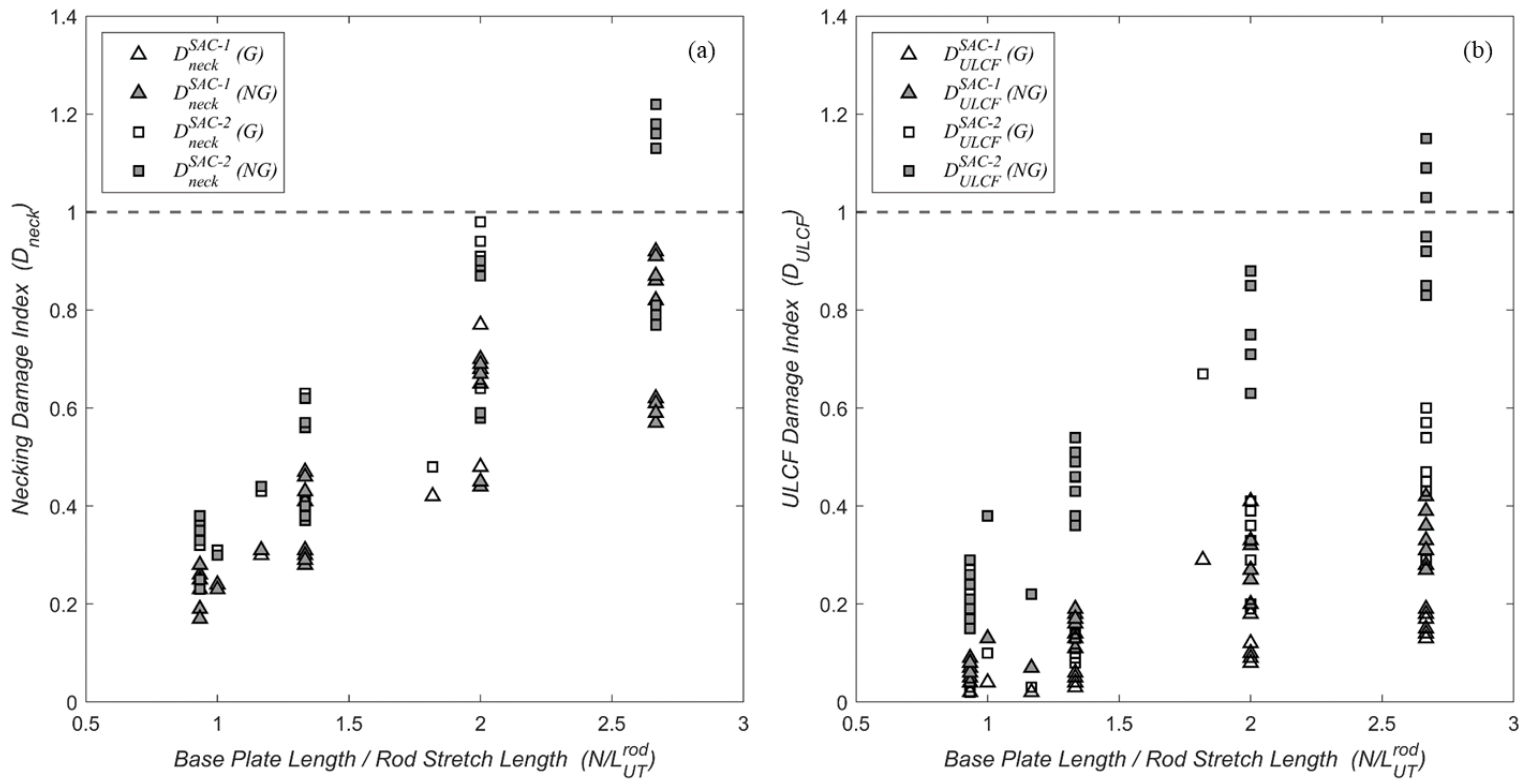


Figure 2.17 – Anchor rod damage measures (a) D_{neck} and (b) D_{ULCF} after each applied loading history versus N/L_{UT}^{rod} for all simulations.

Figures 2.17a and b plot all four values of the damage index, i.e., D_{neck}^{SAC-1} , D_{ULCF}^{SAC-1} , D_{neck}^{SAC-2} , and D_{ULCF}^{SAC-2} against the N/L_{UT}^{rod} . Referring to these figures, the following observations may be made. First, a strong positive trend is observed between all the damage indices and the plate length N/L_{UT}^{rod} . This is not unexpected, because the term N/L_{UT}^{rod} approximately reflects the kinematic relationship between connection rotation and the rod strain, wherein a high value of N results in greater rod deformation (for a given base rotation), which is then distributed over the length L_{UT}^{rod} . Second, it is noted that for N/L_{UT}^{rod} values less than 2.0, all damage index values are significantly lower than 1.0, indicating safety for these connections even in the SAC-2 case. Collectively, these observations provide preliminary guidance for sizing of L_{UT}^{rod} relative to the base plate dimensions.

2.6 SUMMARY AND CONCLUSIONS

Recent studies indicate that concentrating inelastic rotations in ductile column base connections (i.e., a weak-base design) in steel moment frames, rather than in the attached column may result in safe as well as economic connection design. This is a significant departure from the prevailing approach of designing the base to be stronger than the column. This study examines an exposed column base plate detail that can provide significant inelastic rotation capacity without failure. The detail concentrates yielding in Upset Thread (UT) anchors that provide a designated stretch length for distribution of strains and are frictionally isolated from the footing through the use of polyethylene tape. Other than these modifications, the detail is identical to conventional exposed base plate connections. Four full-scale experiments were conducted on these connections. In these tests, the main form of observable damage was the cracking and spalling of grout, accompanied by yielding of the anchor rods. Concrete punch-out was observed at the bottom of the specimens at the conclusion of the tests. None of the tests showed anchor fracture or any other form of

catastrophic failure. In terms of load-deformation response, the specimens showed an elastic response, followed by yielding and pinched hysteresis with cycle-to-cycle degradation due to the aforementioned damage mechanisms. Notwithstanding this degradation, the specimens were able to maintain significant flexural capacity throughout the loading. The experiments suggest that the Upset Thread (UT) detail is highly promising and can provide extraordinarily ductile response even under very high seismic demands.

A comprehensive program of simulations was carried out to examine to what degree the response of the physical experiments may be generalized to untested configurations. These simulations were verified against the physical experiments and then used to parametrically examine the effect of base configurations on connection response – specifically anchor rod failure. The results of this parametric study indicate that for the large majority of the cases, damage in the anchor is below its critical value, suggesting that they are unlikely to fracture. The cases in which anchor failure is predicted all correspond to the second application of the ATC-SAC loading history (no failure is predicted in any of the cases for the first application), and configurations in which the base plate length is at least twice as long as the stretch length, i.e., the term $N/L_{UT}^{rod} \geq 2.0$. In summary, the test and simulation program indicates that the UT detail is likely to provide ductile response under a wide range of configurations. Moreover, the parametric analysis indicates that limiting the ratio of base plate length to stretch length may be an effective strategy for controlling anchor rod strains, and mitigating failure.

The study has some limitations that must be considered while evaluating its results and, more importantly, design development; these limitations are now outlined. First, the performance of connections (as implied by both the tests and simulations) cannot be extrapolated to details that

that are significantly different than those examined – for example, alternate anchor rod patterns, material grades, or nut-washer assemblies may influence the deformation capacity of the rods. Perhaps most importantly, to achieve the observed performance, components of the base connection (i.e., base plate, welds) must be designed to concentrate yielding only in the anchor rods. Second, the tested details included a shear key that effectively transferred column shear to the foundation. The absence of such a mechanism may result in shear transfer through the anchors, compromising their deformation capacity. Regarding the simulations, it is important to recognize that they predict failure only in the anchor rods, and even for these, only two possible failure modes – assuming purely axial deformations. Moreover, the damage measures have not been independently verified against failure data of anchors, other than the observation that they predict no-failure in the configurations corresponding to the experiments. While these are supported by complementary CFE simulations and agreement with test data, it is not possible to rule out failure modes that may develop in untested configurations that are also not captured by the simulations. Thus, caution must be exercised in evaluating the results of the simulations. Finally, it is emphasized that the study focuses only on connection response, and does not consider its interactions with the frame. Designing connections to be weak may raise collateral issues, e.g., the concomitant decrease in flexural stiffness (see Falborksi et al. 2020) and a redistribution of forces and deformation demands in the connections.

CHAPTER 3

SEISMIC RESPONSE OF BLOCKOUT COLUMN BASE PLATE CONNECTIONS UNDER AXIAL COMPRESSION AND FLEXURE

This chapter presents the pre-print version of the article (to be revised and submitted) with the following full bibliographic details: Ahmad S. Hassan, Arka Maity, Paul Richards, and Amit M. Kanvinde (202X). “Seismic Response of Blockout Column Base Plate Connections under Axial Compression and Flexure.” Journal of Structural Engineering, American Society of Civil Engineers (ASCE).

3.1 INTRODUCTION

Exposed Column Base Plate (ECBP) connections are commonly used in steel construction to connect the column to the concrete footing (see Figure 3.1), and to transfer the forces from the entire frame into the foundation. Referring to Figure 3.1, these connections consist of a steel column welded to a base plate, which is then attached to a concrete footing using anchor rods. Given their prevalence and importance, they have been the subject of considerable study. These studies have included experimental (Astaneh et al. 1992; Burda and Itani 1999; Gomez et al. 2010; Kanvinde et al. 2015; Trautner et al. 2016; Hassan et al. 2022) as well as analytical (Ermopoulos and Stamatopoulos 1996) investigations, and have addressed strength models (Drake and Elkin 1999), stiffness models (Wald et al. 1995; Kanvinde et al. 2012), seismic performance (Trautner et al. 2017; Hassan et al. 2022), strength characterization of biaxially loaded (Hassan et al. 2021) details, as well as interactions with the frames (Falborski et al. 2020; Inamasu et al. 2021). Figure 3.1 also illustrates the mechanism through which these connections resist applied loads. The applied axial force and moment are resisted by the development of a bearing stress block on the compression side of the connection, complemented by tension in the anchor rods. Shear is resisted either by the anchor rods, a shear lug (not shown), or friction. Based on these mechanisms, the

American Institute of Steel Construction's (AISC) *Design Guide 1* (Fisher and Kloiber, 2006), hereafter abbreviated as DG1, provides strength characterization methods, and design guidance for these connections.

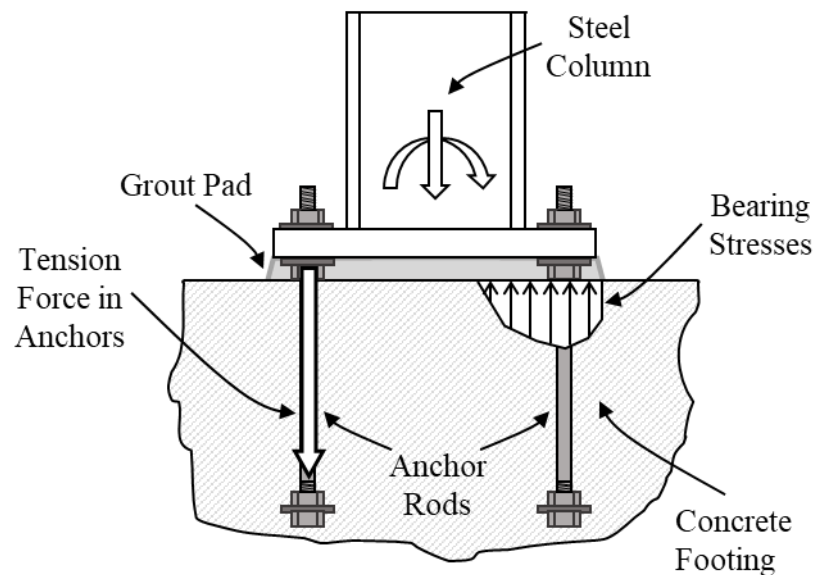


Figure 3.1 – Schematic illustration of an exposed column base plate connection subjected to axial compression and moment

In many situations (especially in commercial or residential buildings), a slab-on-grade is often cast on top of the base plate to provide a flat surface – see Figure 3.2. To achieve this, the column is connected to the footing as in a conventional ECBP connection, but through a diamond shaped “blockout” as shown in Figure 3.2. This blockout allows for the installation of the remainder of the slab-on-grade prior to the installation of any structural steel (minimizing the overlap of concrete and steel work on the job site). After the column is installed, the blockout is filled with unreinforced concrete or grout creating a cold joint between the blockout concrete and the remainder of the slab. The depth of the blockout is usually in the range of 200 mm – 400 mm. The diamond shape of the blockout (i.e., orientation at 45 degrees to the frame gridlines) encourages

formation of shrinkage cracks in preferred directions aligning with construction control joints (i.e., along and perpendicular to the gridlines) as shown in Figure 3.2.

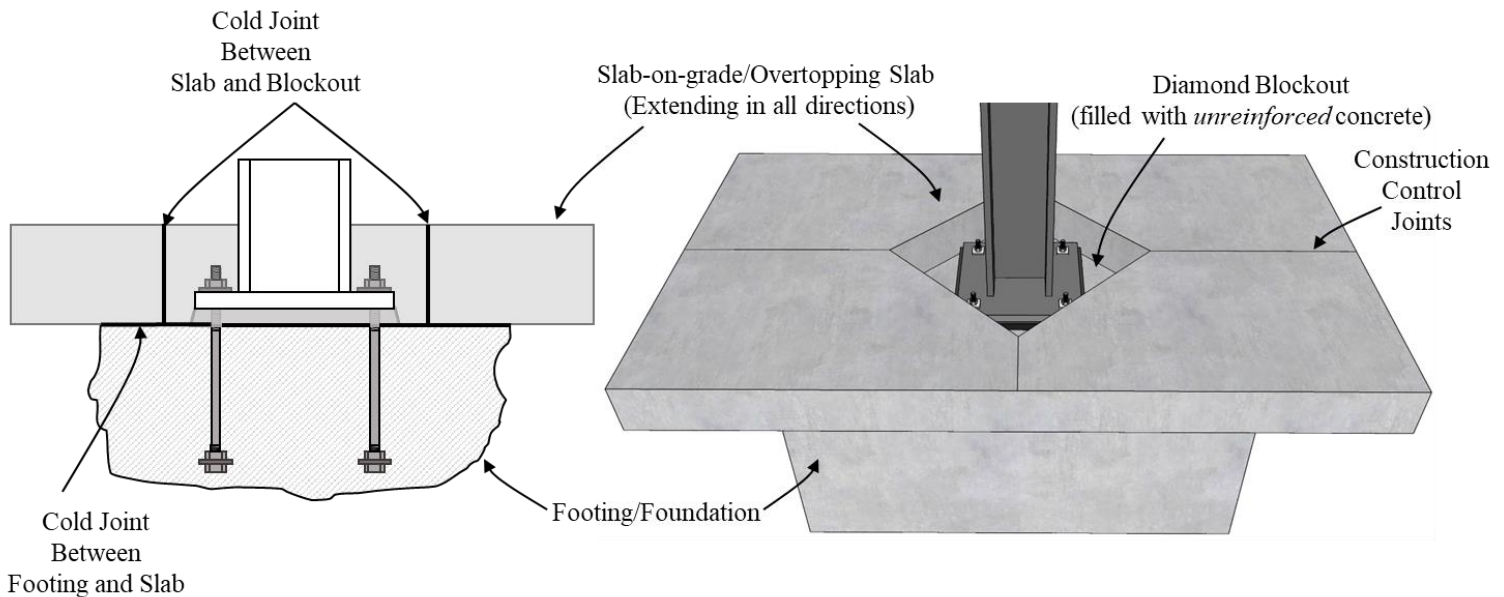


Figure 3.2 – Blockout column base connection

The blockout and the surrounding slab results in an embedded base connection, which provides supplemental flexural strength and stiffness to the mechanisms illustrated in Figure 3.1. This supplemental resistance is usually disregarded in the design of the ECBP connection itself, as well as in the simulation of the frame – both in the context of its design as well as seismic performance assessment. Previous experiments by Richards et al. (2018), Hanks and Richards (2019) on similar connections, as well as Grilli et al. (2017) on more deeply embedded connections indicate that the embedment provides significant additional strength (as much as 50% compared to ECBPs without the blockout) as well as stiffness, which cannot be disregarded without introducing major conservatism into design and seismic performance assessment. The latter (i.e., performance assessment) is particularly relevant because: (1) a large number of ECBP connections with

blockout are often present, both in the seismic lateral load resisting system as well as the gravity system, (2) these are often simulated ECBP connections without the blockout, greatly underestimating their contribution to the overall lateral resistance of the frame, and 3) the collapse capacity of the overall system has been shown (Flores et al. 2014) to be sensitive to the base condition.

Despite their importance, blockout as well as embedded connections (especially those consistent with United States construction practice) have attracted research attention only recently, such that the knowledge regarding their response is fairly immature. The only experimental studies featuring blockout connections are Richards et al. (2018); Hanks and Richards (2019), and the only study with embedded connections is by Grilli et al. (2017). While these studies provide valuable experimental data and an understanding of fundamental behavior and seismic response, none of the experimental specimens (on blockout connections) tested so far include axial compression, which is expected to have a major influence on the response of the connection. Motivated by this, the current study presents results from three large-scale experiments on blockout connections representative of construction practice in the United States. In addition to interrogating the effect of axial force on lateral or flexural cyclic response, the experiments also feature larger (than previously tested) column sizes and base plates, and also a larger slab on grade outside the blockout, providing realistic boundary conditions with respect to uplift of the blockout.

The next section of the chapter summarizes observations from previous studies conducted in the United States as well as a previous study from Japan. This is followed by a discussion of the experiments conducted as part of this study. Results from the experiments (both current and

previous) are then used to propose a model for strength characterization that provides good accuracy across all test programs, and to evaluate models for estimation of rotational stiffness. The study concludes by providing recommendations for design and representation of these connections, and outlining limitations.

3.2 BACKGROUND AND PREVIOUS WORK

Experiments from two prior test programs are considered in this study to supplement test data from this study, and to inform model development and validation. Both these test programs feature details that may be considered similar to construction practice in the United States. These programs were conducted at Brigham Young University (termed BYU tests) and Kyoto University, termed the KU tests. The BYU series (Richards et al., 2018; Hanks and Richards, 2019) consists of 10 experiments (applying load along the strong axis) on specimens with shallowly embedded details, intended to represent a slab-on-grade overtopping an exposed base plate type connection. A strength model was developed to quantify the flexural strength of blockout connections. Figure 3.3 illustrates the key concept of the strength model (details and associated equations are available in Richards et al. 2018). As per this approach, the effect of the blockout and surrounding slab may be represented by assuming that the blockout effectively blockout spreads the compression out over a distance $d_{blockout}$ from the face of the column. The failures in the specimens from BYU study all showed separation of the entire slab from the footing below, rather than separation of the blockout from the slab or breakout of concrete above the base plate.

In the KU test series, Cui et al. (2009) tested 7 specimens of column base connections embedded in concrete, referred to hereafter as the KU study (Kyoto University). Of these, two specimens are

physically similar to breakout connections used in the United States (i.e., the overtopping slab only reinforced by top mesh bars, with no reinforcement around the base plate), and are consequently considered in this study. The specimens featured square-tube columns with a welded base plate featuring twelve anchor rods (distributed on multiple rows), with different embedments (100 and 200 mm). The specimens showed a notable increase in strength (10 to 95%) as well as elastic stiffness (10 to 47%) as compared to a similar base connection without the embedment. The study identified the failure mode of most specimens (including the ones of interest shown in Table 3.1) as an upward punching shear failure of the overtopping slab with a 45-degree cone formation. An analytical model was proposed to evaluate the moment capacity of the connection by adding the

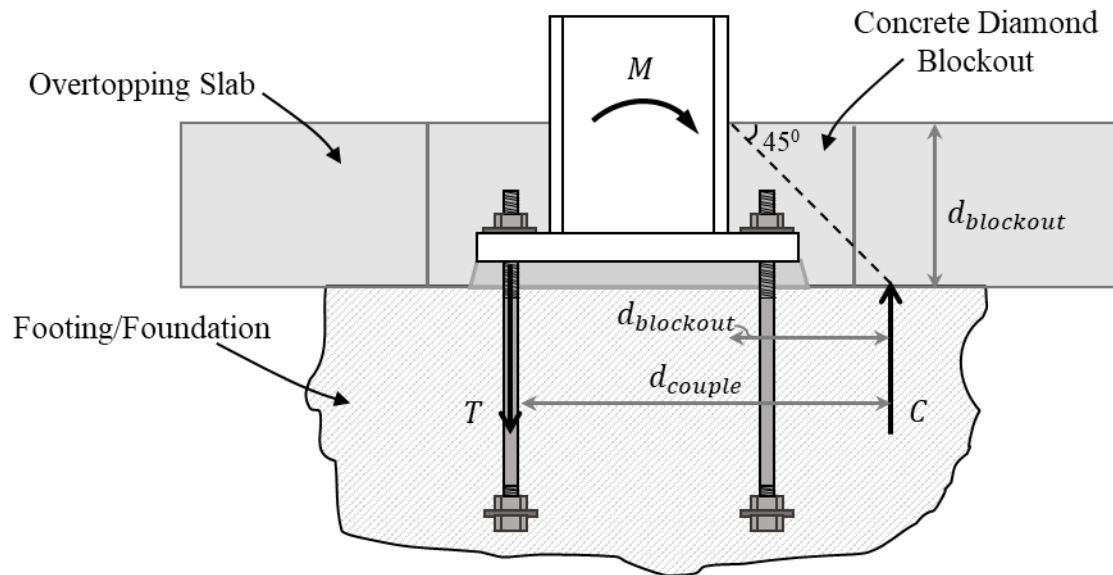


Figure 3.3 – Schematic illustration of the breakout column base connection strength model developed by Richards et al. (2018)

strength of multiple components (base plate and column bearing, concrete slab, and anchor rods), assuming plastic response of the connection.

These two test programs provide an understanding of the load transfer and failure modes of blockout connections, indicating that the embedment generated by the blockout supplements by the resistance by restraining the motion of the column in the horizontal direction, and the embedded base plate in the vertical direction. These mechanisms are qualitatively similar to those observed for embedded column base connections, by Grilli and Kanvinde (2017). The next section describes the experiments conducted as part of the current study.

3.3 EXPERIMENTAL PROGRAM

This section outlines the experimental test setup, matrix, applied loading protocol, and instrumentation for the recent experiments conducted in this study. Figures 3.4 and 3.5 illustrate aspects of the test setup and specimen detailing, respectively; whereas Table 3.1 summarizes the test matrix, along with key results that are discussed later.

Test Setup and Instrumentation

Figure 3.4 shows the test setup, including the specimen, reaction frame for lateral loads, and the loading cross-beam to introduce compressive axial loads. Specific aspects of the test setup are now summarized:

- All specimens were cantilever columns attached to a footing through a blockout in the slab. Lateral deformations were applied to the columns with a servo-hydraulic actuator attached at the top. This location (3.4 m above the base plate) was assumed to represent the inflection point in a first story column. All columns were of ASTM A992 steel with Grade 50 ($F_y = 345 \text{ MPa}$) and were designed to remain elastic to induce failure in the base connection.
- The footing dimensions (common for all tests) are indicated on Figure 3.5. All footings used concrete with nominal compressive strength $f'_c = 27.6 \text{ MPa}$, and were provided with

minimal longitudinal and transverse reinforcement. The reinforcement featured an identical top and bottom mesh of #5 hooked bars (#16 metric size) placed longitudinally at 305 mm (12 in.) on center and transversely at 178 mm (7 in.) on center, with a 76 mm (3 in.) bottom cover. The footings were fastened to the strong floor using pretensioned rods/tie downs as shown in Figure 3.5.

- An overtopping slab of length of 2.43 m (96 in.), a width of 1.82 m (72 in.) and depth 305 mm (12 in.) with a nominal compressive strength $f'_c = 27.6 \text{ MPa}$ was cast on top of each footing, consistent with standard practice. The slab reinforcement represented typical temperature and shrinkage reinforcement (top mesh only). A diamond-shaped blockout formwork was placed to allow for column placement. After column placement, the space created by the blockout was filled with plain concrete ($f'_c = 27.6 \text{ MPa}$), resulting in cold joints with the underlying footing, as well as the surrounding slab.
- The loading-beam shown in Figure 3.4 introduced a constant compressive axial load through an assembly of tension rods and hydraulic jacks in Tests #2, and #3. The lower end of the tension rods was connected to a freely rotating clevis, such that the axial forces were follower forces and did not introduce $(P - \Delta)$ moment into the connection as the column rotated.
- The columns were welded to the base plates with Partial Joint Penetration (PJP) welds and reinforcing fillet welds. The plate and welds were sized to remain elastic, forcing yielding into the anchors.

All specimens featured 4 anchor rods with the same diameter (1 in./25.4 mm) and material grade (ASTM F1554, Gr. 55 – 380 MPa). At the bottom end of the rods, a square plate washer and nut assembly provided anchorage, while at the top, a nut and plate washer were used along with oversized base plate holes as specified by *AISC Design Guide One* (2006). A shear lug with a

thickness of 25.4 mm was fillet welded to the bottom of the base plate protruding 82.5 mm (3.25 in.) from the bottom surface of the base plate. A 50 mm (2 in.) layer of non-shrink grout with nominal compressive strength $f_{grout} = 55 \text{ MPa}$ was provided between the base plate and the top surface of the concrete footing after the setting and leveling of the base plate on shim stacks. The fabrication and erection procedure for the detail is similar to that used in current field practice. Major instrumentation included measurements of: (1) lateral force and displacement at the top of the column (i.e., at the actuator location); (2) axial force in the column; (3) vertical displacements of the diamond blockout concrete; (4) strain gage measurements from the anchor rods and the base

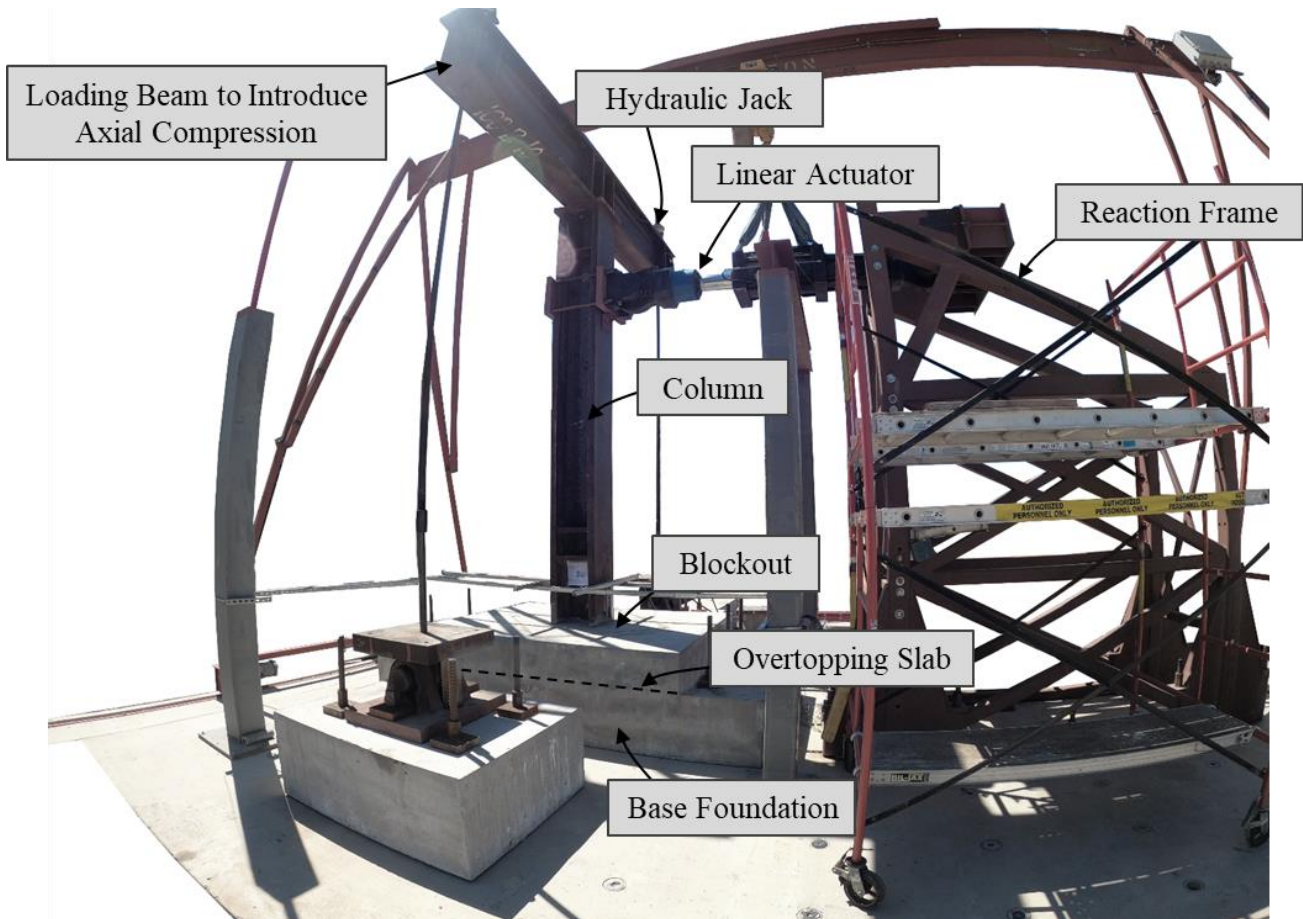


Figure 3.4 – Wide angle view of test setup

plate surface to monitor local strains. Additional transducers were installed to detect unanticipated response modes such as out of plane and torsional response of the column.

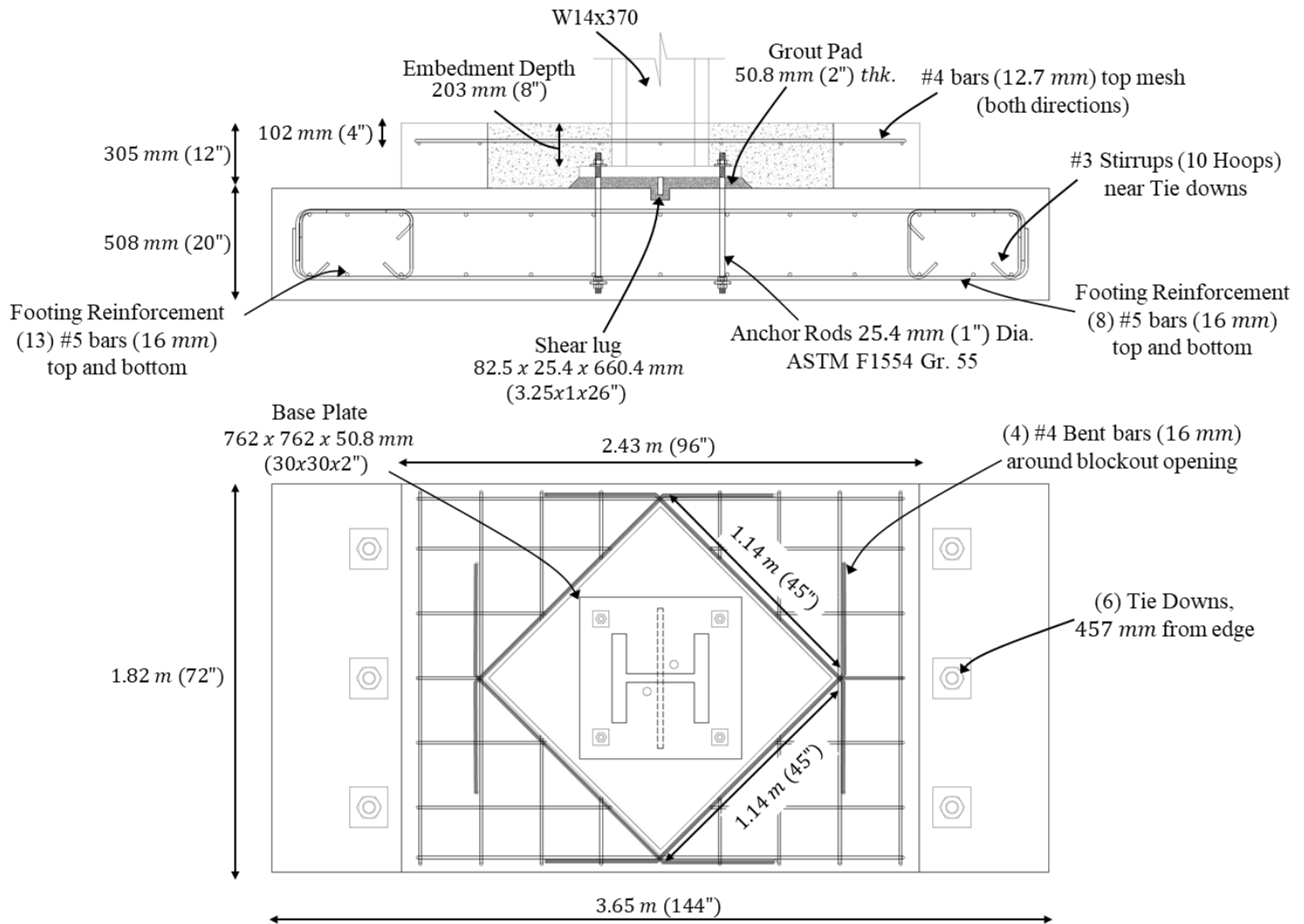


Figure 3.5 – Schematic illustration of experimental specimens detailing

Ancillary Testing and Material Properties

Ancillary tests were conducted to characterize the mechanical properties of the materials used in the tested specimens; these tests included: (1) tension tests of the anchor rods, (2) compression tests on standard concrete cylinders, and (3) compression tests of grout cylinders. Concrete

samples were taken during the casting of the footing, overtopping slab, as well as the blockout and grout specimens were cast during the installation of the column. Table 3.2 summarizes measured material properties corresponding to each large-scale test.

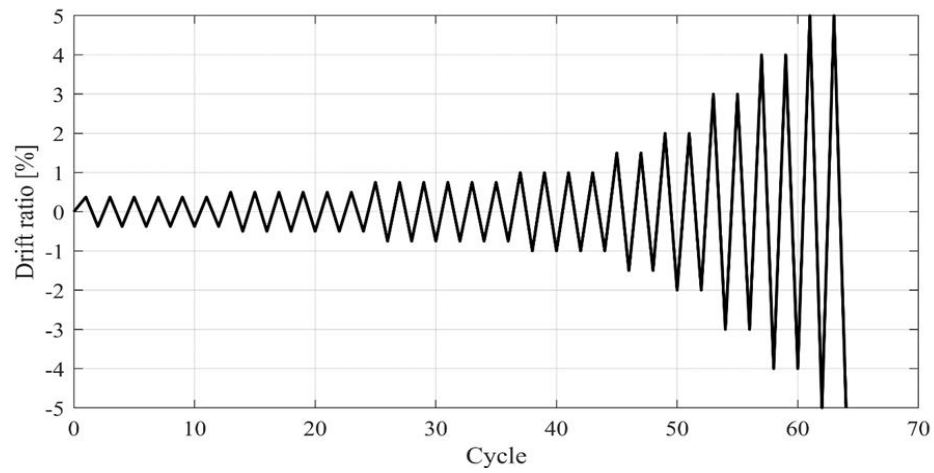


Figure 3.6 – Loading protocol

Table 3.1 – Tests Matrix and Results from UCD Tests

Test ^{a,b}	Axial Load P [kN]	Embedment Depth d_{embed} [mm]	Anchor Rod Diameter ^{c,d} d^{rod} [mm]	ASTM ^e F1554 Anchor Grade	M_{DG1} ^f [kN.m]	M_{max}^{test} ^g [kN.m]	M_y^{test} [kN.m]	$\frac{M_{max}^{test}}{M_{DG1}}$	$\frac{M_y^{test}}{M_{DG1}}$	$\frac{M_y^{test}}{M_{max}^{test}}$	$Drift_{max}$ [%]
1	0	203 (8")	25.4 (1")	55 (380 MPa)	275	571 (+)	463 (+)	2.07	1.68	0.81	5 (+)
						553 (-)	443 (-)	2.01	1.61	0.80	5 (-)
2	445 (100 kip)	203 (8")	25.4 (1")	55 (380 MPa)	436	857 (+)	624 (+)	1.96	1.43	0.73	5.7 (+)
						861 (-)	586 (-)	1.97	1.34	0.68	5.1 (-)
3	667 (150 kip)	203 (8")	25.4 (1")	55 (380 MPa)	515	898 (+)	786 (+)	1.74	1.52	0.88	6.1 (+)
						780 (-)	547 (-)	1.51	1.06	0.70	5.5 (-)
							Mean	1.88	1.45	0.77	5.4
							CoV	0.11	0.15	0.09	0.08

^aTests featured $W14 \times 370$ (customary units) cantilever columns - ASTM A992 Grade 345 MPa.

^bBase plate dimensions: $N \times B \times t_p = 762 \times 762 \times 51$ mm; Edge distance between rod centerline and edge of plate = 101.5 mm. with 2 rods on each side; Oversized hole diameter in plate = 47.5 mm.

^cUnthreaded diameter (rod shank) with a 4" threaded portion on top and bottom.

^dSquare plate washers at top and bottom dimensions: $76 \times 76 \times 9.5$ mm and $76 \times 76 \times 12$ mm, respectively.

^eValues of anchor rod yield strength F_y^{rod} are nominal. Refer to Table 3.2 for measured material properties.

^fMoment calculated in accordance with current procedures outlined in AISC's Design Guide One - Fisher and Kloiber (2006), using measured material properties.

^gMaximum moment at the level of base plate level measured for specimens in each direction of loading (positive and negative), where the positive sign denotes the first deformation cycle direction

Large Scale Test Matrix

Referring to Table 3.1, the selected specimen characteristics were selected to be representative of current design practice with axial load as the primary variable. Specifically:

- The compressive axial loads were varied to examine the effect on the moment capacity. The level of applied axial load was chosen such that yielding of the base plate on the compression side of the connection was avoided.
- The anchor sizes were chosen to ensure yielding in the anchors, while other components of exposed base connection remained elastic. The embedment length of anchor rods was sufficient to achieve full tensile capacity prior to pullout/breakout concrete failure following *AISC Design Guide 1* and ACI 318-19 standards (ACI 2019).

Axial load was introduced first and held constant while the lateral displacement-controlled loading protocol was applied. Figure 3.6 illustrates the lateral loading protocol, expressed in terms of the column drift ratio measured with respect to the top of the base plate – which is usually considered to be the datum for structural analysis and design (i.e., the blockout is not considered). The ATC-SAC (Krawinkler et al. 2000) history was selected to represent deformation histories consistent with seismic demands in moment frame buildings.

3.4 EXPERIMENTAL RESULTS

Response plots for column base moment versus rotation (determined from the total deformation after subtracting the elastic column deformations) are presented in Figures 3.7a-d for the three tested specimens, whereas Figures 3.8a-d show photographs of damage progression and failure for one of the tests (Test #2); the damage progression is qualitatively similar for all other experiments. The photographs illustrate response and failure modes of the tested specimens and correspond to the loading instants identified by the numbers 1 to 3 in Figures 3.7a-c. The typical damage progression included the following:

1. On the compression side of the connection, small cracks began to form on the concrete surface in front of the column flange indicative of concrete crushing – Figure 3.8a, corresponding to Point “1” on Figures 3.7a-c.
2. On the tension side of the connection, diagonal cracks are seen emanating from the corner of the column flange extending into the blockout and beyond into the overtopping slab around it – Figure 3.8b, corresponding to Point “2” on Figures 3.7a-c. This (as determined subsequently) is indicative of the breakout cone of the concrete forming underneath the surface as the plate pushes the concrete upwards. The capacity of the connection is reached around this time.
3. Cracks perpendicular to the direction of loading (which appeared earlier) start to grow at the corners of the blockout, Figure 3.8c. These cracks indicate splitting of the outside slab (at its weakest net section) due to wedging of the blockout as it tries to rotate further. After this point, the blockout concrete begins to rotate somewhat freely within the diamond-shaped hole, shimmying up as the deformations increase – also shown on Figure 3.8c. This continues until the strains in the anchors accumulate, eventually causing fracture of one of the anchors, which occurs at around 5-6% drift, corresponding to Point “3” on Figures 3.7a-c.

4. Figure 3.8d shows a post-test photograph of the concrete and blockout after removal of the column; the location of the column, and the diamond blockout are indicated. This shows the blowout cone, which extends through into the surrounding overtopping slab.

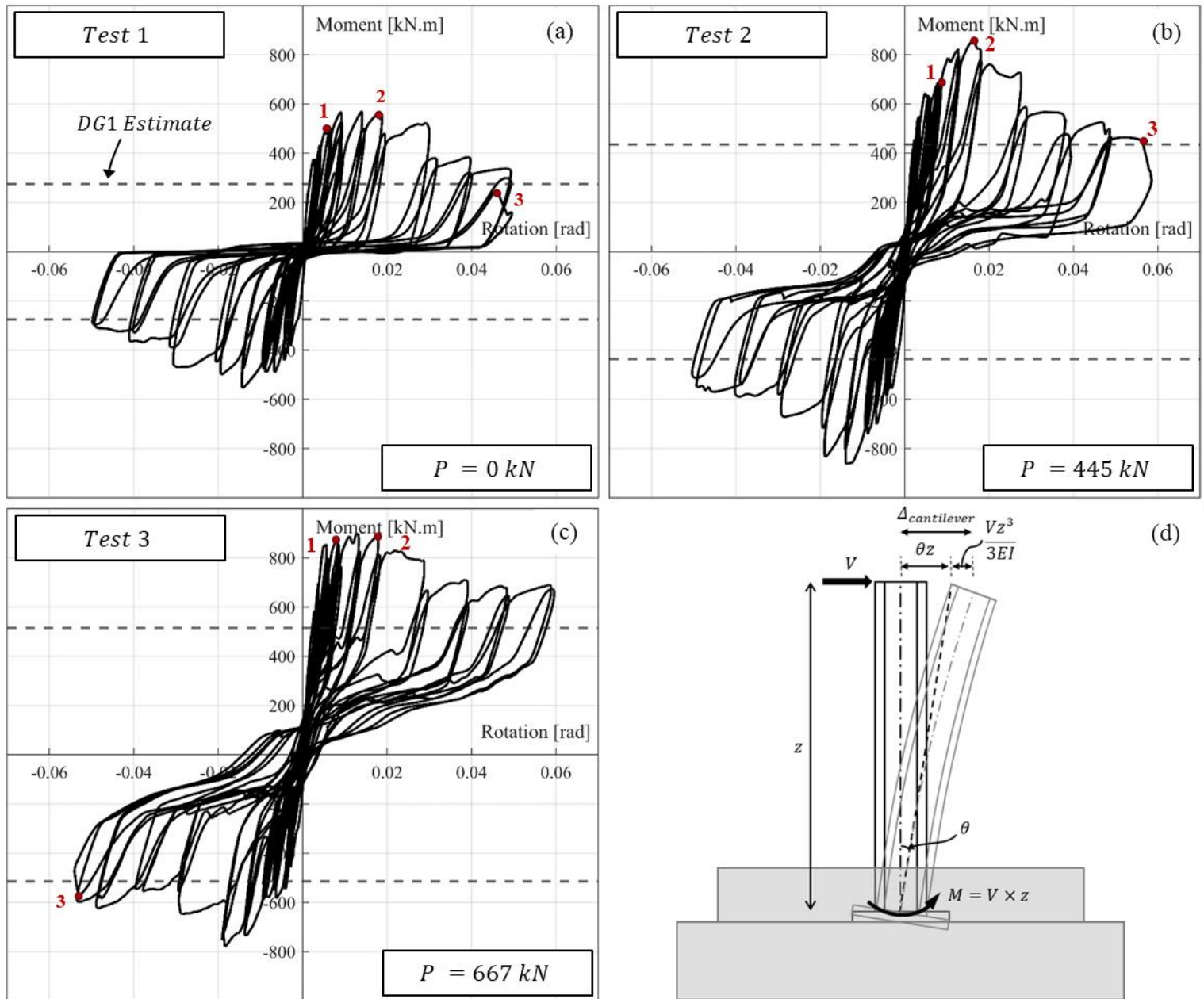


Figure 3.7 – Moment rotation plots for all experiments and schematic illustration of plotted quantities

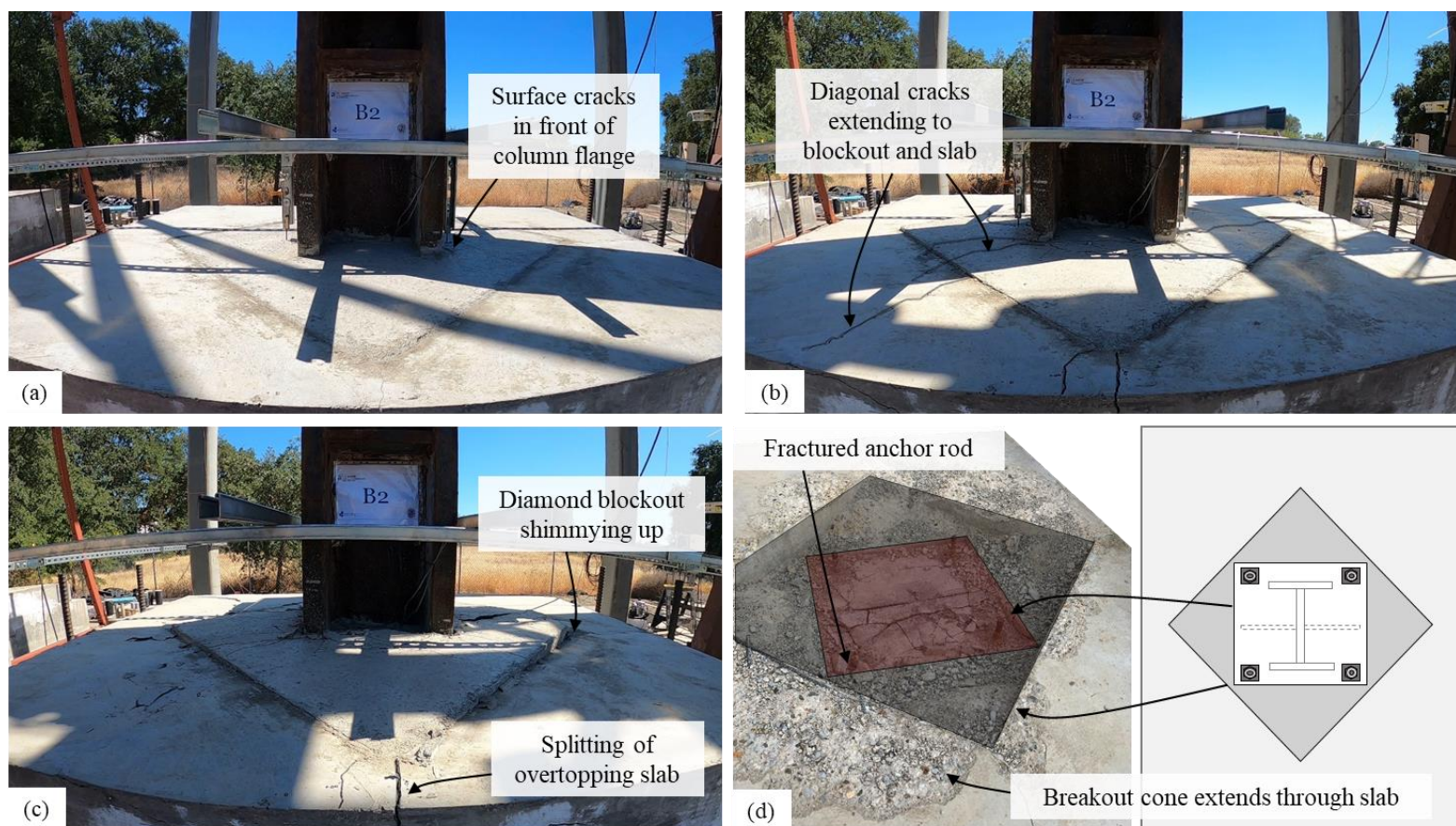


Figure 3.8 – Typical damage progression for one of the tested specimens (Test #2)

Table 3.2 – Summary of measured material strengths from ancillary tests

Test #	Anchor Rod Yield Strength ^a F_y^{rod} [MPa]	Anchor Rod Ultimate Strength F_u^{rod} [MPa]	(Base Foundation) Concrete Compressive Strength ^b f'_c [MPa]	(Overtopping Slab) Concrete Compressive Strength f'_c [MPa]	(Blockout) Concrete Compressive Strength f'_c [MPa]	Grout Compressive Strength f_{grout} [MPa]
1	400	552	30.5	28.1	28.0	58.5
2			31.0	28.6	28.3	60.1
3			30.7	28.3	28.1	58.5

^a ASTM F1554 Rod Grade 55 (ASTM 2020).

^b Compressive strength for concrete and grout cylinders is measured on the day of full-scale test.

Table 3.1 summarizes important quantitative data. This includes the maximum base moment observed during testing M_{max}^{test} with two values provided, one for each loading direction (M_{max+}^{test} , and M_{max-}^{test}), where the positive sign denotes the direction of the first deformation cycle. These moments represent the column moments calculated at the elevation of the top surface of base plate, which is usually considered as the datum in structural analysis and design. In addition to the ultimate moments M_{max+}^{test} , and M_{max-}^{test} , the yield moment strengths, M_{y+}^{test} , and M_{y-}^{test} are of interest as well. However, unlike the ultimate moments, these cannot be determined objectively given the nonlinearity of the load deformation curve even at relatively low moments (see Figures 3.7a-c). As a result, a procedure outlined by Grilli et al. (2017) is used to estimate these in a consistent way – this involves conducting a least squares fit of a bilinear moment-rotation relationship to the backbone of the experimental moment-rotation curve. The ratio of the yield moment to the ultimate moment $M_y^{test}/M_{max}^{test}$ is also tabulated in Table 3.1 for each of the experiments. The average value of $M_y^{test}/M_{max}^{test}$ for all experiments is 0.77 with a Coefficient of Variation (CoV) 0.09, which suggests consistency and may be considered as a fraction of ultimate strength for design purposes. The table also includes the ratio between the maximum base moment, M_{max}^{test} and yield base moment, M_y^{test} observed during testing with respect to the design moment M_{DG1} . Referring to Table 3.1 and Figures 3.7a-c, the following observations may be made:

- A majority (2 out of 3) of the experiments are stronger in the positive direction, such that the average of $M_{max+}^{test}/M_{max-}^{test}$ is 1.05 with a Coefficient of Variation (CoV) 0.07. This suggests that damage caused by loading in one direction affects the strength in the reverse direction.
- A comparison among Tests #1, 2 and 3 provides a direct assessment of the effect of axial load, indicating that the moment capacity of the connection steadily increases with respect to axial

load. This is not unexpected, because the axial compression introduces a pre-stress into the connection, delaying the uplift of the base plate.

- All specimens exhibited excellent deformation capacity until 5-6% drift without considerable strength degradation.

3.5 MODELS FOR STRENGTH CHARACTERIZATION

Richards et al. (2018) and Hanks and Richards (2019) proposed a method to characterize the strength of blockout connections. The details of the method (illustrated previously in Figure 3.3) may be found in Hanks and Richards (2019); only the main concepts are summarized here. The method incorporates the effect of the blockout by assuming that it effectively extends the plate on the compression side of the connection, and the moment at the base of the column is resisted by a force couple consisting of a resultant tensile force T in the anchor rods and a compression resultant C at the base of the blockout, located at the distance d_{couple} as indicated in Figure 3.3. For each of experiments considered in this study (i.e., from the Richards et al. 2018, Hanks and Richards 2019, and Cui et al. 2009 test programs as well as the tests described in this study – see Table 3.3), this approach (termed Method 1) is used to estimate the moment strength. The strength comparisons made in this section utilize the ultimate strength from the experiments (i.e., M_{max}^{test}) because it can be estimated objectively. Corresponding model-based estimates (i.e., $M_{max}^{Method\ 1}$) utilize the measured (rather than specified) ultimate strength of the anchor rod (F_u^{rod}), rather than the yield strength (F_y^{rod}) for a consistent comparison with the experiment. Note that the anchor rod is the only element in the connection that yields, such that the strength of the base plate or column material is not relevant. Figures 3.9a-f plot results for all the experiments (BYU, KU, and UCD series) from various strength characterization methods against two test variables, i.e., the

column embedment (normalized by the depth of the column, i.e., d_{embed}/d_{col}), and the axial force (normalized by the crushing strength of the footing under the base plate, i.e., P/P_{crush}). Specifically, Figures 3.9a-b plot the test-predicted ratios M_{max}^{test}/M_{DG1} for the DG1 approach, which entirely disregards the effect of the overtopping slab or blockout. Figures 3.9c-d are similar, except that the test-predicted ratios $M_{max}^{test}/M_{max}^{Method\ 1}$ are plotted for Method 1 outlined above. Finally Figures 3.9e-f plot results for a new strength characterization approach proposed herein (and presented later) – this is termed Method 2. Referring to Figures 3.9a-d, and the corresponding entries in Table 3.3, it is noted that:

- The average test-predicted ratio for the DG1 method, i.e., M_{max}^{test}/M_{DG-1} is 1.67 with a CoV 0.32. This is not unexpected, because the DG1 entirely disregards the contribution of the overtopping slab. Moreover, this suggests that using the DG1 approach to assess the strength of blockout connections is highly conservative. This is further confirmed through an examination of Figure 3.9a, which shows a positive trend with respect to the embedment ratio d_{embed}/d_{col} (implying greater conservatism as the embedment increases). No such trend is observed with respect to the axial load ratio P/P_{crush} .
- The average test-predicted ratio for Method 1, i.e., $M_{max}^{test}/M_{max}^{Method\ 1}$ is 1.38 with a CoV 0.50. This suggests, that on average, the conservatism is reduced by accounting for the effect of embedment. Nonetheless, the method is still conservative and has a significant variability (CoV), suggesting that it does not accurately represent the underlying physics when examined across all the tests. More specifically, Figure 3.9c shows that while the approach works well for $P/P_{crush} = 0$ (with an average $M_{max}^{test}/M_{max}^{Method\ 1} = 0.93$), the accuracy of the method decreases for applied axial compression. This is not surprising either, because Method 1 is

based on experiments (Richards et al. 2018; Hanks and Richards 2019) that do not include an axial force.

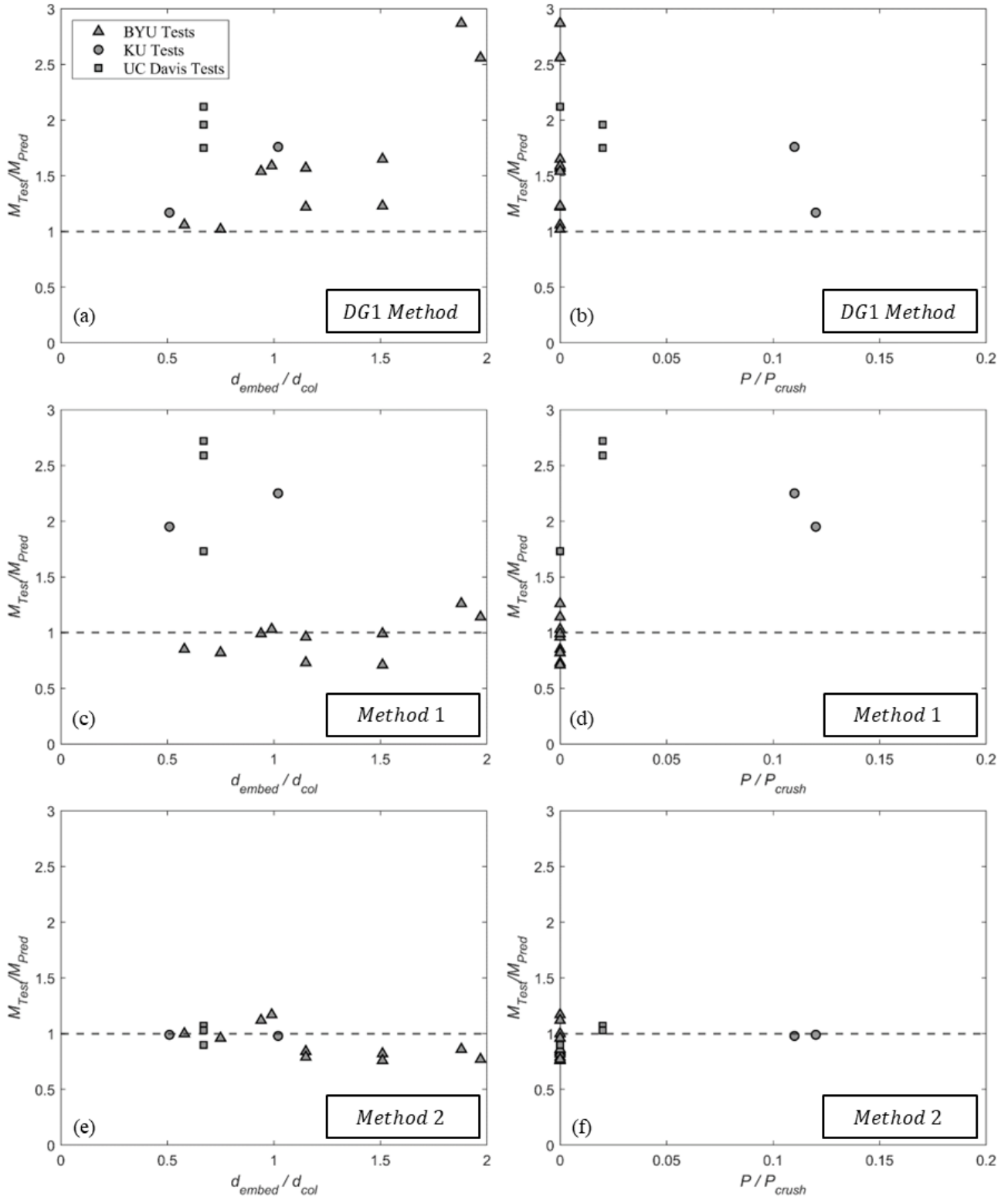


Figure 3.9 – Test-predicted ratios for all experiments from various strength characterization methods plotted against d_{embed}/d_{col} and P/P_{crush}

Table 3.3 – Test Matrix from UCD, BYU and KU Studies and Results

Test Prog.	Test # ^a	Column Size	$d_{embed}^{c,d}$ [mm]	P [kN]	Base Plate Size $t_p \times N \times B$ [mm]	d^{rod} [mm]	F_y^{rod} [MPa]	F_u^{rod} [MPa]	$M_{max}^{test\ e}$ [kN.m]	$\frac{M_{max}^{test}}{M_{DG1}}$	$\frac{M_{max}^{test}}{M_{max}^{Method\ 1}}$	$\frac{M_{max}^{test}}{M_{max}^{Method\ 2}}$	$\frac{\beta^{test}}{\beta_{UC-Exposed}^{Method}}$	$\frac{\beta^{test}}{\beta_{BYU}^{Method}}$
UCD	1	W14x370	203	0	2 x 30 x 30" (51 x 762 x 762)	25.4	400 MPa (58.1 ksi)	552 MPa (80 ksi)	588	2.12	1.73	0.90	2.05	1.67
UCD	2			445		25.4			882	1.96	2.59	1.07	1.50	1.97
UCD	3			667		25.4			925	1.75	2.72	1.03	1.32	1.98
									Mean	1.94	2.35	1.00	1.62	1.87
									COV	0.09	0.23	0.09	0.23	0.09
BYU	D2 ^b	W14x53	121	0	2.25 x 22 x 16" (57 x 559 x 406)	25.4	355 MPa (51.5 ksi)	621 MPa (90 ksi)	487	1.06	0.85	1.00	0.75	0.98
BYU	D3 ^b		324			25.4			559	1.22	0.73	0.84	0.76	1.24
BYU	D4 ^b		343		1.50 x 22 x 16" (38 x 559 x 406)	25.4			369	1.57	0.96	0.79	1.34	0.96
BYU	F2 ^b	W10x77	102		3 x 20 x 16" (76 x 508 x 406)	28.6	341 MPa (49.5 ksi)	527 MPa (76.5 ksi)	447	1.02	0.82	0.96	0.84	1.10
BYU	F3 ^b		305			28.6			539	1.23	0.71	0.82	0.88	1.21
BYU	F4 ^b		330		2 x 20 x 16" (51 x 508 x 406)	28.6			372	1.65	0.99	0.76	1.85	1.07
BYU	A1 ^b	W8x35			1 x 13 x 13" (25 x 330 x 330)	19	314 MPa (45.5 ksi)	560 MPa (81 ksi)	109	1.59	1.03	1.17	0.74	0.78
BYU	A2 ^b	W8x48				19			105	1.54	0.99	1.12	0.84	0.82
BYU	B1	W8x35				19			175	2.56	1.14	0.77	1.42	0.80
BYU	B2	W8x48				19			196	2.87	1.26	0.86	1.81	0.96
									Mean	1.63	0.95	0.91	1.12	0.99
									COV	0.38	0.19	0.16	0.39	0.16
KU	SL-100	HSS	76	511	1 x 11.8 x 11.8" (25 x 300 x 300)	12.7	303 MPa (44 ksi)	552 MPa (63.7 ksi)	135	1.17	1.95	0.99	-	-
KU	SL-200	8x8x3/8	178			12.7			206	1.76	2.25	0.98	-	-
									Mean	1.46	2.10	0.98	-	-
									COV	0.28	0.10	0.00	-	-
									Mean (All)	1.67	1.38	0.94	1.24	1.19
									COV (All)	0.32	0.50	0.14	0.38	0.35

^a Test names refer to the reported labeling system in each respective publication (Richards et al. 2018; Hanks and Richards 2019; Cui et al. 2009).^b Tests from BYU program for which separation of slab occurred (refer to Figure 3.10f).^c Embedded depth d_{embed} is calculated based on the schematic in Figure 3.10b.

^d Reported values for breakout concrete compressive strength f'_c were used as follows: 28 MPa (4 ksi) for UCD and KU, 31 MPa (4.5 ksi) for BYU (D and F tests), and 17.2 MPa (2.5 ksi) for BYU (A and B tests).

^e M_{max}^{test} is the maximum moment value of both directions of loading (positive and negative) calculated at the top of foundation level.

In summary, neither the DG1 approach, nor Method 1 provide satisfactory characterization of connection strength, motivating an approach that is able to characterize the strength of breakout connections with more generality, across a large range of configurations, and considering the effect of axial force as well. This is the topic of the next subsection.

Proposed Approach for Strength Characterization

As discussed in the preceding sections, introduction of the breakout concrete provides significant additional resistance with respect to the DG1 method (see Table 3.3). This additional resistance may be attributed to two mechanisms as determined by Grilli and Kanvinde (2017) in the context of Embedded Base Connections. These mechanisms are illustrated in Figures 3.10a-b: (1) the development of horizontal bearing stresses against the column flanges, and (2) the development of downward vertical stresses that resist uplift of the base plate. The breakout connections are similar in terms of the overall mechanics as compared to the connections studied by Grilli and Kanvinde (2017), with three differences:

1. The breakout connections include a fully designed exposed base plate connection under the breakout with anchor rods; this has two implications. First, the distribution of moments between the horizontal and vertical bearing mechanisms is affected by the fixity of the exposed base plate under the breakout. Second, the failure modes also include those associated with the exposed base plate connection, e.g., anchor rod yielding and failure.
2. The embedment of the breakout connections is usually lower (in the range of 200-400mm) as compared to the embedded connections.
3. The breakout connections include a cold joint (see Figures 3.2a-b) between the breakout concrete and the surrounding slab.

Based on these observations, the key assumption of the method is that the total applied base moment is resisted through a combination of horizontal and vertical bearing such that their contributions to the overall strength are additive, as follows:

$$M_{base} = M_{HB} + M_{VB} \quad (3.1)$$

This assumption is based on the visually observed failure modes in the various experiments, and implies the development of a plastic mechanism in which the following response modes are mobilized and considered to be acting “in parallel” such that their contributions at the limit state can be incorporated as shown in Figures 3.10c-d: (1) yielding of the anchor rods on the tension side accompanied by uplift of the base connection, (2) development of an upward stress block on the compression side of the base plate, similar to that assumed in DG1, (3) development of a downward stress block on the uplifting side of the plate, in the vertical direction; and (4) development of bearing stress blocks on both sides of the embedded column (top and bottom) in the horizontal direction. Figure 3.10c-d schematically illustrates the idealized internal forces and stresses associated with the transfer of moment and shear for both the vertical and horizontal resistance mechanisms.

Moment Resistance due to Vertical Bearing Stresses

Referring to Figure 3.10c, the bearing stress underneath the base plate (on the compression side of the connection) may be represented as a rectangular block with a value of f_{lower} denoting the lower side of the plate and the corresponding width Y_{lower} . This follows the approach of DG1 for exposed base plate connections. The bearing stress magnitude f_{lower} may be determined as $f_{lower} = \min(f_{grout}, f_{concrete})$, wherein f_{grout} is the crushing strength of the grout, whereas $f_{concrete}$ is determined to account for the confining effect of the footing size as follows:

$$f_{concrete} = 0.85 \times f'_c \times \sqrt{A_2/A_1} \leq 1.7 \times f'_c \quad (3.2)$$

Where f'_c is the compressive strength of concrete, A_1 is the plate bearing area, and A_2 is the effective concrete area (typically the plan area of the footing). In the case of blockout base connections, since both the concrete and the grout are confined, f_{lower} is usually governed by the value of $f_{concrete}$. The width of the bearing stress block Y_{lower} is an unknown; its calculation is discussed later. The tension side of the base plate has two downward forces acting on it (see Figure 3.10c). One is the anchor rod force (summation over all anchors) denoted T , whereas the other is the downward bearing stress on the upper surface of the base plate, termed f_{upper} . Of these, $T = 0.75 \times n_{rod} \times F_u^{rod} \times A_{rod}$ (assuming yielding is mobilized in the rods), where n_{rod} is the number of anchor rods in a line, F_u^{rod} is the ultimate strength of the anchor rod material and A_{rod} is the unthreaded area of the anchor rod. The downward bearing stress block on the upper surface of the base plate f_{upper} may be represented as a resultant downward force F_{upper} , which acts over an effective plate width Y_{upper} as shown in Figure 3.11c. The magnitude of F_{upper} depends on the strength required to fail (or break loose) the concrete above the plate on the tension side of the connection. As discussed previously, this can occur through two mechanisms. The first of these is breakout of the concrete in the blockout and surrounding region. This force may be calculated using the Concrete Capacity Design (CCD) method proposed by Fuch et al. (1995) as shown below:

$$F_{upper} = F_{breakout} = \frac{40}{9} \times \frac{1}{\sqrt{d_{cover}}} \times \sqrt{f'_c} \times A_{35} \quad (3.3)$$

In the above equation, d_{cover} is thickness of the material which must be ruptured for breakout, which is equal to d_{embed} for tension breakout (see Figure 3.10c for reference). The term A_{35} is the projected area of a 35-degree failure cone emanating from the edges of the effective plate width (i.e., the width Y_{upper} of the downward bearing stress block f_{upper}). The effective plate width is

taken as $0.3N$, following the work of Grilli and Kanvinde (2017); where N is the length of the base plate. The projected area A_{35} is shown in Figure 3.10e and is calculated using the equation below:

$$A_{35} = (B + 3 d_{embed}) \times (0.3 N + 1.5 d_{embed}) - (B \times 0.3 N) \quad (3.4)$$

Once these two quantities are determined, two equations may be written corresponding to the vertical force and moment equilibrium as shown below:

$$f_{lower} \times B \times Y_{lower} - P - T = F_{upper} \quad (3.5)$$

$$M_{VB} = F_{upper} \times \left(N - \frac{0.3N}{2}\right) + T \times (N - g) + P \times \frac{N}{2} - f_{lower} \times B \times \frac{Y_{lower}^2}{2} \quad (3.6)$$

Given the applied axial force P , the two equations may be used to solve for the two unknowns Y_{lower} , and M_{VB} . It is important to note that the above Equations 3.5 and 3.6 directly converge to DG1 method for exposed base connections in the case of the blockout/overtopping slab is absent (i.e., $F_{upper} = 0$). The moment M_{VB} calculated in this manner reflects the moment at the bottom end of the embedded column, i.e., at the elevation of the top of the base plate. The moment M_{VB} is calculated in this way for the 3 experiments at UC Davis, the 2 experiments at KU and 2 out of 10 experiments (i.e., Tests B1 and B2) at BYU that failed through the breakout mode.

The second mechanism, through which the concrete overlying the base plate may fail, involves separation of the slab at the cold joint (see Figure 3.10f). Referring to Table 3.3 and prior discussion, this was observed for 8 out of the 10 BYU tests. To estimate the vertical moment strength corresponding to this, DG1 approach is followed by ignoring the effect of bearing stress acting downwards on the upper surface of the base plate (i.e., $F_{upper} = 0$). The equilibrium equations 3.5 and 3.6 above are solved again, with $F_{upper} = 0$.

Moment Resistance due to Horizontal Bearing Stresses

Referring to Figure 3.10d, another portion of the applied moment and shear is resisted through the development of bearing stress blocks on both sides of the embedded column. The model adopted

herein is developed by Mattock and Gaafar (1982) for strength characterization of steel coupling beam embedded in concrete shear walls, and adapted by the AISC Seismic Provisions (AISC 341-16 2016) and the AISC Seismic Design Manual (AISC 2018) for estimation the strength of Embedded Column Base Connections. The model is based on the force couple developed from the top and bottom stress blocks where a parabolic distribution of bearing stresses is assumed for C_{bottom} , and C_{top} is estimated by a uniform stress equal to:

$$f_b^{top} = 4.04 \sqrt{f'_c} \left(\frac{b_w}{b_f} \right)^n \quad (3.7)$$

In the above equation for f_b^{top} (in MPa), the term b_w/b_f accounts for the effect of confinement, wherein b_w (in mm) is the width of the foundation, and b_f (in mm) is width of the flange. The exponent n is calibrated based on experimental data to a value of $n = 0.24$. As per Mattock and Gaafar (1982), the bearing stress distribution at the bottom of the embedded section may be expressed as parabolic function with maximum stress of f'_c at a strain of $\varepsilon_b = 0.002$, such that $f_b^{bottom} = 1000 f'_c [\varepsilon_b - 250 \varepsilon_b^2]$. Referring to Figure 3.10d, the term k_2 defines the location of the resultant compressive force C_{bottom} such that:

$$k_2 = \frac{1 - 0.375 \left[\frac{d_{embed} - c}{c} \right]}{3 - 1.5 \left[\frac{d_{embed} - c}{c} \right]} \quad (3.8)$$

and,

$$C_{bottom} = 0.5 \frac{b_f}{c} \left(\frac{b_w}{b_f} \right)^n f'_c (d_{embed} - c)^2 \left[3 - 1.5 \left[\frac{d_{embed} - c}{c} \right] \right] \quad (3.9)$$

$$C_{top} = f_b^{top} \beta_1 c b_f \quad (3.10)$$

In the above, c (in mm) is the neutral axis depth and β_1 is the factor relating the depth of equivalent rectangular stress block to neutral axis depth, as shown in Figure 3.10d. The moment resistance due to horizontal stresses, M_{HB} may be obtained by simultaneously solving the force and moment

equilibrium equations based on the assumed stress distributions described above and shown in Figure 3.10d:

$$V - C_{top} + C_{bottom} = 0 \quad (3.11)$$

$$V \times z = C_{top} \times \left(d_{embed} - \frac{\beta_1 c}{2} + t_p + t_g \right) - C_{bottom} \times [k_2(d_{embed} - c) + t_p + t_g] \quad (3.12)$$

Such that, t_p (in mm) is the thickness of base plate and t_g (in mm) is the grout layer thickness (if any). Once V and c are calculated from equations (3.11) and (3.12),

$$M_{HB} = V \times z \quad (3.13)$$

The connection strength as per the proposed approach is then calculated such that:

$$M_{max}^{Method\ 2} = M_{VB} + M_{HB} \quad (3.14)$$

It should be mentioned that the above equation implicitly employs a moment-to-shear ratio as a given parameter for defining the problem (i.e., z the height of column inflection point), such that for a given base moment $M_{max}^{Method\ 2}$, the corresponding column/connection shear V is constrained to it. Thus, the reported values of moment capacity depend on this moment-to-shear ratio. The results from the moment capacity calculations for all the tests using the proposed model (denoted $M_{max}^{Method\ 2}$) are summarized in Table 3.3 and illustrated in Figures 3.9e-f; these are similar to Figures 3.9a-d, i.e., they plot the test-predicted ratios against the normalized embedment and axial load. Referring to this figure and Table 3.3, it is observed that:

- The model represents the moment capacity of the blockout connection when compared to tested specimens with good accuracy. When compared to the previously discussed approaches (DG1 and Method 1), the proposed model shows significantly reduced variability and bias with an average $M_{max}^{test}/M_{max}^{Method\ 2}$ of 0.94 and CoV of 0.14, across all the tests, suggesting that the model is able to capture the underlying physics of connection response. For the UCD and KU test series, where slab separation did not occur, average $M_{max}^{test}/M_{max}^{Method\ 2}$ values are 1.0 (CoV

= 0.09), and 0.98 (CoV = 0) respectively, indicating that for realistic situations, the method shows excellent performance.

- For the tests where the slab separation mode of failure occurred (i.e., tests from the BYU program as indicated in Table 3.3), the proposed approach (with adjusted vertical bearing capacity – as explained above) is able to capture the physics and fundamental behavior of the breakout connection with a fair accuracy, as indicated by the average test-predicted ratio of 0.91, with a CoV of 0.16, which is acceptable, although marginally slightly worse than for the other tests. Even if such failure is unlikely in realistic conditions (where a larger slab is present), the agreement between experiments and model further confirm the efficacy of the model in terms of representing the overall physics of connection response.
- Referring to Figure 3.9e, for cases where d_{embed}/d_{col} is greater than 1.5, the method yields slightly unconservative results (with an average $M_{max}^{test}/M_{max}^{Method\ 2}$ of 0.85). These details approach “deeply embedded” connections, similar to those tested by Grilli and Kanvinde (2017). As noted in that study, for these deeper embedments, a full mechanism is often not developed before breakout failure, such that the component strengths may not be considered additive.

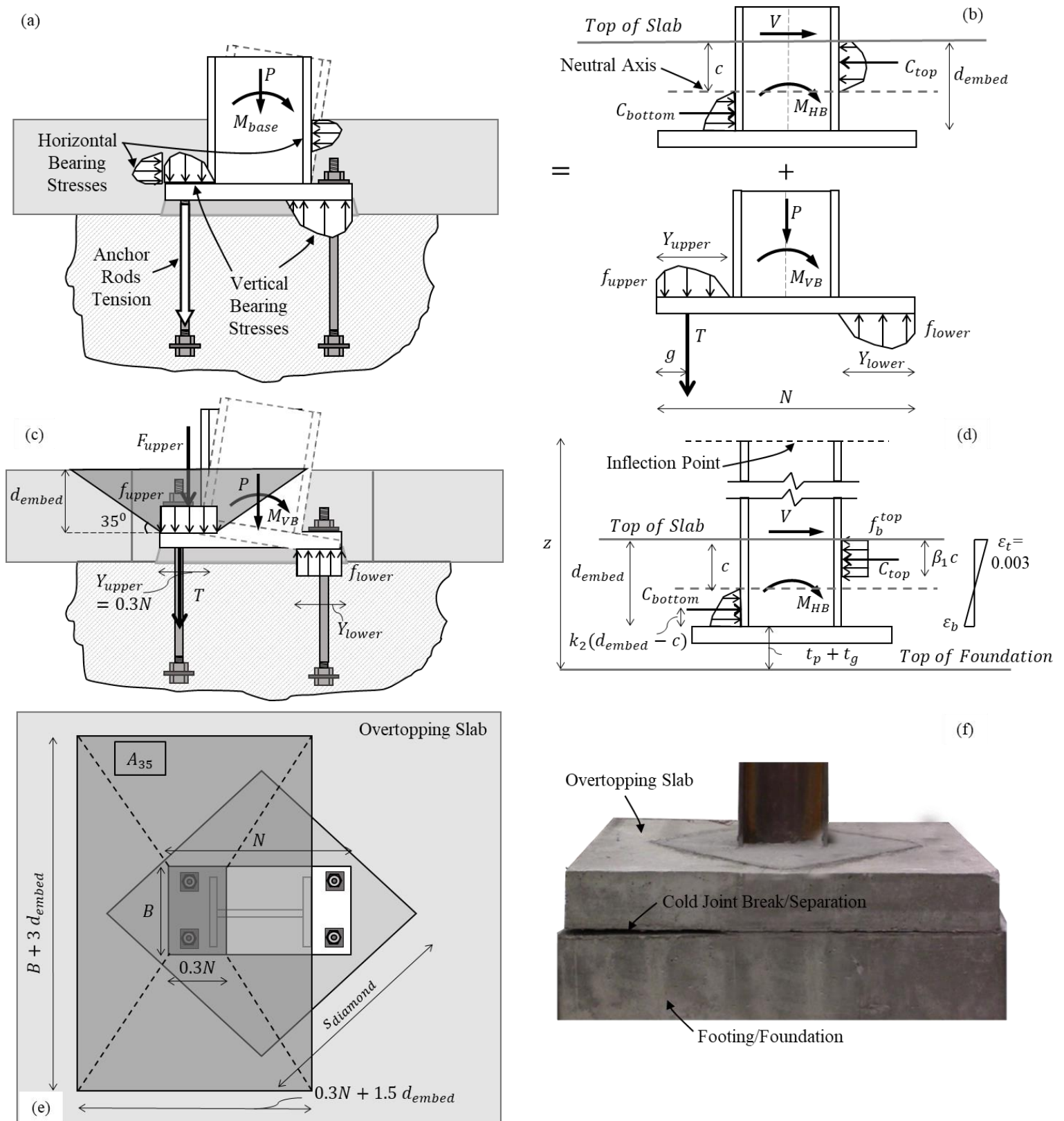


Figure 3.10 – Mechanisms and model for strength characterization – Method 2 (a) overall mechanism; (b) moment resisted due to horizontal forces and due to vertical forces; (c) elevation view of concrete breakout cone and vertical resistance mechanism model; (d) horizontal resistance mechanism model (modified Mattock and Gaafar 1981); (e) projected area of breakout cone failure A_{35} ; (f) observed failure mode in some of BYU experiments (slab separation).

3.6 MODELS FOR STIFFNESS CHARACTERIZATION

While the major focus of this study is to develop a strength model, the rotational stiffness characterization of such connections is also important, especially from the standpoint of structural performance assessment where rotational stiffness of column base connections plays a critical role (Zareian and Kanvinde 2013, Falborski et al. 2020). Although this study does not develop a new model for rotational stiffness characterization, it evaluates two existing models against all the available test data summarized in Table 3.3. The first is an approach presented by Kanvinde et al. (2012) for exposed base plates referred to as UC-Exposed Method, which does not consider the effect of the blockout or overtopping slab, whereas the second approach is by Richards et al. (2018), referred to as BYU Method, which considers the effect of the blockout and overtopping slab. Both these methods are now briefly summarized and applied to the test data outlined previously in Table 3.3.

The UC-Exposed method leverages internal force distributions from AISC *Design Guide 1* to determine the rotational stiffness of exposed base connection. The method considers deformations from the base plate, anchors and concrete foundation (as shown in Figure 3.11a) to calculate the overall connection rotation under a given moment. Although the method is specifically developed for exposed column base connections (without the blockout), it is discussed in this study to examine its suitability for use in predicting the stiffness of blockout connections. The BYU method for calculating the rotational stiffness of blockout connection estimates the rotational stiffness of the embedded base plate, and then represents it as an equivalent spring at the end of a beam in an elastic foundation, which represents the embedded portion of the column. Table 3.3 summarizes the ratio between the rotational stiffness calculated for each of the tested specimens β^{test} from the considered programs and the predicted rotational stiffness using the two methods outlined above

(i.e., $\beta_{UC-Exposed}^{Method}$ and β_{BYU}^{Method}). A graphical representation of the test-predicted ratio for the rotational stiffness against the column embedment is also shown in Figures 3.11c-d.

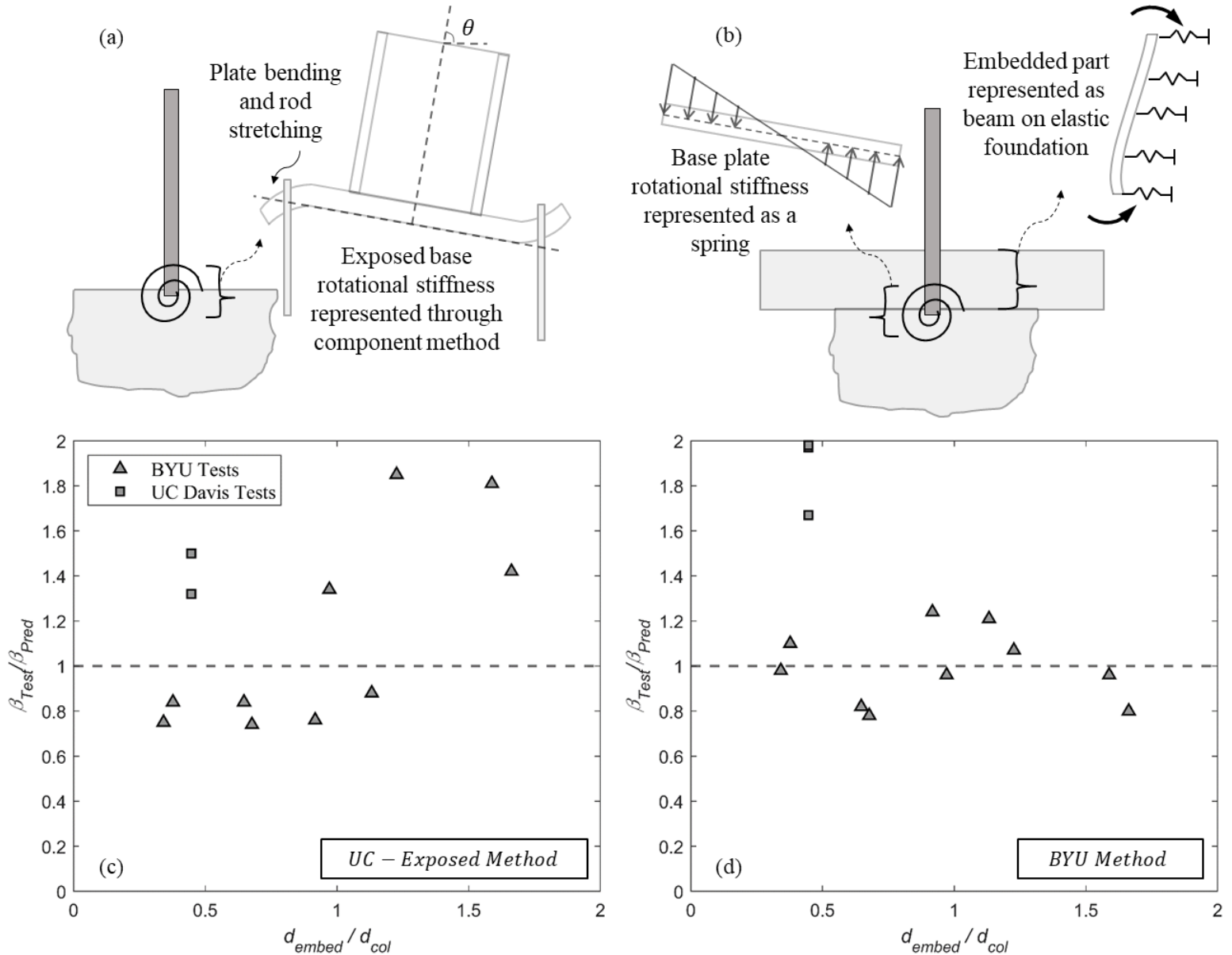


Figure 3.11 – Key elements of stiffness method proposed by (a) UC Method - Kanvinde et al. (2012) and (b) BYU Method - Richards et al. (2018); (c-d) Test-predicted ratios for rotational stiffness from both methods.

Referring to Table 3.3, the average test-predicted ratio $\beta^{test}/\beta_{UC-Exposed}^{Method}$ is 1.24 with a CoV 0.38.

Whereas average test-predicted ratio $\beta^{test}/\beta_{BYU}^{Method}$ is 1.19 with a CoV 0.35. Referring to these values and Figures 3.11c-d, the following observations may be made:

- Both models provide reasonable estimates of the rotational stiffness, with some degree of uncertainty. While these errors (in the range of 19 to 25%) are not ideal, they may be acceptable in the context of structural performance assessment where the current practice is to simulate these connections as either fixed or pinned (i.e., a stiffness of zero or infinity). In fact, research by Zareian and Kanvinde (2013), and more recently by Falborski and Kanvinde (2022) suggests that some variation in base flexibility, in the neighborhood of the true flexibility does not significantly affect structural response.
- The efficacy of the methods does not appear to depend on the embedment (as shown in Figures 3.11c-d), or on axial load.

Based on the above two observations, the existing methods (particularly the BYU approach) are appropriate for estimating base stiffness in the current performance assessment content.

3.7 SUMMARY AND CONCLUSIONS

This study presents findings from three tests of blockout column base connections representative of construction practice in the United States. These findings synthesized with findings from similar experiments from two other test programs to evaluate current strength and stiffness estimation approaches for these connections, and to propose a new strength characterization method. The experiments reveal that the current strength characterization methods (including the AISC DG1 approach and another approach proposed by BYU) are somewhat inaccurate; the former because it does not consider the effect of the blockout concrete, and the latter because it is based on test

data that does not include axial load. To address this, a new method is proposed for strength estimation. This method assumes the formation of a mechanism within the connection, such that the total moment and shear is resisted by a combination of horizontal stresses in the footing that resist rotation of the column (similar to a deeply embedded connection or a coupling beam) and vertical stresses and anchor rod forces that resist rotation of the base plate (similar to an exposed base plate connection). The method predicts the strength of specimens from 15 specimens (from three test programs) with good accuracy, and shows minimal dependence on test parameters, suggesting that it represents the physics of response with fidelity. The strength model may be used in two contexts:

1. To reduce conservatism in the design of exposed base plate connections, which is usually conducted using AISC DG1 type approaches, anticipating an increase in strength due to the installation of the blockout. In this context, it is important to note that the strength model predicts the maximum strength of the connection as a whole, whereas the aim of conventional design approaches is to preclude yield in any of the members. However, the test data from this test program as well as others (e.g. Richards et al. 2018; Hanks and Richards 2019) indicate that the connection yield moment (which typically corresponds to the yielding of the first component, e.g., the anchors) is roughly 80% of the ultimate strength, with modest variability. This factor may be used in conjunction with the proposed method to design the connection.
2. For seismic performance assessment. As discussed previously, exposed base plate connections are used in both lateral load resisting frames as well as gravity frames. Cumulatively, their resistance can significantly affect structural performance, particularly collapse resistance. Thus, simulating the nonlinear response of these connections in pushover analysis or Nonlinear Response History Analysis in the context of FEMA P695 (Applied Technology Council 2009)

is important. Typically, these connections are represented as rotational springs with calibrated hysteretic properties (e.g., Torres-Rodas et al. 2018). Strength estimates for blockout connections calculated from the proposed method may be used within such models.

The study also evaluates rotational stiffness models, and concludes that the model developed at BYU (Richards et al., 2018) provide good estimates of base flexibility, and will possibly offer vast improvements in assessment of structural performance (including internal force distributions and seismic performance) as compared to assumptions of pinned or fixed bases. In closing, it is important to note some limitations of the study and the strength model proposed herein. First, the test configurations sampled only a limited set of parameters. While these parameters are fairly realistic, extrapolation of test results to highly dissimilar configurations may be prone to error. For example, the strength model begins to lose accuracy for embedments that are significantly deeper than common floor slabs. Similarly, the plastic mechanism used in the model implicitly presumes some ductility in various load resisting mechanisms (e.g., anchors and concrete crushing); this too may be compromised for different details or material grades. Addressing these issues will require additional study.

CHAPTER 4

SEISMIC PERFORMANCE OF EMBEDDED COLUMN BASE CONNECTIONS WITH ATTACHED REINFORCEMENT: TESTS AND STRENGTH MODELS

4.1 INTRODUCTION

Embedded Column Base (ECB) connections in seismically designed Steel Moment Frames are commonly used to connect the steel columns to concrete foundations for mid- to high-rise buildings. Unlike low-rise buildings for which Exposed-Type Base Plate Connections (where a base plate is welded to the column with attached anchor rods to the foundation – See Figure 4.1a) are suitable, in mid- to high-rise frames, the embedment is required to resist large base moments and provide fixity through bearing of column flanges against concrete, as shown in Figure 4.1b. The column is usually welded to a base plate resting in a thin concrete layer for leveling purposes. Face bearing plates are often employed on the top of concrete surface to transfer axial compression and facilitate the formation of a shear panel as prescribed for similar connections (e.g., Composite Beam-Column Connections or Steel Coupling Beams in Concrete Shear Walls).

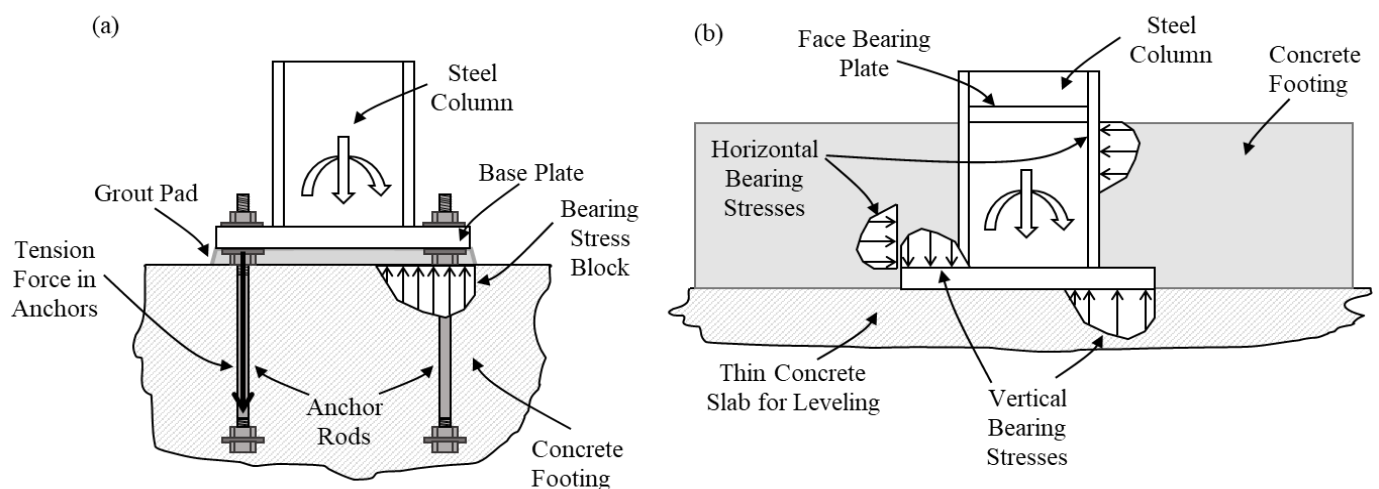


Figure 4.1 – Column base connections and force transfer mechanisms: (a) exposed type; (b) embedded type (ECB Connection)

Significant research has been conducted on the Exposed-type Base Connection in the last two decades, including large-scale experimental testing (Astaneh et al. 1992; Fahmy et al. 1999; Gomez et al. 2010; Kanvinde et al. 2015; Trautner et al. 2017; and Hassan et al. 2022), analytical (Wald et al. 2000), and computational simulations for both component (Inamasu et al. 2020; Hassan et al. 2022), and frame (Falborski et al. 2020), leading to the development of design considerations (AISC Design Guide One – Fisher and Kloiber 2006; AISC 341-16; SEAOC 2015 Seismic Design Manual SSDM). In contrast, research on ECB connections is sparse, with no experimentally-validated guidelines or methods for design, and only limited finite-element parametric studies (Pertold et al. 2000a, b). Current design practice in the United States, rely on adaptations of methods developed for other similar components such as Composite Beam-Column Connections (ASCE 1994) and Steel Coupling Beams Embedded in Concrete Shear Walls (Marcakis and Mitchell 1980; Mattock and Gaafar 1982; Harris et al. 1993; Shahrooz et al. 1993). The AISC Seismic Provisions (AISC 341-16) and the AISC Seismic Design Manual (AISC 2012) suggest the use of the method developed by Mattock and Gaafar (1982) for strength characterization and design of ECB connections. These ad hoc adaptations (in the absence of experimental data) are susceptible to inaccuracies owing to the disregard of behavioral aspects specific to the ECB connections including: (1) concrete confinement effect which is limited around a thin shear wall or a composite beam-column connection; (2) the presence of a base plate welded to the column section; (3) the presence of axial load which is higher in case of columns; as well as (4) other differences in reinforcing bar patterns. Other studies related to ECB connections (Cui et al. 2009; Richards et al. 2018; Hanks and Richards 2019) examined the effect of an overtopping slab-on-grade on top of an Exposed-type column base connection. This type of connection (known as blackout column base connection) is distinct from ECB connection in fundamental behavioral

characteristics wherein the concrete embedment is incidental (for construction purposes) and the primary mode of moment resistance is that of the base uplift (through anchor rod tension and vertical bearing on the overlying slab). As a consequence, they are not readily applicable to ECB connections.

Previous experimental studies (Grilli et al. 2017), on a similar project on ECB connections representative of the United States construction practice (similar to that shown in Figure 4.1b) serve as the only test data available on the seismic performance of such connections. These five specimens featured wide flange steel cantilever columns embedded within a concrete footing and subjected to cyclic lateral deformation history under a constant axial force (compression and tension). The main variables were the column size, embedment depth, and axial load. The specimens were designed with minimal longitudinal and transverse reinforcement such that observed failure modes and strengths were associated (to the possible extent), with the concrete only.

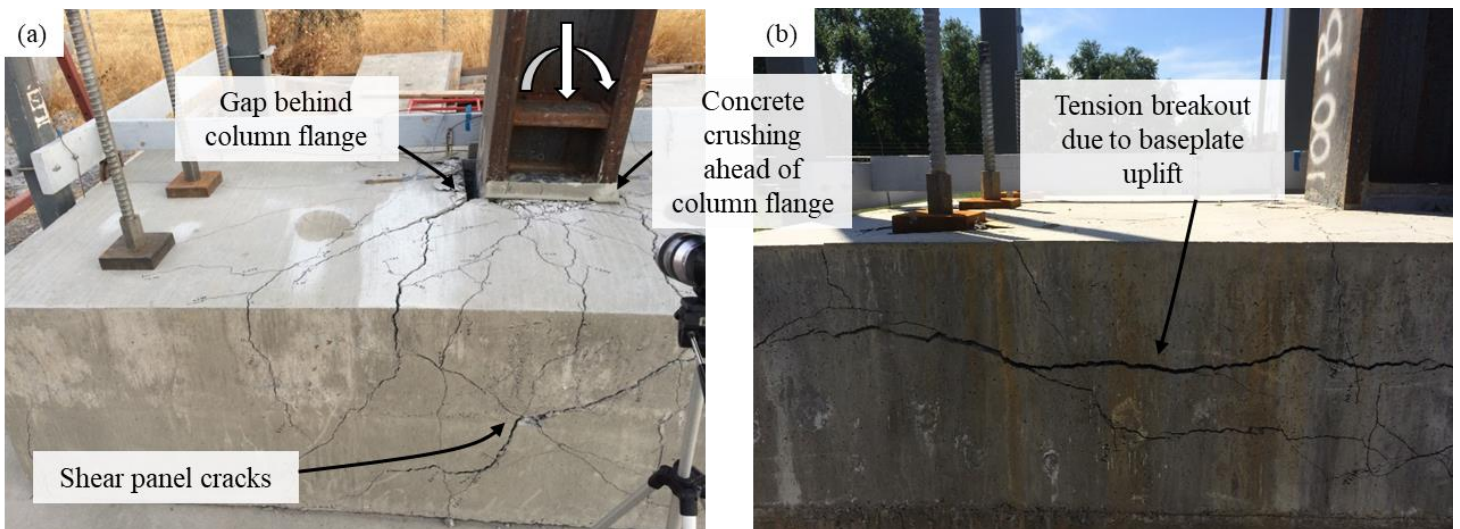


Figure 4.2 – Experimental program (Grilli et al. 2017): damage patterns suggesting modes of failure/deformations governed by (a) horizontal bearing, and (b) vertical bearing

The results from this experimental program (Grilli et al. 2017 and Grilli and Kanvinde 2017), provided insights into the fundamental physics of the ECB connections, including failure modes which informed the development of strength models suitable for the design of ECB connections. The study postulated internal stress distributions and mechanisms for resisting applied moments and axial loads in ECB connections. Figure 4.1b shows two primary mechanisms of moment resistance, as outlined by Grilli and Kanvinde (2017): (1) horizontal bearing stresses against the column flanges along with a complementary shear panel zone (similar to that observed in composite steel beam column connections: ASCE 1994; Sheikh et al. 1989; Cordova and Deierlein 2005); and (2) vertical bearing stresses resisting uplift of the base plate. While all the tested specimens suggested that the strength of such connections is determined by the ultimate horizontal bearing stress of the concrete ahead of the column flange (which is consistent with the current design standards i.e., AISC 341-16 and the AISC Seismic Design Manual), other failure modes might as well be active as indicated by Grilli and Kanvinde (2017). This includes: (1) Tension breakout of concrete due to the uplift of the base plate on the tension side of connection, and (2) Shear cracking or failure in the web panel in the concrete footing. Figures 4.2a-b show posttest photographs illustrating the failure modes observed from two specimens in the experimental program (Grilli et al. 2017) with different embedment depths; similar response was observed for other tests.

Notwithstanding the valuable contribution from the experiments to provide direct assessment to the response of ECB connections and support a strength characterization method, the study is limited by a relatively small data set and the examination of a single detail. The specimens featured only one generic detail (Figure 4.1b) with the absence of major reinforcement. Other detail

(commonly used in practice) may feature additional reinforcement (welded/attached to the column) which have the potential to affect the failure modes of horizontal bearing and vertical bearing (specifically the tension-breakout), as well as improve the energy dissipation characteristics of the connection.

Motivated by these issues, this study presents a series of five full-scale experiments of ECB connections with attached reinforcement bars along with a proposed method for strength characterization of ECB connections. The testing program demonstrates ECB connection details that are commonly used by the construction practice in the United States. Figure 4.3 schematically illustrates the main features for the tested details developed in consultation with an oversight committee of practitioners and fabricators (see “Acknowledgments”). These specimens feature a similar detail to the one examined by Grilli et al. (2017), with the exception of reinforcement fixtures attached to the embedded column flanges with varying configurations, size, confinement effect. Two main techniques for reinforcement attachment are examined, namely, Welded reinforcement bars to the column flange (deformed weldable bars – commonly used in practice); and U-bar hairpin reinforcement bars (recommended by AISC Seismic Provisions 341-16 for steel coupling beams) anchored by the embedded portion of the column and alternating to engage both column flanges (See Figure 4.3b). The main objectives of this study are to: (1) Query the effect of additional reinforcement on the seismic performance of ECB connections, and (2) critically examine the assumptions commonly used to design ECB connections along with the available strength models/approaches while providing recommendations for improved design of ECB connections.

The next section begins by briefly providing relevant background on prevalent approaches/models for estimating the strength of ECB connections, followed by a description of the experimental program and evaluation of the strength characterization approaches (along with the new strength estimation method) against test data.

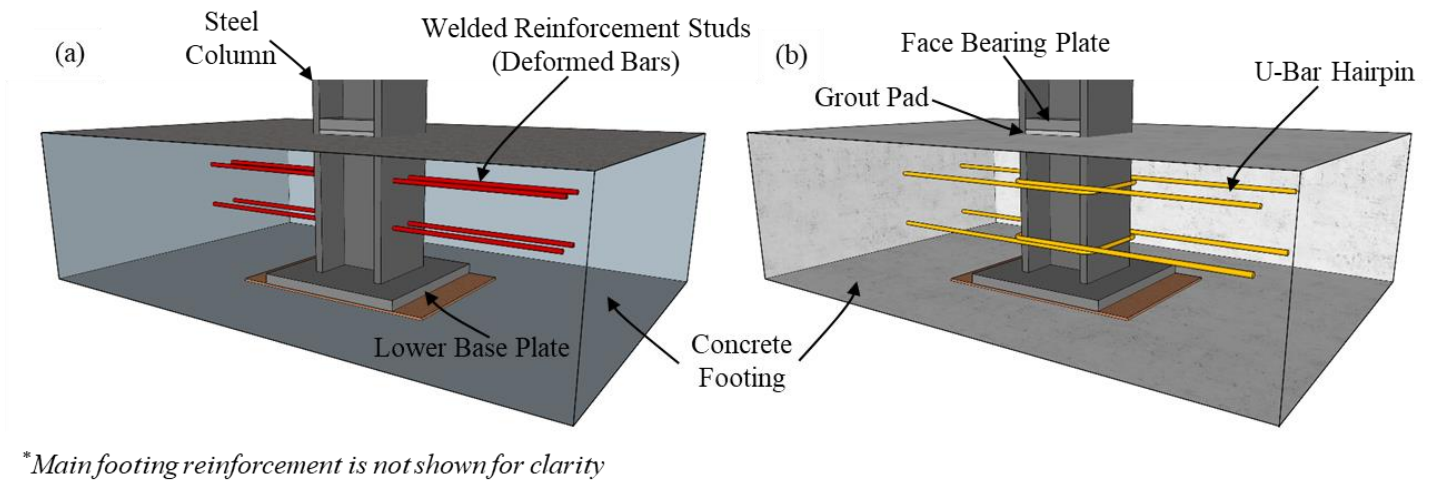


Figure 4.3 – Details under investigation for the experimental program: (a) Welded Reinforcement Stud, and (b) U-bar Hairpin

4.2 CURRENT PRACTICE AND AVAILABLE STRENGTH MODELS

As previously discussed, the current practice (in the United States) and design provisions (AISC Seismic Design Manual) adapt the flexural and shear resistance of a steel coupling beam embedded in a concrete shear wall for the seismic design of ECB connections. Figure 4.4a illustrates the assumptions adopted by this approach (referred to here after as AISC SDM Method). Referring to this figure, the applied moment and shear are resisted through the development of bearing stress blocks on both sides of the embedded column flanges. Equation 4.1 below provides a closed form solution for the moment capacity, obtained by solving for the force and moment equilibrium based on the assumed stress blocks. This equation is based on the work done by Mattock and Gafaar for

steel coupling beams embedded in concrete shear walls and subjected to reversed cyclic loading (1982).

$$M_{base}^{AISC\ SDM} = 1.54 \sqrt{f'_c} \left(\frac{b_w}{b_f} \right)^{0.66} \beta_1 \times b_f \times L_e \times \frac{g}{2} \times \left(\frac{0.58 - 0.22 \times \beta_1}{0.88 + \frac{g}{2 \times L_e}} \right) \quad (4.1)$$

Where f'_c is the specified compressive strength of concrete (in ksi); b_w (in inches) is the width concrete foundation perpendicular to the loading direction (b_w is the thickness of wall pier in the original equation); b_f (in inches) is the width of the embedded section (column) flange; L_e (in inches) is the embedment depth of the steel column measured from the face of the foundation (as shown in Figure 4.4a); $g/2$ (in inches) is the distance from the top surface of the foundation to the inflection point of the column; and β_1 is the factor relating the depth of equivalent rectangular stress block to the neutral axis depth c as defined in ACI 318-19 (ACI 2019). The term $\left(\frac{b_w}{b_f} \right)^{0.66}$ accounts for the effect of concrete confinement and spread of compressive stress ahead of the column flange such that the value 0.66 is calibrated to match experimental results by Mattock and Gaafar (1982). Referring to Figure 4.2a, the values c/L_e and k_2 are assumed to be 0.66 and 0.36, respectively as reported by Mattock and Gaafar (1982) for design purposes. From the perspective of ECB connections, the following aspects of this method are problematic: (1) it assumes that the entire moment is carried solely by the bearing against the flanges (i.e., it does not consider the effect of the embedded base plate and its contribution to moment resistance), (2) the term reflecting the effect of concrete confinement is unbounded which has the potential of overestimating the bearing stresses in concrete foundations (which are significantly wider than the embedded steel section as compared to shear walls), and (3) several factors relating to the mechanics of the method (for example, the ratio of the neutral axis location to the depth of embedment c/L_e and consequently the value k_2 – see Figure 4.4a) have been particularized for

Figure 1(a) shows a schematic diagram of a column subjected to shear force V and base moment M_{base} . The column is embedded in a concrete slab. The inflection point is shown above the slab. The effective depth of the column is c . The base of the column is fixed to the slab. The slab has a thickness of $2(L_e - c)$. The concrete strength is f_c . The effective depth of the slab is d_{eff} . The slab is subjected to a horizontal bearing stress and complementary panel shear cracks. The slab is supported by a foundation. The slab is subjected to a horizontal bearing stress and complementary panel shear cracks.

Figure 1(b) shows a schematic diagram of a column subjected to shear force V and base moment M_{base} . The column is embedded in a concrete slab. The inflection point is shown above the slab. The effective depth of the column is c . The base of the column is fixed to the slab. The slab has a thickness of $2(L_e - c)$. The concrete strength is f_c . The effective depth of the slab is d_{eff} . The slab is subjected to a horizontal bearing stress and complementary panel shear cracks. The slab is supported by a foundation. The slab is subjected to a horizontal bearing stress and complementary panel shear cracks.

Grilli and Kanvinde (2017) developed a strength model based on physical observations of connection damage and failure from test data and simulations. The model provides a fundamental understanding of the internal force transfer in embedded base connections (schematically illustrated in Figure 4.4b). Referring to Figure 4.4b, the key assumption of the method is that the total applied base moment (denoted M_{base}) is resisted by two mechanisms: (1) horizontal bearing stresses against the column flange, accompanied by the formation of a shear panel action – this portion of the moment is denoted M_{HB} , and (2) vertical bearing stresses against the base plate that resist its rotation – this moment is denoted M_{VB} . Thus,

wherein M_{HB} denotes the moment carried by horizontal bearing stresses, and M_{VB} denotes the moment carried by vertical bearing stresses. The distribution of moments between these two

mechanisms is determined through a semi-empirical equation that is inspired by a beams-on-elastic foundations solution (Hetenyi 1946). In practical terms, the moments carried by each of these mechanisms is determined from the following equations:

$$M_{VB} = \alpha \times M_{base} \quad (4.3)$$

and,

$$M_{HB} = (1 - \alpha) \times M_{base} \quad (4.4)$$

The term α , which determines the split is calculated as:

$$\alpha = 1 - (d_{embed}/d_{ref}) \geq 0 \quad (4.5)$$

in which,

$$d_{ref} = \frac{C}{\rho}, \text{ where } \rho = \left(\frac{E_{concrete}}{4 \times E_{steel} \times I_{column}} \right)^{\frac{1}{4}} \quad (4.6)$$

The term α represents the fraction of the moment resisted by vertical bearing on the embedded section such that, α approaches 0 (i.e., all the moment carried by horizontal stresses) as d_{embed} approaches ∞ . The terms corresponding to the elastic modulus of steel E_{steel} , the second moment of inertia of the steel column I_{column} and the elastic modulus of concrete $E_{concrete}$ (which is assumed to indirectly represent the effective stiffness of the concrete per unit length of the column – analogous to a subgrade modulus) set the scale over which the horizontal stresses attenuate, based on an interpretation of the Hetenyi solution for beams on elastic foundations (1946). The basis of the proposed equations and the underlying physics is detailed in Grilli and Kanvinde (2017). The term C is a calibration constant (equal to 1.77), and in the original work by Grilli and Kanvinde (2017), is particularized to the case of a column base plate embedded in concrete, without any attachments (i.e., welded reinforcement, anchor rods, etc.). This constant implicitly

accounts for the rotational fixity of the base plate embedded within the concrete. The flexural resistance of the connection is then be calculated as follows:

$$M_{base}^{Grilli} = \frac{1}{1-\alpha} \times \left(\beta \beta_1 f'_c b_j \times \left\{ d_L d_{eff} - \frac{d_L^2 + d_U^2}{2} \right\} \right) \quad (4.7)$$

Where β is assumed to be constant and equal to 2 to account for the confinement effect (while keeping it bounded – compared to the term proposed by the SDM Method). b_j (in inches) is equal to $(b_f + B)/2$ and accounts for the concrete compression field forming outside of the panel zone. The effective embedment depth d_{eff} is defined as the minimum of d_{embed} and d_{ref} . Referring to Figure 4.4b, the depths of the horizontal concrete stress blocks (lower and upper, namely, d_L and d_U , respectively) are determined by solving equilibrium equations (for moment and shear), where the maximum resistance proposed by Grilli and Kanvinde (2017) occurs when $d_L + d_U$ reaches 60% of the effective embedment depth. This assumption is consistent with the approach adopted for composite connections design by the ASCE guidelines for composite connections (ASCE 1994). The above equation assumes that no limit states are engaged either in the embedded base plate or the vertical stresses restraining it until the peak moment is reached (i.e., the horizontal bearing failure limits state occurs before vertical bearing failure).

Both models do not account for the reinforcement attached to the column flanges (commonly used in practice), either through ignoring its contribution (as per the AISC SDM Model – where the reinforcement is only prescribed for force transfer) or by not accounting for its presence in the mechanical model through the equilibrium equations (as per Grilli and Kanvinde 2017). This is problematic as the presence of additional reinforcement (attached to the column flange) greatly influences the strength and stiffness of the connection, which could possibly affect the failure modes/limit states observed. In the next section, a description of the experimental program

featuring ECB connections with reinforcement attachments is presented. The results from the tested specimens are then used to provide direct comparisons with the available strength models while providing recommendations for an improved model for strength characterization and design of ECB connections.

4.3 EXPERIMENTAL PROGRAM

This section outlines the experimental test setup, test matrix and loading protocol. Figures 4.5 and 4.6 illustrate important features of the test setup and specimens detailing, respectively, whereas Table 4.1 summarizes the test matrix along with key experimental results.

Test Setup

Figure 4.5 shows the test setup, including the specimen. Specific aspects of the test setup and specimens are outlined below:

- 1- All specimens featured wide flange cantilever columns. The height (9.5 ft above the surface of concrete) of load application was assumed to be the inflection point in a first story column. The load was applied through a servo-controlled hydraulic actuator attached at the top. The columns were all ASTM A992 Grade 50 (345 MPa) and were designed to remain elastic throughout the test.
- 2- For axial compression application, two hollow hydraulic jacks were positioned at the ends of a crossbeam (shown in Figure 4.5) and connected to tension rods which were attached to a freely rotating clevis, such that the axial forces did not introduce ($P - \Delta$) moments and acted as follower forces.
- 3- The columns were placed on a plywood sheet (with 1 in. thickness and same plan dimensions of the lower base plate) to provide a more realistic supporting condition such

that columns are usually set/supported on a thin unreinforced slab for erection purposes (rather than directly on bare soil).

- 4- Plates were provided at the top (stiffener-like face bearing plates) and the bottom (base plates) of the embedment region (See Figure 4.6), consistent with the design practice. The bottom plate is similar to the ones used in exposed column base connections to allow the column to be supported stably during concrete casting, while also providing resistance to uplift. The top plates were added to provide resistance to compression by distributing the axial force from the column to the foundation in direct bearing.
- 5- The pedestals were fastened to the laboratory floor with 6 pre-tensioned threaded anchors (3 on each side) designed to have minimal effect on the stress distribution in the vicinity of the column.

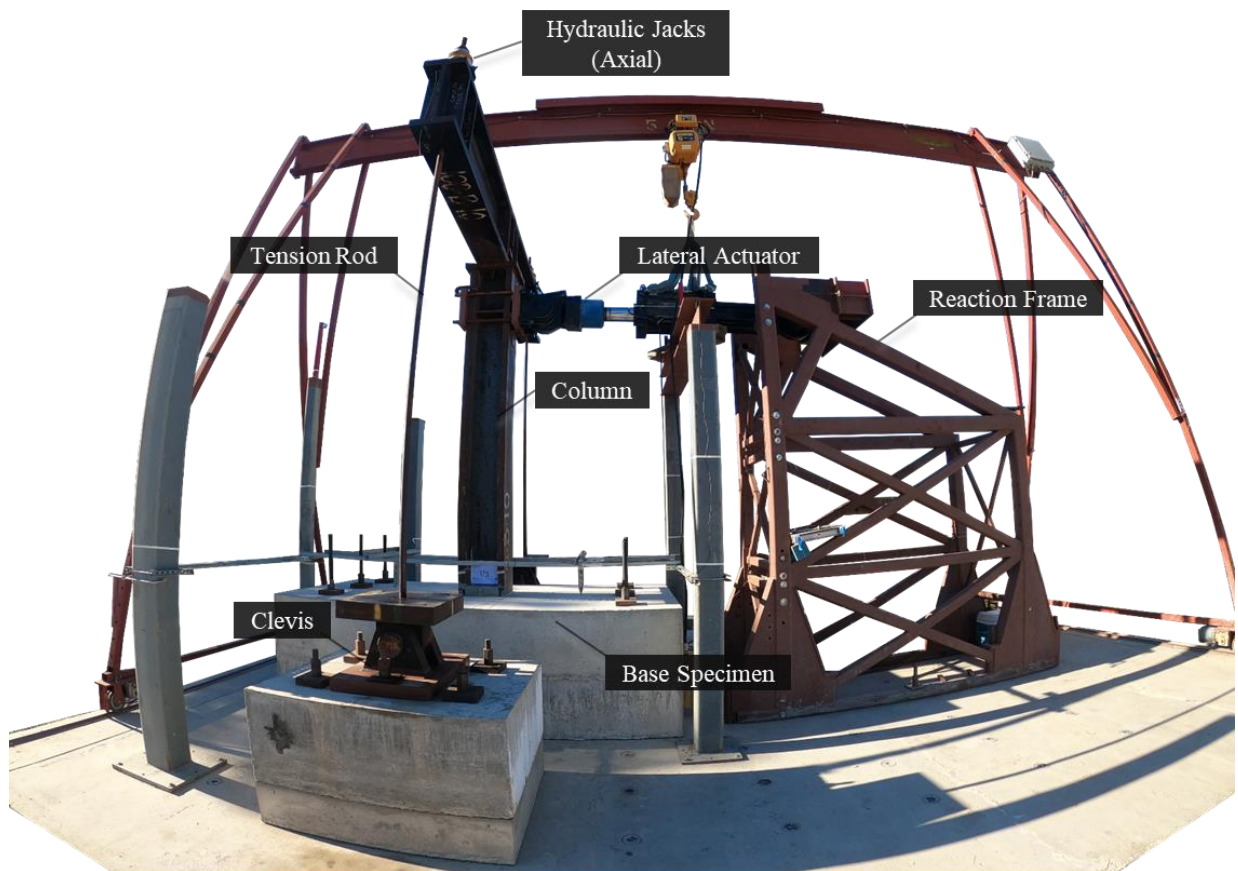


Figure 4.5 – Wide angle view of test setup

Table 4.1 – Tests Matrix and Key Results

Test ^a	Axial Load <i>P</i> [kip]	Column Size <i>b_f</i> [in.]	Embed. Depth <i>d_{embed}</i> [in.]	<i>z^b</i> [in.]	Base Plate <i>t_p</i> x <i>N</i> x <i>B</i> [in.]	Attached Reinforcement Grade	Reinforcement Configuration	<i>M_{max+}</i> ^{test} [k.ft]	<i>M_{max-}</i> ^{test} [k.ft]	$\frac{M_{max}^{test\ c}}{M_{max}^{AISC\ SDM}}$	$\frac{M_{max}^{test}}{M_{max}^{Grilli}}$	$\frac{M_{max}^{test}}{M_{max}^{Grilli-HB}}$	$\frac{M_{max}^{test}}{M_{max}^{Model}}$		
1	100	W14 x 370 (16.5)	20	113	2 x 30 x 30	Weldable Rebar Studs ASTM A706 Grade 60	(4) #4 (0.5” diameter)	994	1002	0.77	0.54	0.95	0.86		
2	100					1055		904	0.81	0.57	1.02	0.92			
3	100					1334	1109	1.03	0.70	1.23	1.15				
4	100					1196	908	0.92	0.65	1.16	0.99				
5	100	W18 x 311 (12)		113	2 x 34 x 28	U-bar Hairpin ASTM A615 Grade 60	(4) #4 (0.5” diameter) + Vertical Reinforcement (STR)	1220	820	1.05	0.72	1.37	1.09		
										Mean	0.92	0.63	1.15	1.00	
										CoV	0.14	0.13	0.15	0.12	
1G	100	W14 x 370 (16.5)			112	2 x 30 x 30	-	-	1902	1927	1.45	1.07	1.81	1.33	
2G	100	W18 x 311 (12)			112	2 x 34 x 28			1714	1599	1.44	1.05	1.87	1.23	
3G	-	W14 x 370 (16.5)		30	122	2 x 30 x 30			2759	2540	0.97	1.01	1.19	1.00	
4G	100				122				3042	2664	1.07	1.11	1.31	1.09	
5G	150 (T)				122				2803	2555	0.99	1.03	1.21	1.05	
											Mean	1.19	1.05	1.48	1.14
											CoV	0.20	0.04	0.23	0.12
									Mean (All)	1.07	0.84	1.33	1.09		
									CoV (All)	0.20	0.27	0.21	0.11		

^aNew tests are labeled from 1-5, whereas tests from Grilli et al. (2017) are labeled from 1G-5G.

^bMoment-to-shear ratio (i.e., distance from point of load application to top of concrete) – See Figure 4.10c

^c M_{max}^{test} is the maximum moment value of both directions of loading (positive and negative).

Test Matrix

Referring to Table 4.1, the following test parameters were varied: (1) the method of reinforcement attachment (welded versus anchored), (2) the reinforcement area (the total area added – with varying rebar sizes), (3) the column size, and (4) the addition of supplemental vertical reinforcement (stirrups) along the length of the concrete pedestal. Parametric values of the test matrix were selected considering similarity to construction practice and limitations of the test setup; specifically:

- 1- The selected columns were sized to ensure failure in the connection (i.e., remain elastic).
For a real concrete pedestal or grade beam, the embedded column (hypothetical column) is smaller as compared to the ones used in this study. In turn, the embedded depths are comparable to those commonly used for moment frames.
- 2- Compressive axial loads were selected to be almost 10-20% of the axial yield capacity of such hypothetical column that would have an embedment depth similar to the one employed in the study.
- 3- The footing design was similar to the specimens tested by Grilli et al. (2017) in terms of concrete dimensions and nominal reinforcement. The footings were provided with minimal longitudinal and transverse reinforcement such that the observed failure modes and strengths were associated (to the extent possible), with concrete only. The column embedment depth d_{embed} , footing dimensions and reinforcement are illustrated in Figure 4.6.
- 4- Referring to Figure 4.6, For each test (out of 5 total specimens), different additional reinforcement attachments details were installed. All tests featured two rows of attached reinforcement bars (close to the face of the concrete footing, and near the end of the

embedment length). The attached reinforcement was fully developed in tension by providing an adequate tension development length as per ACI 318-19 (ACI 2019). The location of the attached reinforcement were selected in accordance with the AISC 341-16 and AISC SDM provisions (AISC 2016; AISC 2018) such that: (a) The first region (top row) of the attached reinforcement coincided with the longitudinal footing reinforcing bars closest to the face of the foundation; and (b) the second region (bottom row) is placed a distance no less than $d_{col}/2$ from the termination of the embedded length.

- 5- Test #1 presented the method of attachment through arc welding of 1/2 in. diameter weldable stud rebars (ASTM A706 Grade 60) – see Figure 4.3a, whereas Test #2 featured #4 (1/2 in. diameter) U-bar hairpin reinforcement (ASTM A615 Grade 60) anchored through the column embedment (alternating in each row to engage the flanges in both loading directions). Test #3 featured the case of bundled U-bar hairpin reinforcement with different diameter as a total of 4 #6 U-bar hairpins per row (3/4 in. diameter). For Tests #4 and 5 a series of supplemental vertical reinforcement/stirrups (detailed in Figures 4.6) were installed to query its effect on avoiding some failure modes (tension breakout) and increasing the connection capacity.
- 6- The test matrix may be considered fractional factorial, such that, subsets of tests examine the effects of isolated test variables. For example, Tests #1 and 2 provide a direct examination of the effect of different attachment techniques (i.e., arc welding versus anchoring/fixing), whereas Tests #2 and 3 provide an interrogation of the effect of reinforcement area/size. In addition, Tests #2 and 4 allow the investigation of the vertical reinforcement (stirrups) effect, whereas Tests #4 and 5 directly examine the effect of column width/size. It is worth mentioning that specimens from this program also allow

direct comparison with tests from the experimental program by Grilli et al. (2017), wherein the test variables as the general effect of horizontal reinforcement as well as column width could be examined, as discussed in the subsequent section.

Standard cylinder tests were performed for concrete pours as well as casted grout for all specimens. Sample tests from the attached reinforcement (both welded studs and U-bar hairpins) used in the experiments are also tested. Table 4.2 summarizes the results of ancillary tests for measured material properties which are used for results analysis and analytical models interpretation.

Table 4.2 – Summary of measured material strengths from ancillary tests

Test	Number of samples ^a	Yield Strength F_y^{rod} ^b [ksi]	Ultimate Strength F_u^{rod} [ksi]	Concrete Compressive Strength f'_c ^c [ksi]	Grout Compressive Strength f_{grout} ^c [ksi]
ASTM A706 - Grade 60 Reinforcement	2	71.2	94.2	-	-
ASTM A615 - Grade 60 Reinforcement	2	65.0	102.5	-	-
Concrete Cylinders	5	-	-	4.0	-
Grout Cylinders	4	-	-	-	8.50

^a Average values for tested samples are presented.

^b Measured yield stress for ASTM A706 rods is based on the 0.2% offset method.

^c Compressive strength for concrete and grout cylinders is measured on the day of full-scale test.

Loading Protocol

For all test specimens, the axial compression was first introduced and held constant while the lateral deformation history (expressed in terms of column drift ration) was applied. Figure 4.8 illustrates the employed protocol consisting of ATC-SAC loading history (Krawinkler et al. 2000) applied in an increasing manner until 6% drift amplitude (one specimen reached 7%). The ATC-SAC loading history was selected to demonstrate performance of the connection under seismic demand.

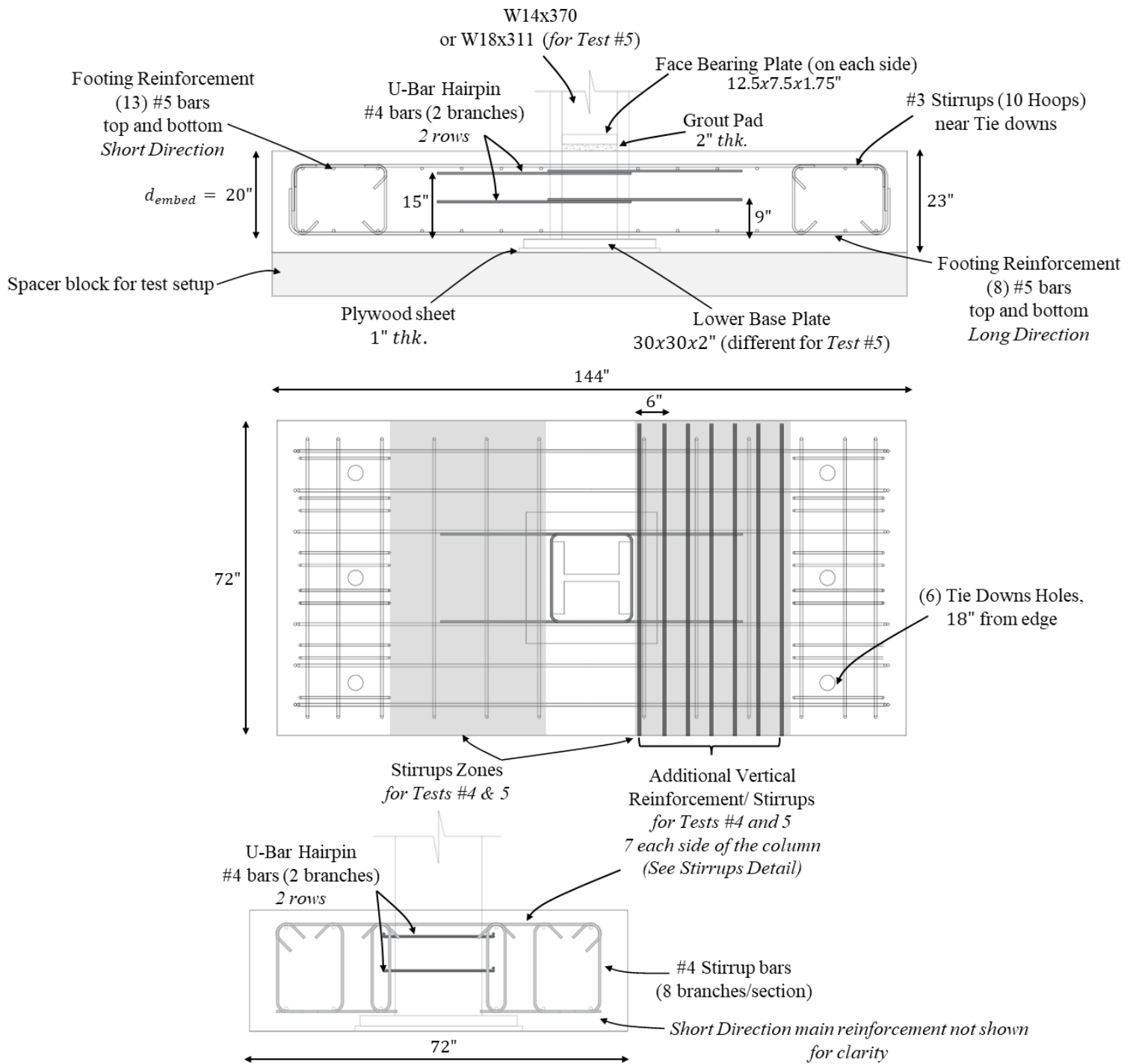


Figure 4.6 – Specimen detailing (see Table 1 for different parameters across the tests)

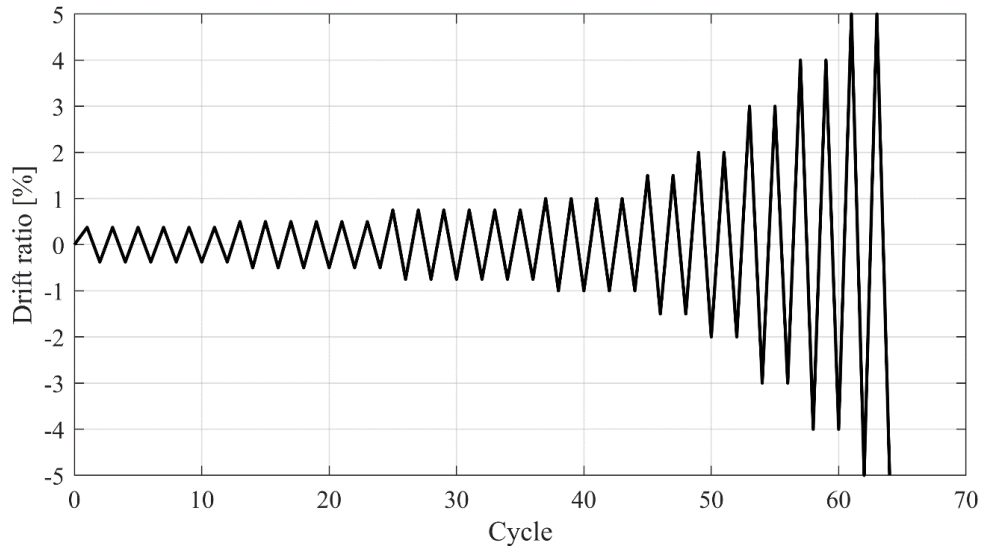


Figure 4.7 – Loading protocol with ATC-SAC (Krawinkler et al. 2000) loading history

4.4 EXPERIMENTAL RESULTS

Figures 4.8a-e show the load-deformation (specifically the moment-rotation curves) of all the five specimens after subtracting the elastic column rotations from the overall drift. Figures 4.9a-c show photographs of damage progression and failure modes for the tested specimens, whereas Table 4.1 shows key results, specifically with respect to model predictions. A qualitative assessment of experimental response for the tested specimens is now presented, to facilitate the interpretation of quantitative data, which is presented subsequently.

Qualitative discussion of failure modes

Figures 4.9a-c show photographic illustrations of damage and failure throughout the applied loading history. All specimens followed a qualitatively similar damage progression, with some exceptions/variations pertaining to the connection (reinforcement) detailing. During the initial stages of loading (with drift applied less than 1%), minor cracks initiated at the corners of the

column (flanges) as shown in Figure 4.9a. Followed by this, diagonal shear cracks formed on the sides of the block accompanied by a vertical crack in the concrete behind the column flanges (where the tension in the reinforcement bars is the highest), which grew in width as loading progressed with spalling of the concrete ahead of the column flanges. These vertical cracks effectively compromise the vertical/uplift capacity of the base plate (as explained later). As the applied drift increased, the diagonal shear cracks on the sides of the concrete block grew in width as an indication of development of concrete panel (however, not controlling the failure). The final failure mode varied from one specimen to another based on the additional vertical reinforcement (stirrups) installed. One of two scenarios occurred (shown photographically in Figures 4.9b-c), these are:

- 1- In Tests #1, 2 and 3, the final failure was accompanied by a breakout on the tension side of the connection. This failure mechanism is similar to the well-known anchor pryout failure modes in concrete (Andreson and Meinheit 2007) which was observed in similar details by Grilli et al. (2017) – see Figure 4.2b. As the base moment is shared by the vertical and horizontal bearing mechanism (as previously discussed), the pryout failure occurs as the moment resisting the uplift of the base plate reaches a critical value.
- 2- For Tests #4 and 5 (featuring additional stirrups/vertical reinforcement-detailed in Figure 4.6), the presence of supplemental reinforcement mitigated the final tension breakout failure (cone failure described above), instead the failure occurred at the interface of the vertical crack forming behind the column flanges (as shown in Figure 4.9c) at a location between installed stirrups. No spreading of failure (i.e., cone formation) was observed for such tests.

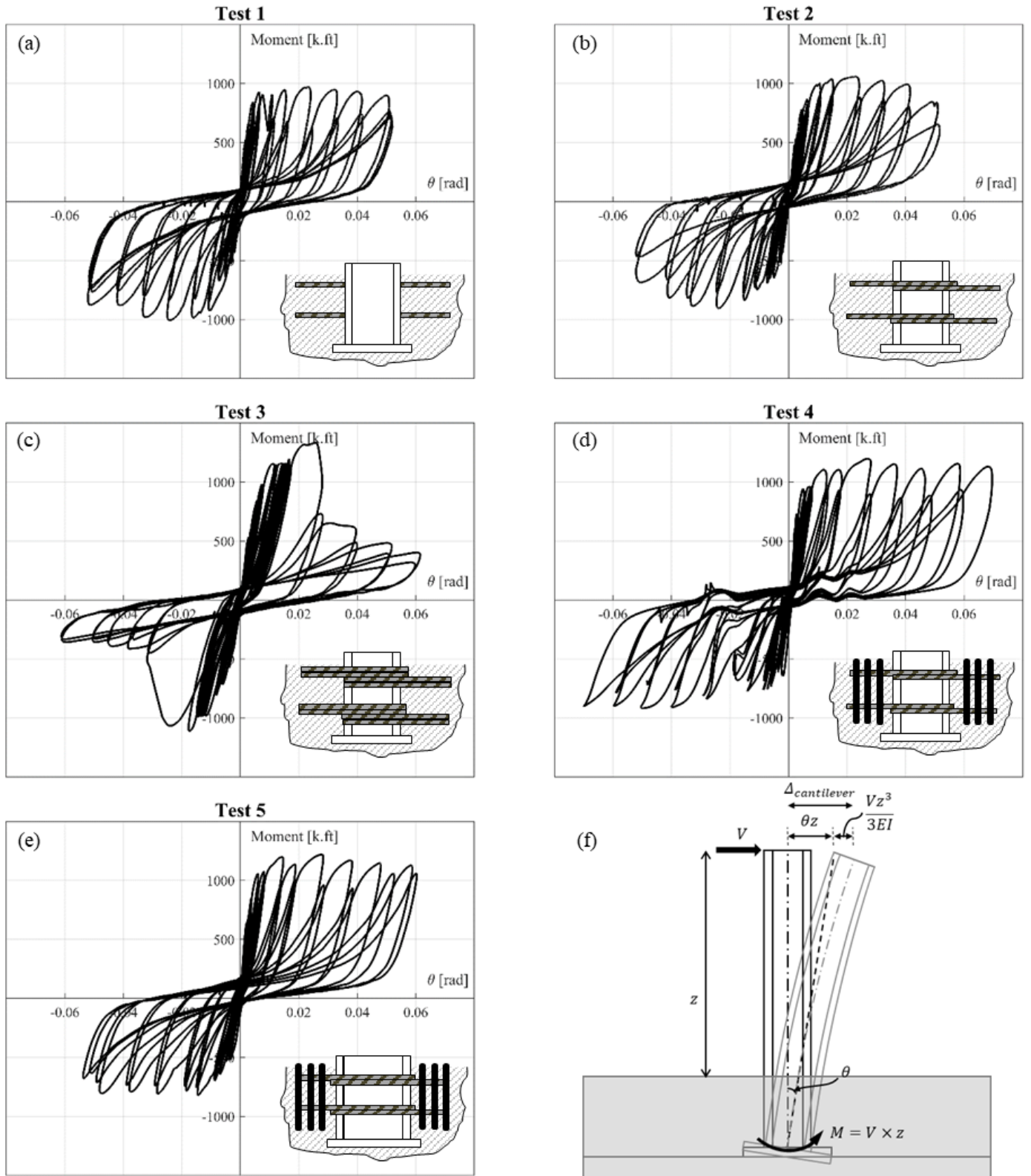
In all tests, the peak moment was achieved between 1.5% to 2% drift. After this, the strength at following cycles started to deteriorate as the concrete block started to separate, reducing the moment resisted by bearing ahead of the flanges (as well as through plate uplift). A similar pinched hysteresis with excellent deformation capacity and minimal strength degradation (i.e., less than 20% drop in peak base moments at 4% drift) was observed, except for Test #3 (with bundled U-bar hairpins) which had a drop in load after achieving capacity at around 2-2.5% drift).

Quantitative discussion of test data

Table 4.1 summarizes key quantities measured in the experiments. Two moment values are recovered for each test corresponding to maximum moment observed in each loading direction. These are denoted as M_{max+}^{test} and M_{max-}^{test} , such that the positive sign denotes the direction of application of the first deformation cycle. Referring to the table and Figures 4.8 and 4.9, the following observations could be made:

- 1- The main observation (referring to quantitative data from Grilli et al. 2017 – see Table 4.1), is that the application of horizontal reinforcement (i.e., attached reinforcement to column flanges) significantly reduced the strength (and stiffness) previously observed in similar details with no reinforcement and otherwise identical – see Figure 4.9d. This is because, the horizontal reinforcement introduced a tension field in the concrete area over the uplifting region of the base plate, which in turn, reduced the vertical resistance (from base plate upward bearing against concrete) resulting in a net reduction in strength relative to unreinforced specimens. Implications of this are discussed in the next section.
- 2- For comparing the effect of reinforcement attachment method in Tests #1 and 2 (Welded Rebar Stud versus U-bar Hairpin), the peak moment achieved from both tests is very close

while the load-deformation shows modest difference in terms of cycle-to-cycle degradation.



99
Figure 4.8 – Moment-rotation plots for all tests, and a schematic illustration of plotted quantities

- 3- A comparison between Tests #2 and 4 provides a direct assessment of the effect of additional vertical reinforcement/stirrups. Apparently, the installation of stirrups increased the strength/capacity of the connection by about 20%. This may be attributed to the fact that the vertical reinforcement mitigated/delayed the formation of the tension breakout cone which in turn allowed for higher moment resistance.
- 4- Comparing Tests #4 and 5 (which are similar in terms of embedment depth, attached reinforcement, and stirrups but differ in terms of column section and base plate geometry – see Table 4.1), the achieved capacities are almost identical. This is different from the observations from (Grilli et al. 2017) for a similar comparison (except with no reinforcement or stirrups attached), such that, a 12% increase in capacity was observed for specimen with wider flange (W14x370). This may be due to the fact that the moment distribution between the horizontal and vertical mechanisms (which is initially dependent on the stiffness of the embedded column – such that a highly flexible column will transfer less moment to the base) has been disturbed due to the formation of the crack behind the column flange, which caused a non-unique distinguishment between both scenarios (different column sizes).
- 5- The effect of additional horizontal reinforcement (reinforcement attachment) is assessed through Tests #2 and 3 (which differ only in terms of the amount of attached horizontal reinforcement). A 20% increase in moment capacity was observed in Test #3, with an increase in the number and diameters of the attached reinforcement.
- 6- All experiments achieved a tremendous deformation capacity in excess of 6% drift (as compared to about 3% for cases without attached reinforcement – see Figure 4.9d). This implies an excellent performance considering the deformation and hysteretic

characteristics of the connection when compared to deformation demands in a design-level shaking (2-3% drift).

The next section describes the development of a strength model for ECB connections considering all observed failure modes (and their interactions), while also applying/adopting fundamental principles from existing methods. This is followed by an assessment of the model while investigating the efficacy of the available strength characterization models for ECB connections against test data.

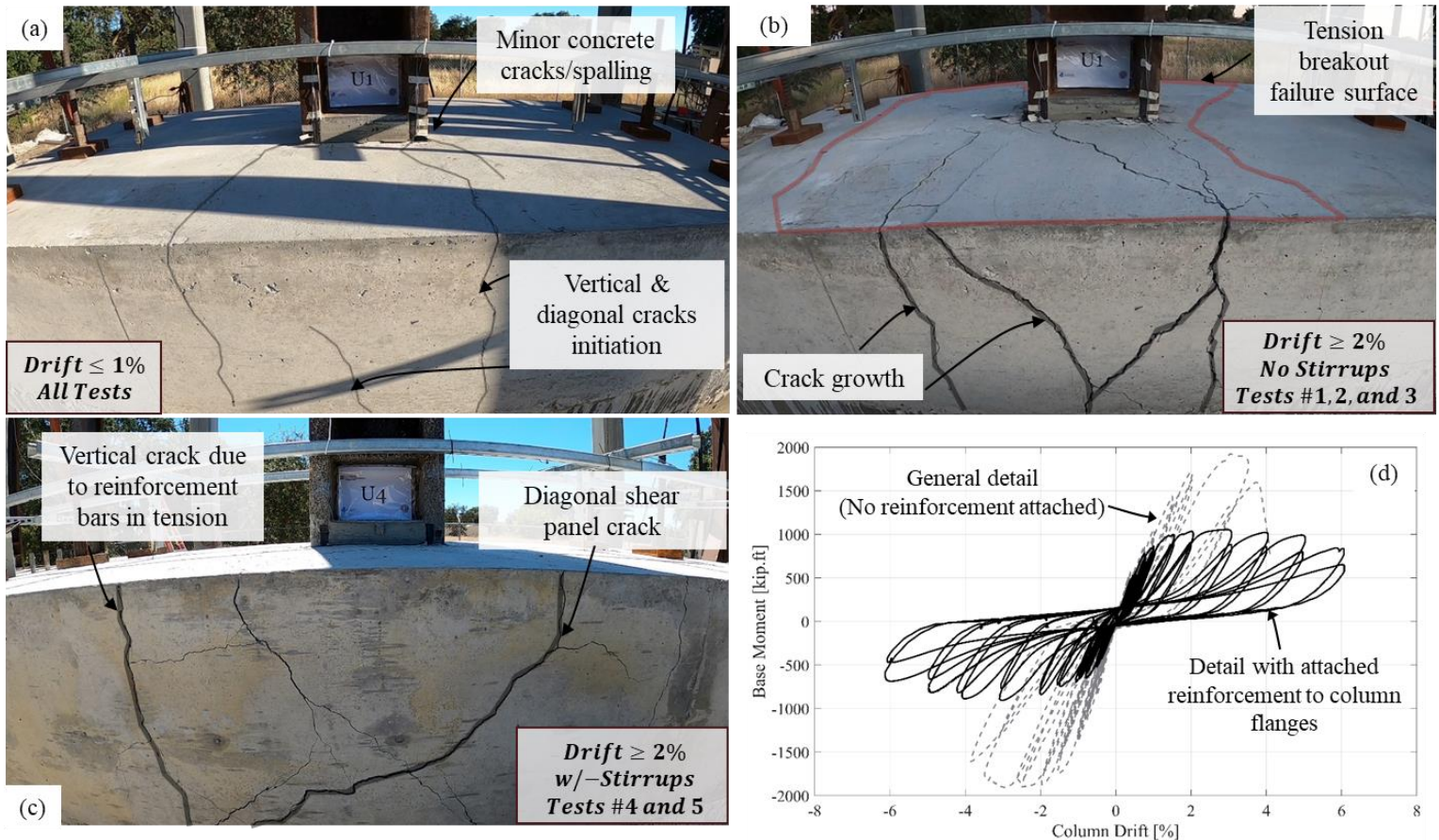


Figure 4.9 – Typical damage progression and behavioral insights: (a) below 1% drift for all tests; (b) failure mode for specimens with no stirrups (Tests #1, 2, and 3); (c) failure mode for specimens with stirrups (Tests #4 and 5); (d) moment-drift curve showing the effect of additional horizontal reinforcement as compared to a generic detail from Grilli et al. (2017)

4.5 PROPOSED MODEL FOR STRENGTH CHARACTERIZATION

Based on the observations from the experimental program, this section describes the development of strength model to facilitate the design and strength characterization of ECB connections. The model is based on three considerations (1) to reflect critical aspects of physics and internal force transfer as observed in previous experimental studies (Grilli and Kanvinde 2017), (2) to capture all relevant effects/failure modes associated with the addition/attachment of horizontal reinforcement, and (3) to quantify the vertical restraint provided to the base plate under varying levels of vertical/stirrup reinforcement.

Figure 4.10a schematically illustrates the two primary mechanisms of moment resistance, as discussed previously: (1) horizontal bearing stresses against the column flanges along with complementary shear panel zone, and (2) vertical bearing stresses resisting uplift of the base plate. The key assumption of the method is that the total applied base moment (denoted M_{base}) is resisted through a combination of horizontal and vertical bearing such that their moment contributions are additive (as shown in equation 4.2). This is consistent with the notation presented by Grilli and Kanvinde (2017) and discussed in a previous section. As proposed by Grilli and Kanvinde (2017), it is assumed that the net moment M_{base} is distributed in a constant proportion between the two mechanisms before any limit state/capacity is reached in either of the mechanisms (vertical or horizontal) through the introduction of the ratio α . This distribution is based on the assumption that no limit states are engaged simultaneously until the peak moment is reached. This is not the case for the ECB specimens tested in this program, wherein the peak moment is attained after obvious deformations in both vertical and horizontal directions.

Following this, the proposed model/approach adopts the concept of plastic mechanism development in which various response modes are mobilized and considered to be acting “in

parallel” such that their maximum contributions (limit states) are additive as shown in Figure 4.10b. The resistance due to each of those mechanisms is now discussed.

Moment resistance due to horizontal bearing stresses

Considering the free body diagram in Figure 4.10c, a portion of the applied moment (i.e., M_{HB}) and accompanied shear V is resisted through the development of bearing stresses on both sides of the embedded column flanges. A modified version of the previously discussed approach developed by Mattock and Gaafar (1981) is adopted in order to provide an estimation of the moment resistance provided by horizontal bearing mechanism while adding the horizontal reinforcement effect. The model idealizes the internal force transfer proposed by the original method while including the contribution of the attached reinforcement to the overall moment resistance. The developed bearing stresses are idealized such that a uniform and parabolic stress distributions are assumed for the top stress f_b^{top} , and the bottom stress f_b^{bottom} , respectively, such that:

$$f_b^{top} = 1.54 \sqrt{f'_c} \left(\frac{b_w}{b_f} \right)^n \quad (4.8)$$

And

$$f_b^{bottom} = 1000 f'_c [\varepsilon_b - 250 \varepsilon_b^2] \quad (4.9)$$

In the above equation for f_b^{top} (in ksi), the term b_w/b_f accounts for the effect of confinement, wherein b_w (in inches) is the width of the foundation, and b_f (in inches) is width of the flange. The exponent n is calibrated based on experimental data to a value of $n = 0.66$ (based on study by Mattock and Gaafar 1981- briefly described above). The concrete strain is assumed to vary linearly, with the maximum concrete strain taken as 0.003 at the top of the foundation, and defined as ε_b at the bottom (end of embedment). As per equation 4.9, the bearing stress distribution at the bottom of the embedded section may be expressed as parabolic function with maximum stress of

f'_c at a strain of $\varepsilon_b = 0.002$. Referring to Figure 4.10c, the term k_2 defines the location of the resultant compressive force C_{bottom} such that:

$$k_2 = \frac{1-0.375\left[\frac{d_{embed}-c}{c}\right]}{3-1.5\left[\frac{d_{embed}-c}{c}\right]} \quad (4.10)$$

and,

$$C_{bottom} = 0.5 \frac{b_f}{c} \left(\frac{b_w}{b_f}\right)^n f'_c (d_{embed} - c)^2 \left[3 - 1.5 \left[\frac{d_{embed}-c}{c}\right]\right] \quad (4.11)$$

and,

$$C_{top} = f_b^{top} \beta_1 c b_f \quad (4.12)$$

In the above, c (in inches) is the neutral axis depth and β_1 is the factor relating the depth of equivalent rectangular stress block to neutral axis depth. The attached reinforcement is assumed can act in tension and compression (in the case of welded rebars) and only in tension (in the case of the U-bar Hairpin) – see Figure 4.10c. The reinforcement bar is assumed to be elastic-perfectly-plastic and fully developed in tension (as per ACI 318-19). Forces in the rebars ($F_{rebar} = A_{rebar} \times F_y$) are assumed to be in the same direction of the applied shear for bars above the neutral axis, while being in the opposite direction for bars below. The resultant from each rebar row (upper and lower) are directly added to the resultants from the stress distributions, such that moment resistance due to horizontal stresses, M_{HB} may obtained by simultaneously solving the force and moment equilibrium equations based on the assumed force distributions, where:

$$V - C_{top} + C_{bottom} - F_{rebar}^{top} + F_{rebar}^{bottom} = 0 \quad (4.12)$$

$$V \times z = -C_{top} \frac{\beta_1 c}{2} + C_{bottom} \times [d_{embed} - k_2(d_{embed} - c)] - F_{rebar}^{top} d_r^{top} + F_{rebar}^{bottom} d_r^{bottom} \quad (4.13)$$

In the above equations, F_{rebar}^{top} , and F_{rebar}^{bottom} are the resultant forces from the engaged reinforcement rods, and d_r^{top} , and d_r^{bottom} are the distances from the rebars location to the top of the foundation surface, for the top and bottom rebars, respectively. Once V and c are calculated from equations (4.12) and (4.13), the moment resisted through horizontal bearing is then calculated as follows:

$$M_{HB} = V \times z \quad (4.14)$$

In the above derivation, the problem is defined while implicitly employing a moment-to-shear ratio (i.e., z the height of the column inflection point) as a given parameter. This implies that for a calculated value of M_{HB} , the corresponding connection shear V is constrained to it.

The next subsection provides a detailed discussion on the estimation of the moment resistance due to vertical bearing stress.

Moment resistance due to vertical bearing stresses

Referring to Figure 4.10d, the base plate at the bottom is subjected to bearing stresses on the lower as well as the upper surfaces, resisting the moment transferred to the base through the column flanges, as well as the net axial force transferred to the base plate. The base plate is assumed to resist the total axial force (through upward bearing in case of compressive load or downward bearing in case of tensile load) in addition to the moment resisted through the vertical bearing mechanism M_{VB} . The bearing stress distributions are idealized such that the moment is resisted through equal bearing blocks at the two ends of the plate (denoted f_{VB}^M) with equal length Y , such that $Y = 0.3N$, where N is the length of the base plate. This is based on agreement with test data (from this program as well as Grilli et al. 2017), and following similar approaches adopted for

composite connection design by the ASCE guidelines for composite connections (ASCE 1994). Following this, the vertical bearing stress in the blocks can be expressed as:

$$f_{VB}^M = \frac{M_{VB}}{(N-Y) \times Y \times B} \quad (4.15)$$

The stress due to the axial force (denoted f_{VB}^P) is considered to be uniform over the footprint of the base plate such that $f_{VB}^P = P/(B \times N)$, where P is the axial load and B is the width of the base plate (perpendicular to the direction of loading). This axial stress may be added or subtracted from the stress blocks f_{VB}^M , resulting in a stepped stress distribution where the end blocks carry stress equal to $f_{VB} = f_{VB}^M \pm f_{VB}^P$, depending on the axial load sign as shown in Figure 4.10d.

As previously discussed in the experimental study, two main failure modes were observed pertaining to the vertical resistance mechanism and involving the failure of the concrete block above the plate on the tension side of the connection. Since this failure type is generally controlled by the total force in the bearing block, rather than the bearing stress, the resultant of the stepped bearing stress distribution on the tension side of the connection is utilized for the model calculations, such that:

$$F_t = (f_{VB}^M - f_{VB}^P) \times (Y \times B) \quad (4.16)$$

This force F_t is calculated based on each failure mechanism/mode depending on the connection detailing. Referring to the prior discussion on the experimental results, the first failure mode observed is the breakout of the concrete through a cone failure on the tension side of the connection. The total breakout force may be calculated as shown below:

$$F_t = F_t^{breakout} = \frac{40}{9} \times \frac{1}{\sqrt{d_{cover}}} \times \sqrt{f_c'} \times A_{35} \quad (4.17)$$

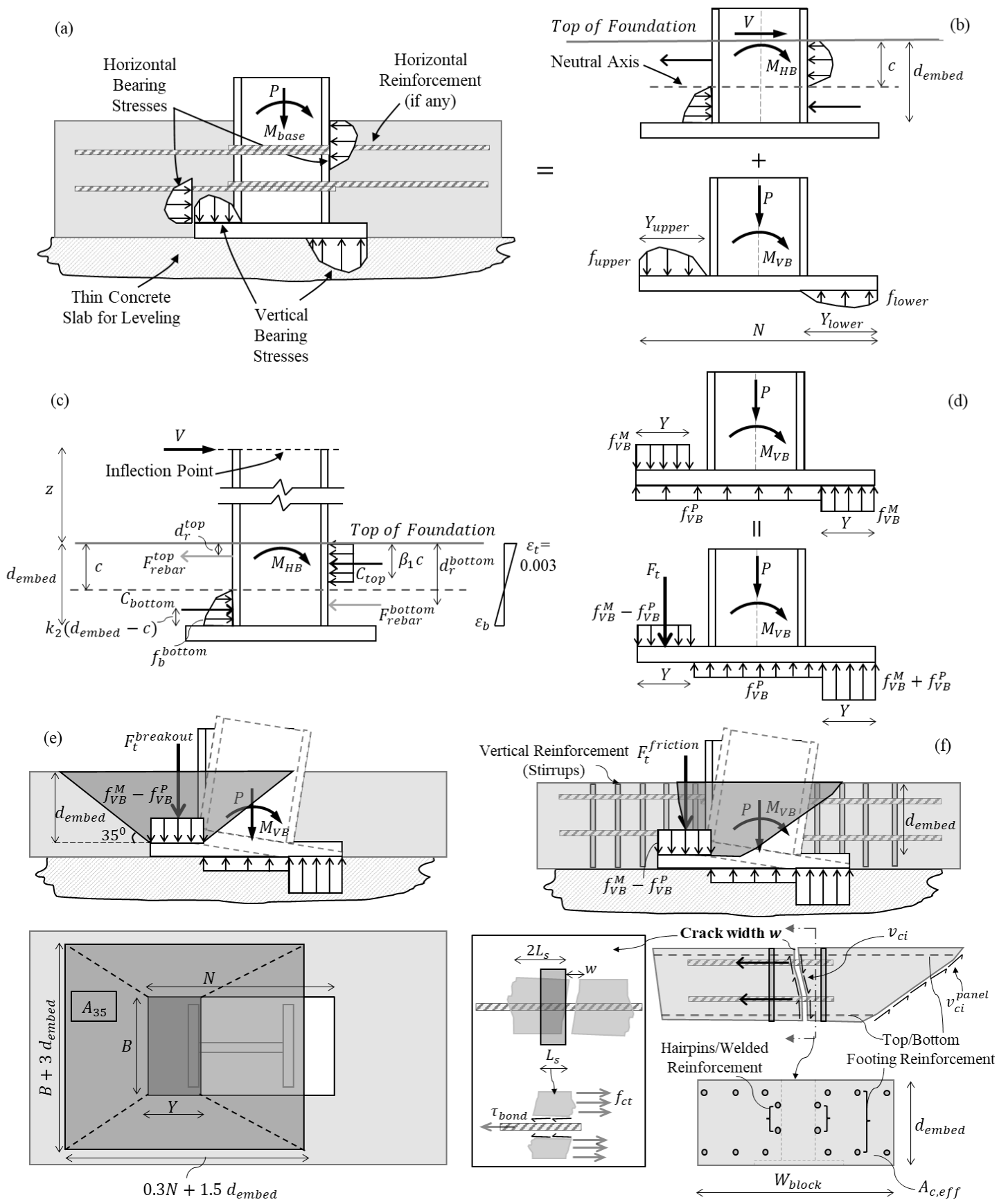


Figure 4.10 – Proposed model for strength characterization: (a) overall mechanism; (b) moment resisted due to horizontal forces and due to vertical forces; (c) horizontal resistance mechanism model (modified Mattock and Gaafar 1981) with the effect of reinforcement; (d) idealized vertical moment resistance – stepped bearing distribution due to moment and axial load; (e) tension concrete breakout failure mode (vertical bearing) with projected area A_{35} illustration; (f) shear/friction failure mode between stirrups (vertical bearing) with crack model illustrations

The above equation is based on the Concrete Capacity Design (CCD) method proposed by Fuchs et al. (1995), such that d_{cover} is thickness of the material which must be ruptured for breakout, which is equal to d_{embed} for tension breakout. The term A_{35} is the projected area of a 35-degree failure cone emanating from the edges of the stress block on the tension. The projected area A_{35} is shown in Figure 4.10e and is calculated using the equation below:

$$A_{35} = (B + 3 d_{embed}) \times (0.3 N + 1.5 d_{embed}) - (B \times 0.3 N) \quad (4.18)$$

Once established this way, the moment resisted through vertical bearing can be determined by solving both equations 4.15 and 4.16:

$$M_{VB} = \left(F_t - \frac{P \times Y}{N} \right) \times (N - Y) \quad (4.19)$$

It should be mentioned that this failure mode is applicable to details where no horizontal reinforcement is attached (tests by Grilli et al. 2017). As previously discussed, once reinforcement is attached to column flanges, a tension field is created above the uplifting end of the base plate reducing the resistance to vertical motion (to almost zero). In turn, the vertical bearing resistance could be conservatively assumed as zero (i.e., $M_{VB} = 0$). for cases where no additional vertical reinforcement (stirrups) is installed (for example, Tests #1, 2 and 3 from the experimental program).

The second failure mode observed is associated with the presence of vertical reinforcement/stirrups supplementary to the attached horizontal reinforcement. The purpose from having such reinforcement is to increase the vertical bearing resistance by mitigating the breakout failure mode. Referring to the test results and Figures 4.8d-e, the stirrups added a fair amount of vertical resistance while shifting the failure mode from a cone breakout into a direct shear failure at the weak point in the foundation (i.e., the cracked section between the stirrups location – see

Figure 4.9c). For this, the total resultant force F_t is calculated based on the amount of resistance provided by the upward bearing of the base plate against the cracked concrete section above. This requires the determination of the shear stress on the crack interface (i.e., the shear friction).

Based on the derivations by (Vecchio and Collins 1986), cracks occurring along the interface between the cement paste and the aggregate particles result in a rough surface which can transfer shear through aggregate interlocking (see Figure 4.10f). Vecchio and Collins (1985) developed a relationship between the shear stress transferred across the crack v_{ci} , the crack width w , and the required compressive stress f_{ci} (in psi) on the crack, such that:

$$v_{ci} = 0.18 v_{ci,max} + 1.64 f_{ci} - 0.82 \frac{f_{ci}}{v_{ci,max}} \quad (4.20)$$

Where $v_{ci,max}$ (in psi) is the maximum shear stress that can be transferred across a crack when its width is held at w (in inches), and given by:

$$v_{ci,max} = \frac{2.16 \sqrt{f'_c}}{0.3 + \left(\frac{24w}{a + 0.63} \right)} \quad (4.21)$$

Such that, a (in inches) is the diameter of the coarse aggregate in the cracked concrete, taken as 0.75 inches. Given that the crack (as shown in Figure 4.10f) is subjected to tension, therefore f_{ci} in equation 4.20 could be considered as zero, and the equation is reduced to

$$v_{ci} = 0.18 v_{ci,max} \quad (4.22)$$

It should be mentioned that the diagonal crack (formed due to panel shear) has zero shear strength (v_{ci}^{panel} - see Figure 4.10f) due to the fact that the shear panel crack has already opened up completely by the time the capacity connection capacity is attained. In order to calculate the crack width w , a classical mechanical approach based on the bond-slip relationship at reinforced concrete interface (i.e., bond law - CEB-FIP Model Code 1990) is employed. This method predicts the maximum crack width assuming the maximum possible slipping length, such that:

$$w = 2 L_s (\varepsilon_{sm} - \varepsilon_{cm}) \quad (4.23)$$

Where $2L_s$ is the maximum slip length and ε_s and ε_{cm} are the average value of steel and concrete strains, respectively. The transfer length L_s is defined as:

$$L_s = \frac{f_{ct} A_{c,eff}}{\tau_{bond} \Sigma \pi d_i} \quad (4.24)$$

Where f_{ct} (in ksi) is the tensile strength of concrete (taken as $7.5 \sqrt{f'_c}$ following the ACI 318-19 provisions), $A_{c,eff}$ (in square inches) is the effective area of concrete taken as $W_{block} \times d_{embed}$ (see Figure 4.10f) such that W_{block} is the width of the concrete foundation block, τ_{bond} (in ksi) is the average bond strength along the transfer length, taken as $0.95 \sqrt{f'_c}$ (ksi) based on canonical literature (CEB-fib Model Code 1990), and d_i is the diameters of bars crossing the considered crack (including the foundation main reinforcement bars as well as the horizontally attached reinforcement – as shown in Figure 4.10f). Once determined in this manner, the value of the upward force due to shear friction/aggregate interlocking across cracked section can be calculated as:

$$F_t^{friction} = v_{ci} \times A_{c,eff} \quad (4.25)$$

The above equation is then applied to equation 4.19 to calculate the vertical moment capacity for the connection where vertical/stirrups reinforcement is provided.

Finally, the connection strength as per the proposed unified model may be estimated as:

$$M_{max}^{Model} = M_{HB} + M_{VB} \quad (4.26)$$

Results and comparison to experimental data

Table 4.1 summarizes the test-to-predicted ratios for the strength estimates $M_{max}^{test}/M_{max}^{Model}$ for all test data points (i.e., from current experimental study and previous experimental program by Grilli

et al. 2017) using the methodology prescribed in the previous section. Also included in the table are the test-to-predicted ratios for the connection strength calculated as per the AISC SDM model $M_{max}^{test}/M_{max}^{AISC\ SDM}$, and the model developed by Grilli and Kanvinde (2017), $M_{max}^{test}/M_{max}^{Grilli}$, discussed previously (except with the inclusion of the effect of horizontal reinforcement for the model by Grilli and Kanvinde 2017 - following the approach explained above). Adding to the models' comparison, the test-to-predicted ratios using the model by Grilli and Kanvinde (2017), without considering the resistance to vertical uplift (for tests featuring horizontal reinforcement), denoted $M_{max}^{test}/M_{max}^{Grilli-HB}$, is also presented. Figures 4.11a-d plot the test-to-predicted ratios from all models against the column embedment depth (normalized by the depth of the column, i.e., d_{embed}/d_{col}). Referring to Table 4.1 and the figure, it is observed that:

- For the AISC SDM Method, results are little bit unconservative for cases with reinforcement while the method shows high variability across all test points (Overall Coefficient of Variation - CoV = 0.20). This is expected as the approach does not consider reinforcement effect (only considered for force transfer), and due to the fact that other aspects of the method (mentioned previously), where implicit assumptions in the method were particularized based on geometrical aspects/constraints which are not necessarily applicable to ECB connections (different ECB details other than the ones tested might yield different results).
- For the original model developed by Grilli and Kanvinde (2017), the method overestimates the strength of the connections (with reinforcement) with an average test-predicted ratio of 0.63 and CoV = 0.13. Referring to the preceding discussion and the qualitative progression of test response, this is not surprising as it suggests that the specimens do not derive significant strength from the vertical bearing mechanism. This

is because the horizontal reinforcement introduces tension in the bearing zone above the uplifting plate, greatly reducing the vertical resistance. In fact, a closer look at the test data suggests that the introduction of stirrups in this region result in a slight increase in the test-predicted ratio (i.e., on average 0.69 for Tests #4 and 5, compared to 0.55 for Tests #1 and #2). However, this increase, which presumably occurs due to the enhancement of vertical breakout strength of the concrete above the base plate, is not sufficient to overcome the loss of strength due to the tension field produced by the horizontal reinforcement.

- Considering the same model, while disregarding the vertical bearing resistance, the model results in significantly improved predictions of test data (compared to the original model including vertical resistance), with an average test-predicted ratio of 1.15, which is somewhat conservative. Interestingly, this model predicts the response of the tests without stirrups (i.e., Tests #1 and 2) with great accuracy (test-predicted ratio 1.00), whereas for the tests with stirrups (Test #4 and 5), the results are significantly conservative (i.e., test-predicted ratio of 1.27). This indicates that the vertical bearing capacity is enhanced to a significant degree by the stirrups, but not to the level of the previous Grilli et al. (2017) tests in which no horizontal reinforcement was present.
- Finally for the proposed unified model, overall, the model predicts the experimentally observed moment capacities with reasonable accuracy; on average the test-to-predicted ratio = 1.00 with a CoV = 0.12. As shown in Table 4.2, the agreement with both testing programs (with different details) is excellent (on average 1.09, with a tight CoV = 0.11). Referring to Figure 4.11d, the proposed method shows great accuracy across all

different details with different embedments this indicates that the model reflects the fundamental mechanics and behavioral aspects consistent with the phenomena controlling the strength of the ECB connection details.

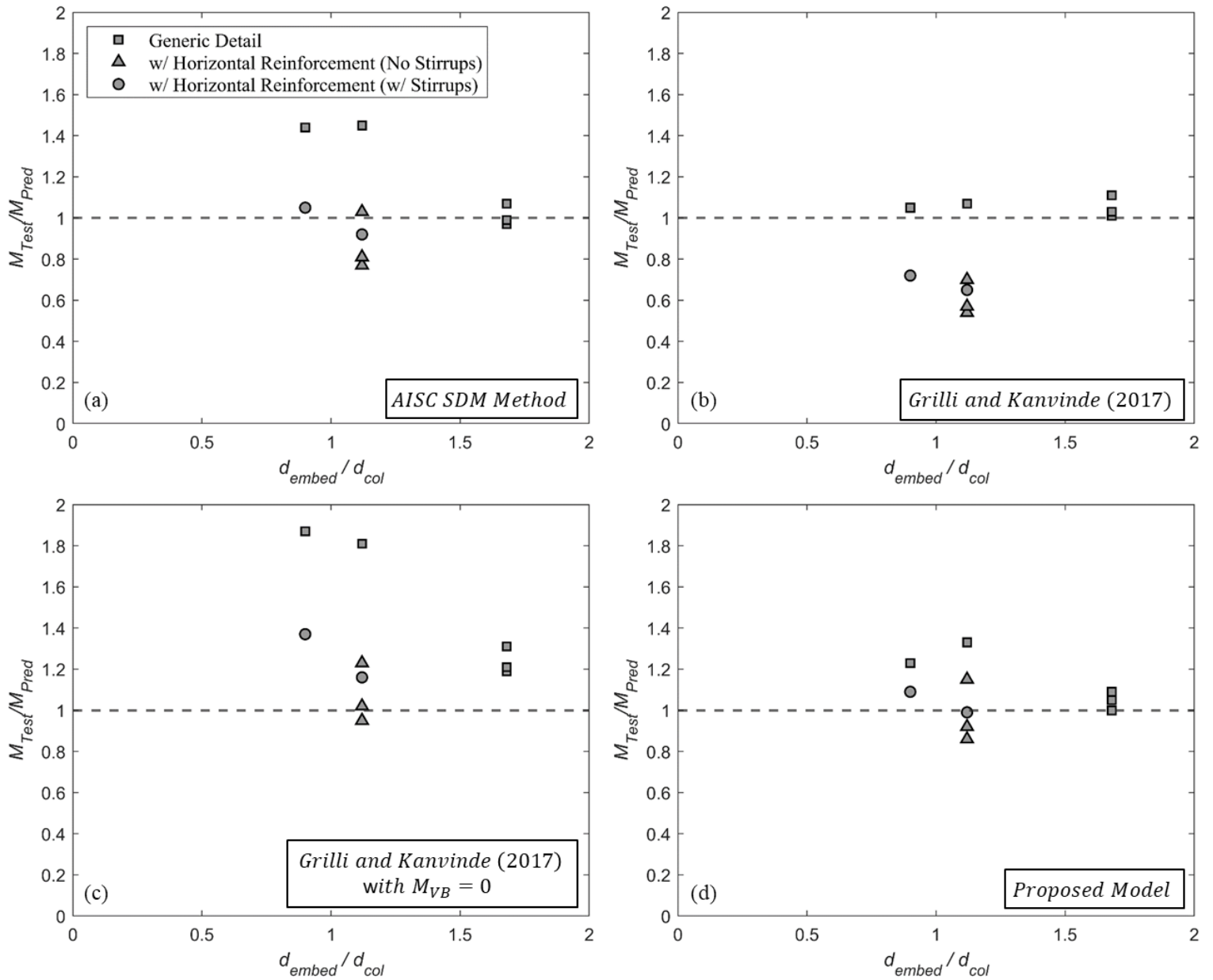


Figure 4.11 – Test-predicted ratios for all experiments from various strength characterization methods plotted against d_{embed}/d_{col}

4.6 SUMMARY AND CONCLUSIONS

Embedded Column Base (ECB) connections are widely used in mid- to high-rise steel moment frames to resist base moments. Despite their prevalence, methods available to design, and estimate their strength rely on experimental data on components (steel coupling beams embedded in concrete shear walls, and/or composite beam column connections) similar in aspects, however with major differences. This study presents findings from five tests representing of ECB connections with attached horizontal reinforcement (to increase connection strength) representative of the current construction practice. All specimens were cantilever columns loaded with cyclic lateral deformations under a constant axial load. The test variables were the method of reinforcement attachment (Welded reinforcement to column flange or U-bar hairpins anchored through the embedded portion of the column), area of the attached horizontal reinforcement, column cross section, and presence of additional vertical/stirrups reinforcement.

The tests revealed incredible a huge deformation capacity for such connections. The main observation is that the addition of attached horizontal reinforcement (specifically to column flanges – as common construction practice), reduces the strength and stiffness (albeit, significantly increases the ductility) of such connections as compared to details with no reinforcement attached. This is due to the fact that, the horizontal reinforcement introduces a tension field in the concrete area above the uplifting region of the embedded plate, resulting in a reduced vertical resistance and an overall net reduction in strength. Two main types of failure were observed: one was characterized by a breakout of concrete cone on the tension side of the connection, whereas the other was associated with a higher strength owing to the presence of additional vertical/stirrups reinforcement which mitigated the breakout failure, and instead failed in shear friction mode at the cracked interface between the cement paste and the aggregates between the stirrups location.

Based on these observations, a series of load resisting mechanisms are postulated (each is associated with local failure modes). A strength characterization model, based on these findings, is presented. The proposed approach is based on an idealized internal force distribution and fundamental mechanics, while providing adherence to key modes of physical response observed across all the test programs. To this end, the method idealizes some aspects of behavior, and leverages apposite elements/assumptions from previously developed strength models (Grilli and Kanvinde 2017 and AISC Seismic Design Manual 2018) and canonical theories on material behavior. The proposed approach is used to characterize the strength of all experiments, The results are encouraging, such that the new approach results in an average test-to-predicted ratio of 1.09, with a CoV of 0.11. This is significantly more accurate than the test-to-predicted ratios from the current AISC SDM approach or the Grilli and Kanvinde 2017 model, which shows higher variability and greater conservatism, respectively.

Despite the accuracy of the proposed approach and the improvement (with knowledge advancement) over the current approaches for strength characterization and design of ECB connections, the model has numerous limitations. The model is only validated against 10 test – since these are the only available data on ECB connections. The proposed method considered different failure modes pertaining to the uplift/vertical resistance, however other limit states associated with vertical bearing are also possible depending on the connection configuration; these include: (1) concrete breakout under the compression toe of the lower base plate (due to placement of the column on a thin layer of concrete), or (2) yielding of the base plate (if not sufficiently thick).

In conclusion, it is emphasized that the response of these connections is controlled by highly nonlinear and complex interactions between the various components (steel column/base, concrete,

and reinforcement). As a result, the development of a design or strength characterization method that explicitly satisfies equilibrium, compatibility, and nonlinear constitutive response of the various components is intractable. Consequently, the method presented in this study is based on some simplifying assumptions. This implies that caution should be applied in extrapolating the results of this study to details that are highly dissimilar from those examined in this study.

REFERENCES

- ABAQUS (2014). ABAQUS standard and ABAQUS documentation for version 6.14. Providence, RI: Dassault Systèmes Simulia.
- ACI (American Concrete Institute). (2019). “Building code requirements for structural concrete and commentary.” ACI 318-19, Detroit.
- American Institute of Steel Construction, Inc. (AISC). 2010. Seismic provisions for structural steel buildings. ANSI/AISC341. Chicago, IL, USA.
- American Institute of Steel Construction, Inc. (AISC). 2016. Prequalified Connections for Special and Intermediate Steel Moment Frames for Seismic Applications (ANSI/AISC 358–16), American Institute of Steel Construction, Chicago, IL, USA.
- American Institute of Steel Construction. (2016) Seismic Provisions for Structural Steel Buildings (ANSI/AISC 341–16), American Institute of Steel Construction, Chicago, IL, USA.
- American Institute of Steel Construction. (2017) AISC Steel Construction Manual, 15th Ed. Chicago, IL.. Chicago, (IL, USA): American Institute of Steel Construction.
- American Institute of Steel Construction, Inc. (AISC). (2018). Seismic Design Manual. 3rd ed. Chicago, IL, USA.
- Anderson, N. S., and Meinheit, D. F., (2005). Pryout Capacity of Cast-In Headed Stud Anchors,” *PCI Journal*, V. 50, No. 2, Mar.-Apr. 2005, pp. 90-112.
- Armstrong, P. J., and Frederick, C. C. (1966). A mathematical representation of the multiaxial Bauschinger effect. CEGB Rep. No. RD/B/ N731, Central Electricity Generating Board, Berkeley, UK.

- Applied Technology Council. (2009). Quantification of building seismic performance factors. FEMA P695. Washington, DC: FEMA.
- Astaneh, A., Bergsma, G. and Shen, J.H. (1992). Behavior and design of base plates for gravity, wind and seismic loads. Proceedings of the National Steel Construction Conference, AISC, Chicago, IL, USA.
- ASCE Guidelines (1994). Guidelines for Design of Joints Between Steel Beams and Reinforced Concrete Columns. Journal of Structural Division, ASCE, Vol. 120(8), pp. 2330-2357.
- ASTM International (2020). ASTM A370-20 Standard Test Methods and Definitions for Mechanical Testing of Steel Products., West Conshohocken, PA.
- ASTM International (2020). ASTM F1554-20. Standard Specification for Anchor Bolts, Steel, 36, 55, and 105-ksi Yield Strength. West Conshohocken, PA.
- Bažant, Z.P. (1976). Instability, ductility, and size effect in strain-softening concrete.” J. Engineering Mech. Div., Am. Soc. Civil Engrs., 102, EM2, 331—344; disc. 103, 357—358, 775—777, 104, 501—502.
- Burda, J. J., and Itani, A. M. (1999). Studies of seismic behavior of steel base plates. Rep. No. CCEER 99-7, Center for Civil Engineering Earthquake Research, Dept. of Civil Engineering, Univ. of Nevada, Reno, NV.
- Chaboche, J. L., K. D. Van, and G. Cordier. (1979). Modelization of the strain memory effect on the cyclic hardening of 316 stainless steel. In Proc., 5th Int. Conf. on Structural Mechanics in Reactor Technology. Amsterdam, Netherlands: North-Holland Publishing.
- Comite' Euro-International Du Beton. CEB-FIP model code (1990): Design Code. London: Thomas Telford Services Ltd.

- Considère, M. (1885). Memoirs on the use of iron and steel in construction.” Annales des Ponts et Chaussees, 9, 574–775.
- Cordova, P.P. and Deierlein, G.G. (2005). Validation of the Seismic Performance of Composite RCS Frames: Full-Scale Testing, Analytical Modeling, and Seismic Design. Technical Report 154, Blume Earthquake Engineering Center.
- Cui, Y., T. Nagae, and M. Nakashima. (2009). Hysteretic behavior and strength capacity of shallowly embedded steel column bases. J. Struct. Eng. 135 (10): 1231–1238. [https://doi.org/10.1061/\(ASCE\)ST.1943-541X.0000056](https://doi.org/10.1061/(ASCE)ST.1943-541X.0000056).
- de Castro e Sousa, A., Y. Suzuki, and D. Lignos. (2020). Consistency in solving the inverse problem of the Voce-Chaboche constitutive model for plastic straining. J. Eng. Mech. 146 (9): 04020097. [https://doi.org/10.1061/\(ASCE\)EM.1943-7889.0001839](https://doi.org/10.1061/(ASCE)EM.1943-7889.0001839).
- Drake, R. M., and S. J. Elkin. (1999). Beam-column base plate design - LRFD method. Eng. J. 36 (1): 29–38.
- Elkady, A., and D. G. Lignos. (2016). Dynamic stability of deep and slender wide-flange steel columns—Full scale experiments. In Proc., Annual Stability Conf. Structural Stability Research Council, 183–202. Chicago, IL: Structural Stability Research Council.
- Elkady, A., and Lignos, D. G. (2018). Full-scale testing of deep wide-flange steel columns under multiaxis cyclic loading: Loading sequence, boundary effects, and lateral stability bracing force demands.” J. Struct. Eng. 144 (2).
- Ermopoulos, J.C., Stamatopoulos, G.N. (1996). Analytical modeling of column-base plates under cyclic loading. Journal of Constructional Steel Research 1996; 40(3), 225-238.

- Fahmy, M., Stojadinovic, B., and Goel, S. C. (1999). Analytical and experimental behavior of steel column bases. Proc., 8th Canadian Conf. on Earthquake Engineering, Canadian Association for Earthquake Engineering, Ottawa.
- Falborski, T., and Kanvinde, A., (2022). Estimation of nonstructural stiffness in instrumented steel frames. Engineering Structures, Elsevier. <https://doi.org/10.1016/j.engstruct.2022.113947>.
- Falborski, T., Hassan, A., Kanvinde, A.M., (2020). Column Base Fixity in Steel Moment Frames: Observations from Instrumented Buildings. Journal of Constructional Steel Research, Elsevier. <https://doi.org/10.1016/j.jcsr.2020.105993>.
- Falborski T, Torres-Rodas P, Zareian F, Kanvinde AM. (2020). “Effect of base-connection strength and ductility on the seismic performance of steel moment-resisting frames.” J Struct Eng, ASCE;146(5):04020054.
- Fisher, J. M., and L. A. Kloiber. (2006). Design guide 1: Base plate and anchor rod design. 2nd ed. Chicago, IL: American Institute of Steel Construction, Chicago, IL, USA.
- Flores FX, Charney FA, Lopez-Garcia D. (2014). Influence of the gravity framing system on the collapse performance of special steel moment frames. Journal of Constructional Steel Research;101(0):351–362. DOI: 10.1016/j.jcsr.2014.05.020.
- Fuchs, W., Eligehausen, R. and Breen, J.E. (1995). “Concrete Capacity Design (CCD) Approach for Fastening to Concrete,” ACI Structural Journal, Vol. 92, No. 1, pp. 73–94.
- Gomez, I., G. Deierlein, and A. Kanvinde. (2010). Exposed column base connections subjected to axial compression and flexure. Final Report. Chicago, IL: American Institute of Steel Construction.

- Grauvilardell, J.E., Lee, D., Hajjar, J.F., and Dexter R.J. (2005). "Synthesis of Design, Testing and Analysis Research on Steel Column Base Plate Connections in High Seismic Zones," Structural Engineering Report No. ST-04-02. Minneapolis (MN): Department of Civil Engineering, University of Minnesota.
- Grilli, D. A., and A. M. Kanvinde. (2017). Embedded column base connections subjected to seismic loads: Strength model. *J. Constr. Steel Res.*129 (Feb): 240 249.
- Grilli, D., R. Jones, and A. Kanvinde. (2017). Seismic performance of embedded column base connections subjected to axial and lateral loads. *J. Struct. Eng.*143 (5): 04017010.[https://doi.org/10.1061/\(ASCE\)ST.1943-541X.0001741](https://doi.org/10.1061/(ASCE)ST.1943-541X.0001741).
- Hanks, K. N., and P. W. Richards. (2019). Experimental performance of block-out connections at the base of steel moment frames. *J. Struct. Eng.* 145 (7): 04019057. [https://doi.org/10.1061/\(ASCE\)ST.1943-541X.0002333](https://doi.org/10.1061/(ASCE)ST.1943-541X.0002333).
- Harries, K. A., Mitchell, D., Cook, W. D., and Redwood, R. G. (1993). Seismic response of steel beams coupling reinforced concrete walls. *J. Struct. Div.*, 10.1061/(ASCE)0733-9445(1993)119:12(3611), 3611–3629.
- Hassan, A.S., Song, B., Galasso, C., and Kanvinde, A.M., (2022). Seismic Performance of Exposed Column Base Plate Connections with Ductile Anchor Rods. *Journal of Structural Engineering*, American Society of Civil Engineers. 10.1061/(ASCE)ST.1943-541X.0003298.
- Hassan, A., Torres-Rodas, P., Giulietti, L., and Kanvinde, A.M., (2021). Strength Characterization of Exposed Column Base Plates Subjected to Axial Force and Biaxial Bending. *Engineering Structures*, Elsevier <https://doi.org/10.1016/j.engstruct.2021.112165>

- Hetenyi, M. (1946). *Beams on Elastic Foundation: Theory with Applications in the Fields of Civil and Mechanical Engineering*. University of Michigan Press (August 1, 1946).
- Huckelbridge A. A. (1977). Earthquake simulation tests of a nine storey steel frame with columns allowed to uplift. Report No. UBC/EERC-77/23, EERC, University of California, Berkeley, CA.
- Inamasu, H, de Castro e Sousa, A, Güell, G, Lignos, DG. (2021). Anchor-yield exposed column bases for minimizing residual deformations in seismic-resistant steel moment frames. *Earthquake Eng Struct Dyn.*; 50: 1083– 1100. <https://doi.org/10.1002/eqe.3392> .
- Kanvinde AM, Higgins P, Cooke RJ, Perez J, Higgins J. (2015). Column base connections for hollow steel sections: seismic performance and strength models. *J Struct Eng, ASCE*;141(7):04014171.
- Kanvinde AM, Jordan SJ, Cooke RJ. (2013). Exposed column base plate connections in moment frames—simulations and behavioral insights. *J Constr Steel Res* 2013;84: 82–93.
- Kanvinde, A. M. (2004). *Micromechanical simulation of earthquake-Induced fracture in steel structures*. Stanford, CA: Stanford Univ.
- Kanvinde, A. M. (2017). Predicting fracture in civil engineering steel structures: State of the art. *J. Struct. Eng.* 143 (3): 03116001.
- Kanvinde, A. M., Grilli, D. A., and Zareian, F. (2012). Rotational stiffness of exposed column base connections: Experiments and analytical models. *J. Struct. Eng.*, 10.1061/(ASCE)ST.1943-541X.0000495, 549–560.

- Kanvinde, A.M. and Grilli, D.A. (2013). “Special Moment Frame Base Connection: Design Example 8,” 2012 IBC SEAOC Structural/Seismic Design Manual, Volume 4, Examples for Steel-Frame Buildings, 255-280.
- Kent DC, Park R. (1971). Flexural members with confined concrete. *J Struct Div* 1971;97(7):1969–90.
- Kolwankar, S.S., Kanvinde, A.M., Kenawy, M., and Kunnath, S. (2017). A uniaxial nonlocal formulation for geometric nonlinearity induced necking and buckling localization in a steel bar,” *Journal of Structural Engineering*, American Society of Civil Engineers. 143(9): 04017091.
- Krawinkler, H., Gupta, A., Medina, R., and Luco, N. (2000). Loading histories for seismic performance testing of SMRF components and assemblies. Rep. No. SAC/BD-00/10, SAC Joint Venture, Richmond, CA.
- Lignos, D. G., Hikino, T., Matsuoka, Y., and Nakashima, M. 2013. Collapse assessment of steel moment frames based on E-Defense full-scale shake table collapse tests. *J. Struct. Eng.*, 10.1061/(ASCE)ST.1943-541X.0000608, 120–132.
- Marcakis, K. and Mitchell, D. (1980) Precast Concrete Connections with Embedded Steel Members. *Prestressed Concrete Institute Journal*, V. 25, No. 4, July/Aug. 1980, pp. 88-116.
- Mattock, A.H. and Gaafar, G.H. (1982) Strength of Embedded Steel Sections as Brackets. *ACI Journal*, Vol. 79, No. 2, pp. 83–93.
- McKenna, F., G. L. Fenves, M. H. Scott, and B. Jeremic (2012). Open system for earthquake engineering simulation (OpenSees). Berkeley, CA: Pacific Earthquake Engineering Research Center, Univ. of California.

- Menun, C., Kiureghian, A. D. (1999). Envelopes for seismic response vectors. I: Theory. *Journal of Structural Engineering*, ASCE 1999; 126(4): 467-473.
- Newell, J. D., and C.-M. Uang. (2008). Cyclic behavior of steel wide-flange columns subjected to large drift. *J. Struct. Eng.* 134 (8): 1334–1342. [https://doi.org/10.1061/\(ASCE\)0733-9445\(2008\)134:8\(1334\)](https://doi.org/10.1061/(ASCE)0733-9445(2008)134:8(1334)).
- Occupational Safety and Health Administration (OSHA). (2001). *Safety Standards for Steel Erection*, (Subpart R of 29 CFR Part 1926), Washington, D.C.; 2001.
- Pertold, J., Xiao, R., and Wald, F. (2000a) Embedded steel column bases – I. Experiments and numerical simulation, *J. Constr. Steel Res.* 56 (3) (2000) 253–270.
- Pertold, J., Xiao, R., and Wald, F., (2000b) Embedded steel column bases – II. Design model proposal, *J. Constr. Steel Res.* 56 (3) (2000) 271–286.
- Richards, P.W., Barnwell, N.V., Tryon, J.E. & Sadler A.L. (2018). Flexural strength and stiffness of block-out connections for steel columns. *Engineering Structures* 2018; 173, 404-415.
- Scott BD, Park R, Priestley MJN. (1982). Stress–strain behavior of concrete confined by overlapping hoops at low and high strain rates. *ACI J* 1982;79(1):13–27.
- SEAOC (Structural Engineers Association of California). (2015). 2015 IBC SEAOC structural/seismic design manual volume 1: Code application examples. Sacramento, CA: SEAOC.
- Shahrooz, B. M., Remetter, M. E., and Qin, F. (1993), “Seismic Design and Performance of Composite Coupled Walls,” *Journal of Structural Engineering*, ASCE, Vol. 119, No. 11, pp. 3291–3309, Reston, VA.

- Sheikh, T.M., Deierlein, G.G., Yura, J.A., and Jirsa, J.O. (1989). "Beam-Column Moment Connections for Composite Frames: Part 1," *Journal of Structural Engineering ASCE*, Vol. 115, November 1989, pp. 2858-2876.
- Smith, C., Ziccarelli, A., Terashima, M., Kanvinde, A., and Deierlein, G. (2021). "A Stress-Weighted Ductile Fracture Model (SWDFM) for Steel subjected to Ultra Low Cycle Fatigue." *Engineering Structures*, Elsevier, 245, 112964.
- Soules, J., Bachman, R., and Silva, J. (2016). *Chile Earthquake of 2010 – Assessment of Industrial Facilities around Concepcion*. American Society of Civil Engineers, Reston, VA, 2016.
- Terashima, M. (2018). *Ductile fracture simulation and risk quantification of buckling restrained braces under earthquakes*. Doctoral Dissertation, Stanford University.
- Timoshenko. (1940). *Strength of Materials, Second Edition*. D. Van Nostrand Company, Inc., 250 Fourth Avenue, NY; 1940.
- Torres-Rodas, P., Zareian, F., Kanvinde, A.M. (2016) Hysteretic Model for Exposed Column-Base Connections. *Journal of Structural Engineering*, ASCE 2016; 142(12): 04016137.
- Torres-Rodas, P., Zareian, F., and Kanvinde, A.M., (2018), A hysteretic model for the rotational response of embedded column base connections. *Soil Dynamics and Earthquake Engineering*, Elsevier, 115, 55-65.
- Trautner, C. A., T. Hutchinson, P. R. Grosser, and J. F. Silva. (2017). Investigation of steel column-baseplate connection details incorporating ductile anchors. *J. Struct. Eng.* 143 (8): 04017074. [https://doi.org/10.1061/\(ASCE\)ST.1943-541X.0001759](https://doi.org/10.1061/(ASCE)ST.1943-541X.0001759).

- Trautner, C. A., T. Hutchinson, P. R. Grosser, and J. F. Silva. (2016). Effects of detailing on the cyclic behavior of steel baseplate connections designed to promote anchor yielding. *J. Struct. Eng.* 142 (2):04015117. [https://doi.org/10.1061/\(ASCE\)ST.1943-541X.0001361](https://doi.org/10.1061/(ASCE)ST.1943-541X.0001361).
- Vecchio, F. J., and Collins, M. P. (1986). The Modified Compression Field Theory. *ACI Journal, Proceedings*, Vol. 83, No. 2, March–April 1986, pp. 219–231.
- Voce, E. (1948). The relationship between stress and strain for homogeneous deformation. *J. Inst. Met.* 74: 537–562.
- Wald, F. (2000). Column Base Modelling. In *Semi-Rigid Joints in Structural Steelwork*. Vienna: Springer; 2000, p. 227-288.
- Wald, F., Sokol, Z., and Steenhuis, M. (1995). Proposal of the Stiffness Design Model of the Column Bases. *Proceedings of the Third International Workshop on Connections in Steel Structures*, Trento, Italy.
- Zareian, F., and Kanvinde, A.M. (2013). Effect of Column Base Flexibility on the Seismic Safety of Steel Moment Resisting Frames. *Earthquake Spectra, Earthquake Engineering Research Institute*, 29(4), 1-2



.....
130 E Randolph St, Ste 2000
Chicago, IL 60601
.....
312.670.2400
.....
www.aisc.org

Research Report No. AISC-LRR-2022-01